DEVELOPING METHODS FOR DESIGNING SHAPE MEMORY ALLOY ACTUATED MORPHING AEROSTRUCTURES

A Thesis

by

STEPHEN DANIEL OEHLER

Submitted to the Office of Graduate Studies of
Texas A&M University
in partial fulfillment of the requirements for the degree of

MASTER OF SCIENCE

August 2012

Major Subject: Aerospace Engineering

DEVELOPING METHODS FOR DESIGNING SHAPE MEMORY ALLOY ACTUATED MORPHING AEROSTRUCTURES

A Thesis

by

STEPHEN DANIEL OEHLER

Submitted to the Office of Graduate Studies of
Texas A&M University
in partial fulfillment of the requirements for the degree of

MASTER OF SCIENCE

Approved by:

Chair of Committee,	Dimitris C. Lagoudas
Committee Members,	Darren J. Hartl
	Richard J. Malak
	James G. Boyd
Head of Department,	Dimitris C. Lagoudas

August 2012

Major Subject: Aerospace Engineering

ABSTRACT

Developing Methods for Designing Shape Memory Alloy
Actuated Morphing Aerostructures. (August 2012)
Stephen Daniel Oehler, B.S., Texas A&M University
Chair of Advisory Committee: Dr. Dimitris C. Lagoudas

The past twenty years have seen the successful characterization and computational modeling efforts by the smart materials community to better understand the Shape Memory Alloy (SMA). Commercially available numerical analysis tools, coupled with powerful constitutive models, have been shown to be highly accurate for predicting the response of these materials when subjected to predetermined loading conditions. This thesis acknowledges the development of such an established analysis framework and proposes an expanded *design* framework that is capable of accounting for the complex coupling behavior between SMA components and the surrounding assembly or system. In order to capture these effects, additional analysis tools are implemented in addition to the standard use of the non-linear finite element analysis (FEA) solver and a full, robust SMA constitutive model coded as a custom user-defined material subroutine (UMAT). These additional tools include a computational fluid dynamics (CFD) solver, a cosimulation module that allows separate FEA and CFD solvers to iteratively analyze fluid-structure interaction (FSI) and conjugate heat transfer (CHT) problems, and the addition of the latent heat term to the heat equations in the UMAT to fully account for transient thermomechanical coupling. Procedures for optimizing SMA component and assembly designs through iterative analysis are also introduced at the highest level. These techniques are implemented using commercially available simulation process management and scripting tools. The expanded framework is demonstrated on example engineering

problems that are motivated by real morphing structure applications, namely the Boeing Variable Geometry Chevron (VGC) and the NASA Shape Memory Alloy Hybrid Composite (SMAHC) chevron. Three different studies are conducted on these applications, focusing on component-, assembly-, and system-level analysis, each of which may necessitate accounting for certain coupling interactions between thermal, mechanical, and fluid fields. Output analysis data from each of the three models are validated against experimental data, where available. It is shown that the expanded design framework can account for the additional coupling effects at each analysis level, while providing an efficient and accurate alternative to the cost- and time-expensive legacy design-build-test methods that are still used today to engineer SMA actuated morphing aerostructures.

To my family:

my guiding father Greg,

my loving mother Kathy,

my insightful brother Mathew,

and my wife and best friend Christa

ACKNOWLEDGMENTS

There is a familiar phrase that was once coined: "It takes a whole village to raise a child." As my several years as an Aggie at Texas A&M University draw to a close, I am now convinced that this idea also applies to educating and preparing a graduate engineering student. There are many people in my life that I owe both my B.S. and M.S. degree to, and I'd like to thank them for their constant support (moral, technical, spiritual) in my journey to become a proper engineer.

I first want to thank my parents, most of all. My mother and father were both sources of constant moral and spiritual support. All of my drive to both succeed and to follow my ambitions has come from their gentle guidance. I thank them for providing a loving home and for always being there to remind me that I always *can* go home.

Before enrolling in graduate school, I was still on the fence about whether or not to pursue my Master's degree or just seek hire into industry. My first summer of undergraduate research work with the SMA research team, as Dr. Dimitris Lagoudas reminded me, was contingent on one condition: that I at least consider seeking a higher education before my senior year. Needless to say, I took the summer job, and am now extremely grateful that he planted the idea of graduate school in my head. After obtaining my Bachelors degree, I felt like I was an engineer. After obtaining my Masters, I *know* I am an engineer. I have Dr. Lagoudas to thank for this, and for bringing me on board as one of his students.

I also extend my thanks to Dr. Darren Hartl. As my supervisor, Darren often related with me on how the engineering world works, provided guiding (and sometimes blunt) words on how to handle my work and how to properly present myself as a researcher. As a colleague, he has been an invaluable source of motivation and

enthusiasm for investigating various applications for SMAs that have, as of yet, gone largely unexplored. One of the lasting memories I will have of working with the research team will be of sitting down with him in his office and, over cups of coffee, draw out a morphing structure that we might be interested in analyzing. He has inspired me to eventually become a leader in engineering.

During my research, I have had the pleasure of meeting and working with several great engineers from industry. I would like to extend my gratitude towards Jim Mabe, Dr. Stefan Bieniawski, and David Friedman from The Boeing Company, as well as Dr. Travis Turner from NASA Langley. The motivating engineering applications from this thesis are from their previous and continuing work, and their constant interaction with me over the past couple of years has been invaluable.

I would like to thank Dr. Richard Malak for providing a unique perspective to my research in the areas of design optimization. In addition, many of the capabilities of the expanded modeling framework presented in this thesis were made possible through his generosity in sharing optimization tool suite licenses with us.

I thank my colleagues from my MEEN 689 student group: Rick Lopez, Chris Bily, and Joanna Tsenn, who helped to create the design feasibility algorithm and some of the visualizations from the assembly-level analysis demonstrated in this thesis. I also thank my teammates of the SMA research team, for their support and readiness to help if I ever had questions about anything. I also thank my friends Nathan Jones and Kyle Huggins; I have been lucky to have these friends and colleagues who made the same journey in parallel with mine. I would like to especially thank my brother Mathew Oehler and Kate Wells for being such a great group of friends to enjoy my time with. Thank you all for seeing me through the various emotional states in which I have left my office in Wisenbaker.

Finally, I thank my wife and best friend, Christa. I don't think I could have

accomplished 6 years of aerospace engineering studies without her love and positive attitude. I could not thank her enough for what she has done for me; showing utmost enthusiasm when my research perfectly fell into place, and support when it fell apart. Undoubtedly, she is the reason I have made it this far.

Thank you all.

TABLE OF CONTENTS

CHAPTER Page

LIST OF TABLES

LIST OF FIGURES

FIGURE Page

FIGURE Page

FIGURE Page

CHAPTER I

INTRODUCTION AND LITERATURE REVIEW

Active research into characterizing and modeling the behavior of shape memory alloys (SMAs) has recently evolved into an effort to implement these materials as actuators in modern aerospace engineering applications. To aid in the design of SMA actuating components, many unique modeling tools are readily available that predict SMA constitutive response under most loading or environmental conditions. These models continue to be refined to focus on more difficult design problems with complex geometries. An increase in computational resources, in the form of parallel processing clusters and expanding allocations of fast-access memory, has allowed engineers to incorporate aspects of the material response into these models which were previously approximated or neglected due to insufficient computing power. However, despite advances in computational resources, simplifying assumptions are still prevalent in modern design methods. Examples include conducting static analyses and assuming boundary and loading conditions that are uniform or calculated from analytical solutions prior to analysis execution. However, it can be shown that these restrictions can be relaxed to take advantage of modern computing capabilities, resulting in greater overall accuracy and improved productivity.

The purpose of this work is to demonstrate some of the more recent developments in SMA modeling to consider solution-dependent, dynamic conditions and material behavior at three design levels: *component*, *assembly*, and *system*. The result is a comprehensive design framework that accounts for multiple aspects of the problem simultaneously. At each design level, a combination of commercially available and

---

The journal model is *IEEE Transactions on Automatic Control*.

custom coded tools are utilized. The Abaqus Finite Element Analysis (FEA) suite and a custom SMA constitutive model are used to assess morphing structure response. Model Center, a suite of optimization algorithms and simulation process management tools, is coupled with Abaqus to automate the execution of analyses at the component and assembly design levels. The unique methods described here fully account for mechanical, thermal, and fluid-structure interaction effects as they pertain to SMA morphing components and their integration into aerospace systems. This expanded analysis framework, while demonstrated on existing designs, is intended for use with any morphing structure application.

A. Relevance of SMAs in Aerospace

SMAs are a unique class of materials that, when subjected to controlled changes in temperature, have the capability of providing motion while under loads that exceed thousands of times their own weight and can do so over tens or hundreds of thousands of cycles. For this reason, significant research has been and is currently being conducted on implementing SMAs as high-powered, energy-dense actuators in aerospace applications. Indeed, the use of SMAs in aerospace has proven to be quite beneficial. Among many other capabilities, "smart" aeroelastic structures actuated by transforming SMAs could morph to modify aerodynamic characteristics in-flight to maximize the lift-to-drag ratio based on the current flight regime. From a maintenance perspective, these SMA solid-state actuators could potentially replace complex multi-component mechanisms that are difficult to diagnose should problems arise. Already several applications have been designed that utilize SMAs as actuators, such as morphing wings [1]-[5] and rotors [6]-[9], active engine inlet [10] and outlet [11], [12] structures that modify flow characteristics, and flow attachment devices [13], [14].

An excellent comprehensive summary [15], [16] exists which describes several such well-known and successful applications.

Some designs utilize the SMA as a morphing component to simply replace the conventional actuators already present in fixed-wing control surfaces. One notable example of this is shown in the works of Song and Ma [17]. Motivated by the high energy density of SMA wires, they installed opposing SMA wires to actuate a flap on a prototype fixed wing. Another fixed-wing application is shown in the work by Quackenbush et al. [14], who proposed the use of actuating SMA tabs attached to the surface of the wing as active vortex generators. This idea was motivated by the fact that static vortex generators, while effective in reattaching separated airflow to the wing, are the source of drag in flight regimes where they are not needed. However, not all applications of the SMA are intended as replacements of conventional actuators. Other designs utilize the SMA to morph the entire aerostructure. One example is the DARPA Smart Wing Project, the work of Kudva et al. [18], which utilized the twisting motion of internal SMA torque tubes to actuate a wing, enabling it to have controllable, variable twist that could be optimized to best fit the current flight regime. It is this classification of active structure, the morphing aerostructure, that is the focus of study in this thesis.

Two specific morphing aerostructure applications, the Boeing Variable Geometry Chevron (VGC) and the NASA SMA Hybrid Composite (SMAHC) chevron, are described in detail here as they motivate the engineering problems demonstrated in this thesis. Both the VGC [19] and the SMAHC chevron [12] are SMA-actuated morphing aerostructures developed by engineers as active mechanisms for reducing aircraft engine noise. Presently, static chevrons are installed circumferentially on jet engine outlets to reduce aircraft noise by causing turbulent flow to mix in an aeroacoustically advantageous manner [20]. However, the benefit of using static chevrons is quickly

lost as soon as the cruise condition of the flight regime is achieved, whereupon a significant reduction in engine efficiency is effected. The VGC and the SMAHC chevron are separate applications that aim to replace these static chevrons so that deflection of the turbulent engine flow can be deployed during takeoff and retracted during cruise.

The VGC assembly, illustrated in Fig. 1(a), consists of a composite panel actuated by three $Ni_{60}Ti_{40}$ (wt.%) (SMA) flexures installed onto the panel surface [19]. These three flexures are fastened to the panel and covered with thin film heaters to thermally induce flexure transformation. The panel, a carbon fiber composite, consists of a 15-ply layup of woven fabric with two regions supported by additional layers of uni-directional tape. These regions stiffen the panel to prevent buckling and provide additional bias force. Multiple morphing aerostructures, shown in Fig. 1(b), are installed circumferentially around the nozzle exit of a jet engine. When the heat strips are activated during takeoff, the flexures reverse transform, causing the composite panels to deflect into the jet engine outlet flow. This deflection mixes the outlet flow and reduces noise. These chevrons are then deactivated during the cruise portion of the flight pattern, cooling and returning to an undeformed shape, thus restoring engine efficiency. Although the *morphing* chevron design is not currently implemented on any aircraft, data from their flight testing was eventually used to design the *static* chevrons that are currently installed onto the Boeing 787 engine outlets to permanently reduce noise [11]. The thermomechanical behavior of the flexures during transformation is also well understood from previous analyses [21], [22] and thus the VGC is considered an excellent motivation for the example design problems in Chapters III and IV.

The SMAHC chevron, shown in Fig. 2, is a 5-ply composite chevron that is actuated by $Ni_{55}Ti_{45}$ (wt.%) (SMA) components [12]. In this manner, the SMAHC chevron is similar to the VGC, however the main difference lies in actuation behav-

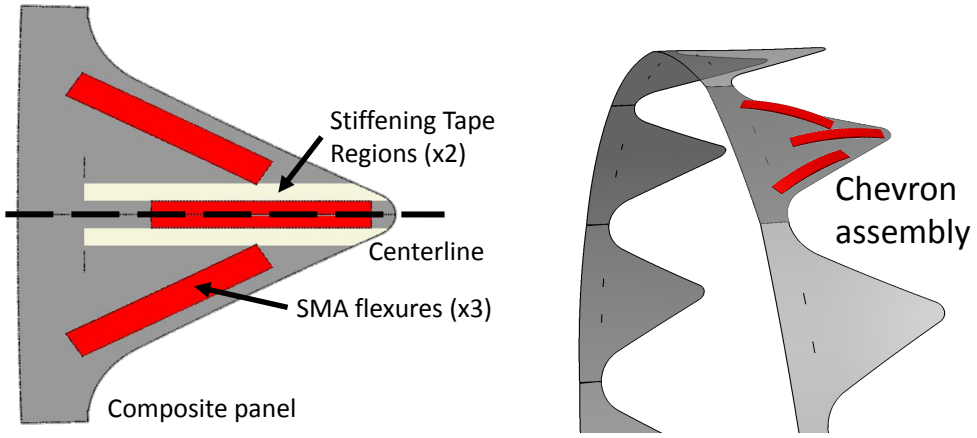

(a) Illustration of the stiffening tape regions and SMA flexure placement on the VGC. (b) Circumferential configuration of installed VGCs.

Fig. 1. VGC assembly and nozzle exit system.

ior of the SMA components. Rather than utilizing the bending motion of externally attached SMA flexures, the SMAHC chevron relies on the axial contraction of SMA ribbons installed in a pre-strained martensitic configuration below the neutral axis of the composite. The SMAHC chevron is one of the only morphing structure applications to have undergone representative flow testing in a controlled environment [12]. The existence of structural deflection data as a function of air velocity makes the SMAHC chevron an attractive example for demonstrating some advanced fluid-structure interaction (FSI) modeling capabilities outlined in Chapter V.

B. Phase Transformation in SMAs

Transformation of SMAs occurs between two distinct phases: austenite and martensite. At high temperatures or low stresses the SMA assumes an austenitic configuration, often called the *parent phase*, that is characterized by a high-symmetry cubic

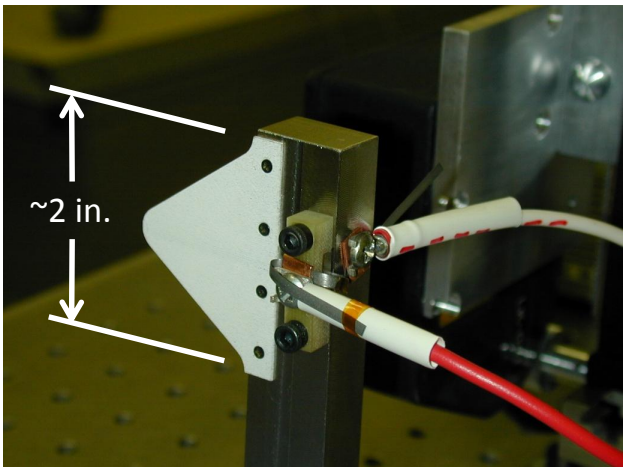

Fig. 2. Scaled prototype of the SMAHC chevron.

crystal structure, as illustrated in Fig. 3. From this point, *forward transformation* into a *twinned* or *detwinned* martensitic state, characterized by a tetragonal, orthorhombic, or monoclinic crystal structure, is dependent on the chosen thermomechanical loading path. Following a zero-stress change in temperature ($a \rightarrow b$), the SMA transforms into a twinned martensitic configuration. Note that, in Fig. 3, forward transformation into martensite begins at the martensitic start temperature (M_s) and completes at the martensitic finish temperature (M_f), and that the temperatures at which transformation initiates and completes increases with stress. Likewise, *reverse transformation* occurs when following the reverse path ($b \rightarrow a$) back into the austenitic configuration. Along this path ($a \rightarrow b \rightarrow a$) the SMA does not exhibit a macroscopic shape change, since twinned martensitic variants are self-accommodating and so the resultant transformation strain is small.

SMAs also exhibit what is called the *pseudoelastic effect*, where a controlled change in applied stress at constant temperature results in forward transformation into detwinned martensite. This isothermal loading path ($c \rightarrow d$) causes the material

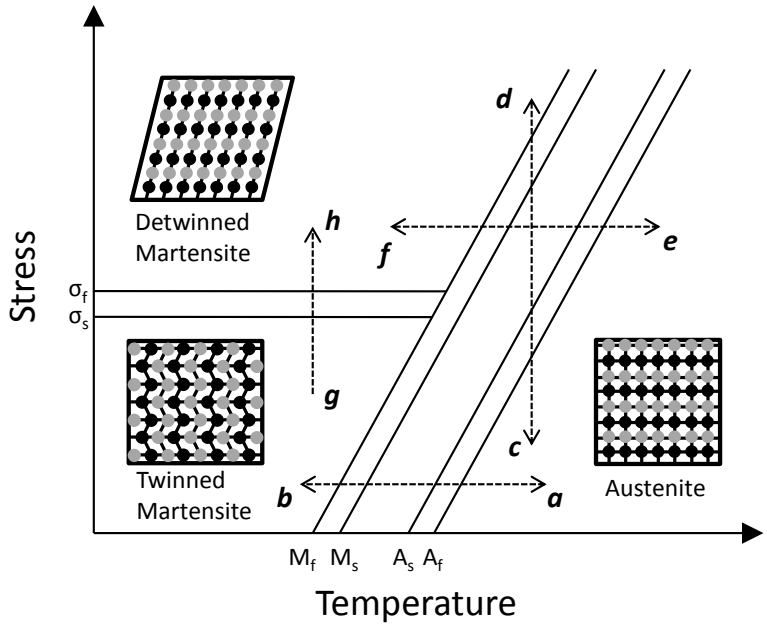

Fig. 3. Phase diagram of the typical SMA.

to deform in the direction of the applied load. Recovery is accomplished by following the reverse of the path ($d \rightarrow c$) such that the material reverse transforms back into austenite. The pseudoelastic effect is quite useful where SMA components are needed to absorb strain energy and recover large shape changes under nominally constant temperature conditions.

If the SMA is cooled from the austenitic configuration under constant non-zero stress ($e \rightarrow f$), the material forward transforms into detwinned martensite and deforms in the direction of the applied load. Note that the detwinned martensitic state can also be reached from the *twinned* martensitic state through isothermal application of stress ($g \rightarrow h$) that exceeds the detwinning start and finish stresses (σ_s and σ_f, respectively). Subsequent recovery of the austenitic configuration is accomplished by reheating the material ($f \rightarrow e$) through reverse transformation. The behavior of

the SMA along the $e \rightarrow f \rightarrow e$ loading path is useful for component actuation, where transformation can be effected through controlled temperature change to provide work against some other mechanism.

The work in this thesis develops and demonstrates methods for designing aerospace applications where SMA components provide loads against elastic structures, and therefore focuses on the role of the SMA as an actuator. However, as opposed to the simplified schematic where it is assumed that the actuator strictly adheres to an isobaric thermal cycle path, we instead consider an arbitrary or mixed thermomechanical loading path that is dynamic and solution-dependent.

C. Design Framework

The objective of this thesis is to develop analytical modeling methods that allow an engineer to efficiently model a morphing aerostructure design and to optimize over this design with reasonable confidence that the solution is accurate. Historically, initial boundary value modeling of conventional morphing structures entailed conservative approximations for mechanical and thermal boundary conditions. These approximations were typically formulated to simplify the problem or to reduce computational cost. The overwhelming majority of existing morphing structure designs utilize the SMA within the context of an assumed highly controlled environment, and therefore analysis of these designs tends to be simplified with static or predetermined boundary conditions. However, actuating SMA components in a morphing *aerostructure* setting are often exposed to the same highly variable environments experienced by the aeroelastic assembly: dynamic and transient thermal and mechanical loads. Therefore, assuming static or predetermined boundary conditions is not appropriate in this case. The inherent sensitivity of SMA transformation behavior to local

changes in stress and temperature suggests that accuracy of predicting SMA thermomechanical response could be improved by allowing loading conditions to vary with the structure's environment and by accounting for transient effects of transformation, such as the generation and absorption of latent heat. The methods described in this thesis therefore have the capability to account for all of these pertinent aspects of the multiphysical problem: transient mechanical and thermal behavior, and interaction between the structure and the fluid environment.

This work proposes a comprehensive design framework for the design and optimization of SMA morphing aerostructures, as illustrated in Fig. 4 in the form of a Venn diagram. Three aspects are of particular interest here: *mechanical*, *thermal*, and *fluid*. The intersection of two circles defines the capability of the model to account for the coupling effects between two aspects of multiphysics. For instance, the intersection between the mechanical and thermal fields implies a thermomechanically coupled (TMC) model, where the transient evolution of latent heat is coupled to the transformation strain rate of the SMA. Similarly, the intersection between the mechanical and fluid fields represents a fluid-structure interaction (FSI) model and the crossover between fluid and thermal fields is a conjugate heat transfer (CHT) model. The ideal model accounts for, and therefore exists at the nexus of, all three aspects of interest.

Note that, just because the model is *capable* of accounting for all three fields, it does not necessarily mean that such a powerful design tool should be blindly applied to any and all morphing structure applications. The work here will demonstrate that the engineer should carefully consider the necessary use of certain aspects of the ideal model based on the level of complexity of the design problem. For example, the engineering problems studied in this work consider static behavior, transient thermal effects, or fluid-structure interaction based on the design level (component, assembly,

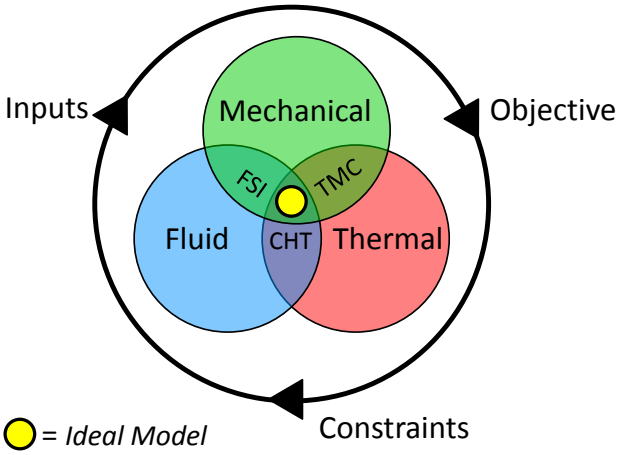

Fig. 4. Diagram of the comprehensive design framework.

or system). However, the developed framework is, in general, capable of handling the extreme case where consideration of all three fields is required.

Finally, an optimization study over the base design may be conducted, as illustrated in Fig. 4, where three defining characteristics of the study must be considered [23]:

- Objective - a function that quantitatively evaluates the performance of a structural analysis. An optimized design solution is one that maximizes or minimizes the value produced by this function. Objective functions that are formulated with the intent of being minimized are referred to here as *cost functions*, while functions that are maximized are *utility functions*.

- Inputs - design variables of the parameterized model that affect the value of the objective function. These are altered with each iterative analysis to maximize or minimize the objective and converge upon a design solution.

- Constraints - specified criteria that the model must satisfy in order for the

design solution to be considered feasible.

Determining the optimized design solution using a model is accomplished via an iterative analysis process, and can therefore become the most computationally expensive component of the framework. The effective use of iterative optimization is dependent on the ability of each analysis to be completed in a timely fashion. The following subsections briefly address the aspects of the diagram relevant to this work and reviews existing literature about each subject.

1. The SMA Constitutive Model

Several models for predicting SMA behavior under thermal and mechanical loading conditions have been developed and widely used for the design of SMA applications. The most common of these are 1-D analytical or numerical solutions to problems with simple geometries such as beams, wires, torque tubes, and others. However, for modeling the complex behavior of SMAs in 3-D, design engineers often turn to FEA implementations of more powerful, full SMA constitutive models. The Brinson et al. [24] and Lagoudas et al. [25] phenomenological models are examples of custom-coded constitutive models that have been successfully implemented into FEA commercial codes for the purpose of designing SMA applications [8], [26]-[29], [22]. A full review of other well-known 1-D and 3-D SMA constitutive models can be found in the text of Lagoudas et al. [30].

Many commercially available codes have the capability of referencing custom material subroutines. In fact, commercial codes have developed native modules for modeling the transformation of SMA components based on existing SMA constitutive models. One example is Simulia's Abaqus Unified FEA suite [31], which now includes by default a precompiled user-defined material (UMAT) implementation of

the Auricchio and Taylor [32], [33] model to predict the pseudoelastic behavior of Nitinol under transformation-induced mechanical loads at temperatures above A_f. This model maps the transformation surfaces using input calibrated phase diagram parameters and uses linear transformation hardening functions. Another example is MSC's Marc FEA suite [34] that includes two different SMA models. One model is based on the same work by Auricchio [33] and thus only considers pseudoelastic effects of the SMA component. The other model is based on the work by Saeedvafa and Asaro [35] that predicts actuation and pseudoelastic behavior of SMAs and can account for transformation-induced plasticity.

As will be discussed in more detail in Chapter II, the expanded design methods described in this thesis utilize an established Abaqus-based [31] finite element framework that references a powerful UMAT implementation of the phenomenological model developed by Lagoudas et al. [25], [36].

2. Transient Thermal Effects

An important design consideration for morphing aerostructures is the operating actuation frequency of its active components. For integration into control surfaces, such as ailerons or flaps, these active components are expected to actuate (i.e. transform) within a reasonable timeframe in order for feedback control to be effective. Unfortunately, the rate of thermally-induced SMA transformation is significantly hindered by low thermal conductivity and high specific heat values of the material. Compounding this issue is the generation and absorption of latent heat during transformation that is antagonistic to fast actuation [37]. The exothermic reaction of forward transformation and conversely the endothermic reaction accompanying reverse transformation can significantly delay SMA actuation if thermal energy is not quickly removed or supplied, respectively [38].

Since the removal or supply of latent heat is dependent on the rate of heat transfer, transient thermal effects should be considered when designing SMA actuator components for use in control surfaces. Thus, the specification of homogeneous changes in the temperature field, as is the conventional practice of modeling static behavior of SMA components, is no longer appropriate. The mechanical and thermal equations must be solved simultaneously, in a coupled manner, in order to properly predict actuation frequency. Several models have been developed to account for this coupling between mechanical and thermal fields. For example, the model referenced in this thesis contains elements from the thermodynamically consistent Boyd and Lagoudas model [39] that describes the forward phase transformation surface using a J2-type plasticity analogy. Another example is the SMA thermomechanical model by Christ et al. [40] that is derived from a multiplicative strain decomposition, and therefore accounts for large deformations. Using this model, comparative analysis was performed on representations of SMA specimens, whereupon a rate-dependent increase in body temperature was observed under pseudoelastic loading conditions and a change in actuation strain rate was observed with a change in heat flux. Another example, from the works of Richter et al. [38], is an implementation of the Muller-Achenbach-Seelecke model [41] into an Abaqus UMAT to analyze the latent heat induced damping characteristics in pseudoelastically transforming SMA beams, tubes, and wires.

As mentioned previously, the SMA constitutive model described in Chapter II is rigorously derived in a thermodynamically consistent manner and therefore may include the volumetric latent heat term in the energy balance [42]. However, in accounting for latent heat, the numerical computation of the global structural response becomes quite complex, since convergence upon a solution of the coupled thermomechanical equations is highly dependent on time increment size and mesh refinement.

3. Fluid-Structure Interaction

The overwhelming majority of existing morphing structure designs utilize the SMA within the context of an assumed highly controlled environment, and therefore analysis of these designs tends to be simplified with predetermined boundary conditions. However, the integration of SMAs into aeroelastic structures [43], [19], [14] motivates an increased demand for more complex modeling of their operation in realistic *dynamic* environments. The highly coupled nature of fluid flow with aeroelastic structures requires careful consideration of interaction effects. This is especially important with SMA actuated morphing aerostructures, since the SMA exhibits variable actuation characteristics that are highly dependent on thermomechanical loading history.

The coupled interaction between fluid flow and actuating SMA structures has already been studied to some degree using a variety of fluid-structure interaction (FSI) analysis techniques, however this subject seems to have been limited to works by Lagoudas and coworkers. For example, one relatively early work describes the use of *cosimulation* to analyze the FSI of a smart wing that actively morphs to maximize aerodynamic performance per the current flight regime [3]. In the cosimulation, a finite element analysis (FEA) of the SMA structure runs in parallel to, and exchanges displacement and pressure data with, a computational fluid dynamics (CFD) panel method code and iterates until the two quasi-static/steady-state simulations converge upon the same solution. A later work also utilizes this iterative "partitioned" approach to calculate change in mass flux through porous SMA channels, although following a much more rigorous implementation of the Stokes equations into the FEA equations [44].

This thesis represents one of the first known efforts to propose the use of commercial cosimulation capabilities in an established FEA framework [21], [22]. The new

model is able to solve complex FSI problems when specified boundary conditions cannot appropriately capture the solution-dependent effects associated with high-speed fluid flow. This is demonstrated in Chapter V with an analysis of a particular morphing aerostructure, the NASA SMAHC chevron. Note that this framework can be used with any such structure.

4. Design Optimization

Over the past fifteen years, much research has been dedicated to advancing engineering design techniques of smart structures for use in both active and passive applications. Earlier works describe design optimization techniques for these applications using gradient-based or analytical solution-based approaches to simplified, often 1-D engineering problems. A comprehensive summary [45] exists which concisely summarizes methods that were developed and utilized up until 2003 and categorizes them by general design objectives. According to this summary, primary research interest lay in optimizing:

- placement of the active component(s) with respect to a resistive or working mechanism,
- shape, size, and/or number of active components,
- feedback controller properties (feedback gains, voltages, damping, etc.), and
- material properties/orientation of active and passive bodies (density, number of composite plies, orientation of fibers, etc.).

The focus of this thesis is to develop methods for designing SMA actuator applications, such as morphing structures [46]. A recent review of SMA design efforts [47]

highlights ongoing research using iterative analysis techniques to find optimized design solutions with these same objectives in mind and many of these same techniques will be applied herein. Another work describes the process for designing SMA spring components using gradient optimization algorithms [48]. Efforts have also utilized genetic algorithms to explore more expansive design spaces for such applications as SMA wire-actuated rotors [49], SMP morphing structures [50], hybrid SMA-SMP active joints [51], and SMA structural damping mechanisms [52]. Recent works by Langelaar and van Keulen [53]-[55] detail more advanced methods for structural design optimization. In an effort to increase computing efficiency, they investigate the use of structural sensitivity analysis methods [23], [56] to guide a gradient optimization algorithm in the search for an optimized SMA actuator topology [53]. Another work by Gurav and coworkers [57] describes a computationally efficient optimization technique that utilizes Bounded-But-Unknown uncertainty analysis [58], [59] to design the shape of an SMA microgripper.

An early detailed discussion of the design process for aerospace-specific SMA applications appeared in 2003, when optimization methods were applied to determine the configuration of SMA wires to change the shape of an airfoil [3], where solid and fluid responses were considered. In addition, the success of the flight tests for the Boeing VGC and associated analysis studies [21], [22] has inspired related design optimization efforts [60]. The work presented in Chapter III and IV of this thesis builds upon those past efforts by presenting comprehensive methods for determining optimized design configurations of individual SMA components and of the whole morphing aerostructure. Although this method is demonstrated by specifically considering the design of one aerostructure, it is intended for adaptation to any SMA-based morphing structure, especially those with multiple components of differing material properties.

D. Outline of the Thesis

This thesis is organized as follows:

- Chapter II describes in detail the wide array of numerical analysis tools used to demonstrate the expanded modeling framework. This includes discussion of the FEA framework, FSI cosimulation scheme, and design optimization methods.

- Chapter III presents a numerical analysis that exemplifies a design optimization problem at the component level. The thermomechanically coupled model fully accounts for the transient evolution of latent heat of a transforming SMA component and solves for optimized material distribution to minimize actuation cycle time.

- Chapter IV presents a design optimization problem at the assembly level. Optimization algorithms are applied to a static model that considers the complex interaction between transforming SMA actuators bonded to an aeroelastic structure. Placement and orientation of the SMA actuators with respect to the assembly are determined to maximize performance metrics based on actuation-induced deflection of the aeroelastic structure.

- Chapter V demonstrates the effective use of cosimulation techniques to analyze dynamic environmental effects at the system level. The evolving, solution-dependent boundary conditions of a an SMA actuated morphing aerostructure in representative fluid flow are manifested as the exchange of data between isolated and uncoupled FEA and CFD models across a common FSI surface. The effect of the fluid flow on the actuated deflection profile of the aerostructure, and likewise the effect of the structure on the flow characteristics, are determined.

- Chapter VI summarizes and concludes this work, and suggests future efforts to improve the demonstrated portions of the expanded model framework.

CHAPTER II

SUMMARY OF NUMERICAL ANALYSIS TOOLS

The expanded modeling framework outlined in the previous chapter consists of a large set of numerical analysis tools and simulation automation algorithms. Any given model may require many of these tools to be intricately linked in order to predict the response of SMA actuators under transient thermomechanical loading conditions, analyze the interaction between a structure and a fluid environment, or iteratively optimize a given design. All of these tools and their connectivity are described in detail in the following sections. The first section elaborates upon the established finite element framework and the implemented SMA constitutive model. The second section presents a method for modeling fluid-structure interaction of morphing structures using commercially available numerical analysis tools. The third and final section describes the process through which a morphing structure design is optimized and the array of algorithms used to accomplish this task.

A. Modeling of SMAs

In this work, we choose to use an established method for modeling the complex nonlinear behavior of 3-D SMA actuators developed by Lagoudas and coworkers. This method, which calls for a finite element implementation of a powerful SMA constitutive model, is proven to be accurate and computationally efficient [22], [61], [47]. This section outlines the tools specific to this framework, reviews the numerical methods behind nonlinear FEA and how the element and nodal degrees of freedom (DOFs) are evaluated, and discusses the SMA constitutive model.

1. Finite Element Framework

As research into active materials progresses, it is becoming clear that the design and integration of SMA actuator technology into aerospace assemblies requires powerful and accurate analysis tools. Designing the optimal actuator for a given assembly could mean that the SMA could take on any number of exotic forms, be subjected to transient thermomechanical loading conditions, and contact or interact with other components. It is therefore important to utilize an FEA tool that has the capability of analyzing 3-D SMA actuation behavior while considering all of these effects.

Before discussing the FEA tool chosen to analyze SMA behavior, this subsection first provides a brief overview of the process used to discretize the governing equations for an example 3-D linear mechanical analysis in FEA. To begin, three sets of governing equations are used [62]. The first are the strain-displacement equations, given by:

$$\boldsymbol{\varepsilon} = \mathbf{D}\mathbf{u}, \tag{2.1}$$

where the strains $\boldsymbol{\varepsilon}$ and partial matrix $\mathbf{D}$ are arranged as:

$$\boldsymbol{\varepsilon} = \begin{Bmatrix} \varepsilon_{xx} \\ \varepsilon_{yy} \\ \varepsilon_{zz} \\ \varepsilon_{xz} \\ \varepsilon_{yz} \\ \varepsilon_{xy} \end{Bmatrix}, \quad \mathbf{D}^{\mathrm{T}} = \begin{bmatrix} \frac{\partial}{\partial x} & 0 & 0 & \frac{\partial}{\partial z} & 0 & \frac{\partial}{\partial y} \\ 0 & \frac{\partial}{\partial y} & 0 & 0 & \frac{\partial}{\partial z} & \frac{\partial}{\partial x} \\ 0 & 0 & \frac{\partial}{\partial z} & \frac{\partial}{\partial x} & \frac{\partial}{\partial y} & 0 \end{bmatrix}. \tag{2.2}$$

The second set contains the equations of motion:

$$\mathbf{D}^{\mathrm{T}}\boldsymbol{\sigma} + \mathbf{f} = \rho\ddot{\mathbf{u}}, \tag{2.3}$$

where ρ is the material density and the stresses $\boldsymbol{\sigma}$, body forces $\mathbf{f}$, and displacements $\mathbf{u}$ are arranged as:

$$\boldsymbol{\sigma} = \begin{Bmatrix} \sigma_{xx} \\ \sigma_{yy} \\ \sigma_{zz} \\ \sigma_{xz} \\ \sigma_{yz} \\ \sigma_{xy} \end{Bmatrix}, \quad \mathbf{f} = \begin{Bmatrix} f_x \\ f_y \\ f_z \end{Bmatrix}, \quad \mathbf{u} = \begin{Bmatrix} u_x \\ u_y \\ u_z \end{Bmatrix}. \tag{2.4}$$

Finally, the third set contains the constitutive equations:

$$\boldsymbol{\sigma} = \mathbf{C}\boldsymbol{\varepsilon} = \mathbf{S}^{-1}\boldsymbol{\varepsilon}, \tag{2.5}$$

where the constitutive matrix $\mathbf{C}$ is given by the inverse of the elastic compliance matrix, or $\mathbf{S}^{-1}$. The principal of virtual displacements is applied, resulting in the following integral form over the arbitrary domain Ω and domain boundaries Γ:

$$\int_{\Omega} \left[(\mathbf{D}\delta\mathbf{u})^{\mathrm{T}}\mathbf{C}(\mathbf{D}\mathbf{u}) + \rho\mathbf{u}^{\mathrm{T}}\ddot{\mathbf{u}} \right] \mathrm{d}\Omega - \int_{\Omega} (\delta\mathbf{u})^{\mathrm{T}}\mathbf{f}\,\mathrm{d}\Omega - \oint_{\Gamma} (\delta\mathbf{u})^{\mathrm{T}}\mathbf{t}\,\mathrm{d}\Gamma = 0, \tag{2.6}$$

where $\mathbf{t}$ are the traction vectors applied to the boundaries of the domain. This is spatially discretized to give the linear finite element model:

$$\mathbf{K}\boldsymbol{\Delta} = \mathbf{F} + \mathbf{Q}, \tag{2.7}$$

where $\boldsymbol{\Delta}$ is a vector containing all of the nodal degrees of freedom (in this case, the

displacements), $\mathbf{K}$ is the global stiffness matrix, $\mathbf{F}$ is the element load vector, and $\mathbf{Q}$ is a vector containing internal forces.

This model is applicable for linear FEA, in which the global stiffness matrix is considered constant throughout the analysis. However SMAs exhibit nonlinear behavior, and so calculation of a tangent stiffness matrix for use in an incremental form of the SMA constitutive equation is necessary:

$$d\boldsymbol{\sigma} = \mathbf{k}_{uu} : d\boldsymbol{\varepsilon} + \mathbf{k}_{uT} dT, \tag{2.8}$$

where $\mathbf{k}_{uu}$ and $\mathbf{k}_{uT}$ are the continuum tangent stiffness and thermal tensors. The derivation of the full forms of these tensors can be found in the text of Lagoudas et al. [63].

Since this is a nonlinear analysis considering SMA, the assembled global stiffness matrix $\mathbf{K}(\boldsymbol{\Delta})$ is expected to change as a function of the nodal degrees of freedom. The final discretized equation becomes:

$$\mathbf{K}(\boldsymbol{\Delta})\boldsymbol{\Delta} = \mathbf{F} + \mathbf{Q}. \tag{2.9}$$

where $\boldsymbol{\Delta}$ now contains both nodal displacements and temperatures.

Solution of these nonlinear algebraic equations requires an iterative solution-finding process. For this reason, the tool used to analyze the engineering example problems in this work is the Abaqus FEA Product Suite from Simulia [31]. Abaqus is a commercially available nonlinear FEA solver that allows for the creation of custom user material subroutines (UMATs) with which unique nonlinear constitutive behaviors may be defined. As mentioned in Chapter I, Section C.1., Lagoudas and coworkers elected to use this finite element framework to predict SMA behavior, utilizing a UMAT implementation of a robust 3-D SMA constitutive model.

Illustrated in Fig. 5 is an example of the solution-finding process used by Abaqus /Standard. While this process has been already been described for a 3D stress analysis in another work [47], this is expanded upon to include coupled temperature-displacement effects here. We consider a hypothetical structure that has been discretized into a collection of material points, some of which may be subjected to mechanical or thermal loads. The global solver then operates on the premise that the forces, moments, and heat fluxes at each node must sum to zero [31].

Note that, since this is a nonlinear material, the solution is not as trivial as inverting a structural stiffness matrix once. An iterative process begins with iteration $i = 0$ by calculating a linear FEA solution to an elastic approximation of the coupled stiffness matrix $[K]_{elastic}$ and, given applied forces, moments and/or heat fluxes, $\{f\}_i$ and $\{Q\}_i$, calculates the resultant strains $[\varepsilon]_i$ and nodal temperatures T_i and passes them into the UMAT. The SMA constitutive, transformation, and heat equations[1] are used to solve for the equivalent stresses $[\sigma]_i^{mp}$ and latent heat of transformation $r_i^{t,mp}$, and update the internal set of state variables ξ_i^{mp} per each material point mp. The UMAT also determines the mechanical and thermal tangent stiffnesses $[k]_i^{mp}$, then passes these values back to the global solver. The global solver sums the forces and moments to form the mechanical residuals $\{R_u\}$ and sums the heat fluxes to form the thermal residual $\{R_T\}$. The displacement and temperature correction vectors $\{c_u\}$ and $\{c_T\}$ are then determined and the global stiffness matrix $[K]$ is assembled. The process continues to refine the initial guess through the reduction of the residuals using Newton's method. Newton's method is used to approximate a new set of nodal displacements and temperatures based on the residuals and the coupled stiffness matrix of the current iteration. The new displacements and nodal temperatures

[1]The SMA constitutive model is explained in detail in Chapter II, Section A.2.

are passed into the UMAT, as before, to repeat the process until the norms of the mechanical and thermal residuals and corrected displacements and temperatures are sufficiently small (i.e. below some specified tolerance). Then, the process exits, increments the boundary conditions, and calculates a new initial elastic guess for the next increment.

The Abaqus FEA Product Suite allows the meshing of a solid body using any of the element variations it provides, which are tailored for specific purposes [31]. These elements are grouped into eight "families": *continuum* (solid and fluid elements), *conventional shell*, *beam*, *rigid*, *membrane*, *infinite*, *special purpose* (dashpots and springs), and *truss*. For brevity, we will review only certain elements in the *continuum* and *conventional shell* element families here, since they will be used to discretize the FEA models in the example engineering problems described in Chapters III, IV, and V[2].

Continuum elements are the standard, general-purpose elements for FEA that can account for contact, plasticity, and large deformations for most applications such as linear and nonlinear stress, heat transfer, and fluid pressure [31]. Also grouped into this family are other more powerful elements that can couple certain effects such as piezoelectric, electromagnetic, and thermomechanical. These elements can come in many forms: 1-D, 2-D (triangles and quadrilaterals), 3-D (tetrahedrals, wedges, and hexahedrals), axisymmetric, or cylindrical and can interpolate nodal degrees of freedom using linear or quadratic shape functions. The continuum element of specific interest in this work, as encountered in Chapter III, is the 3-D thermomechanically coupled hexahedral element `C3D20RT`. This element is illustrated in Fig. 6. As a reduced integration element, it uses a reduced number of Gaussian quadrature points

[2] A full description of all eight families can be found in the Abaqus element library manual [31]

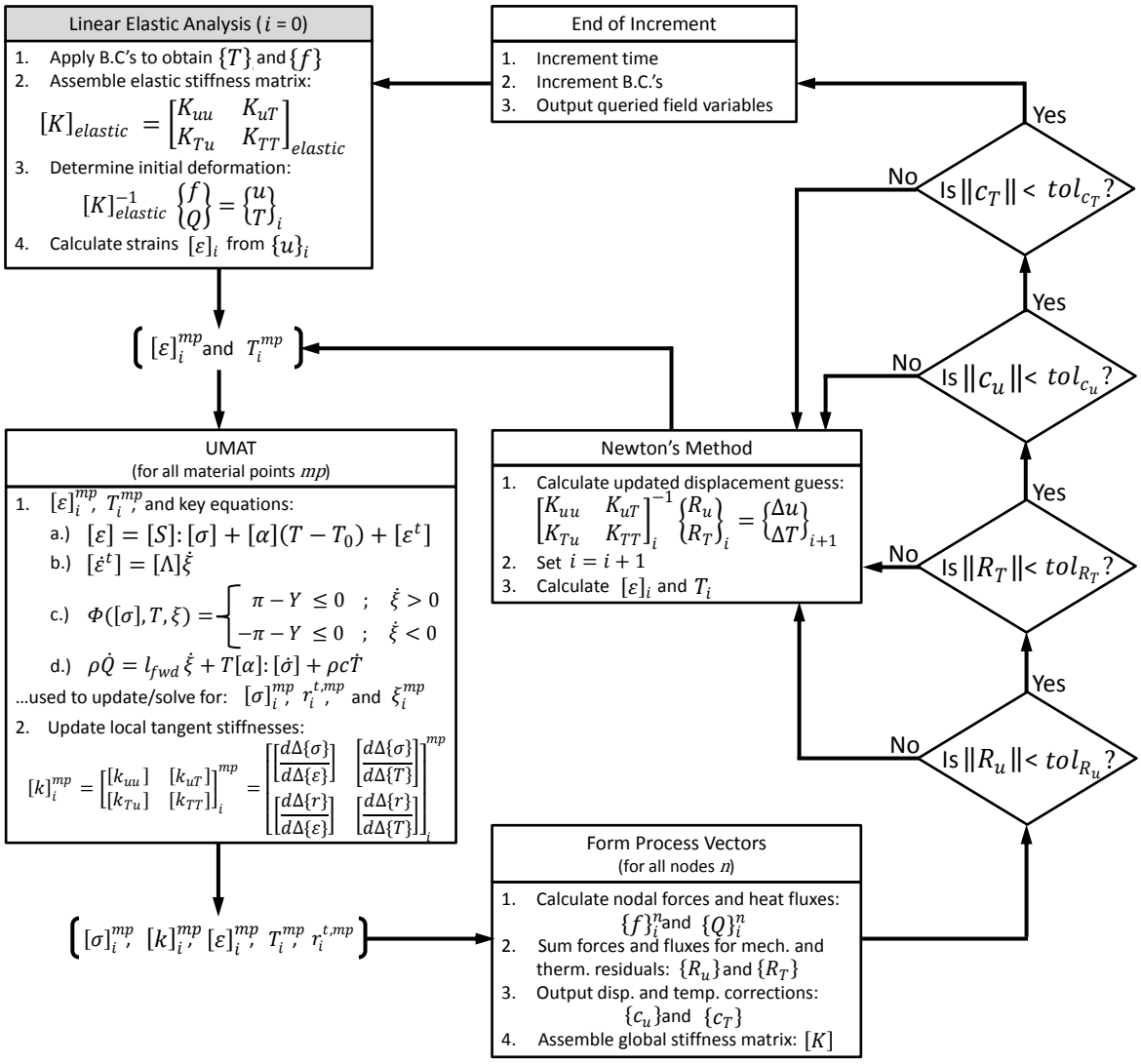

Fig. 5. The iterative solution-finding process for the Abaqus/Standard nonlinear FEA global solver.

to calculate the stiffness matrix, and is therefore computationally less expensive than the full integration option. There are four active nodal DOFs in this element: the x-, y-, and z-displacements, and temperature. Note that, while the displacements are interpolated using quadratic shape functions, the nodal temperatures are only evaluated at the corners and are thus interpolated linearly.

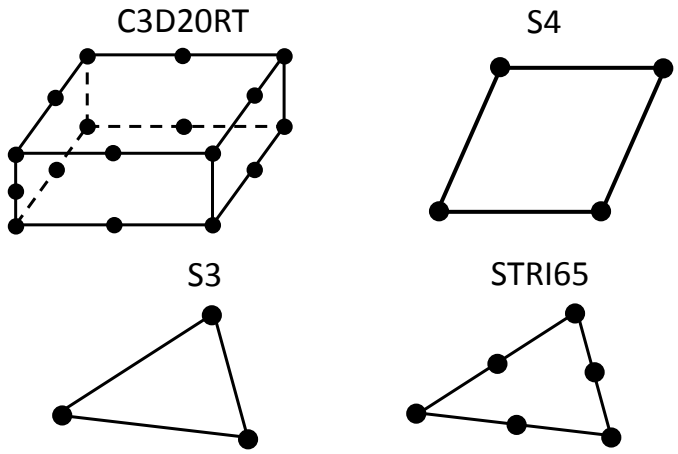

Fig. 6. Abaqus/Standard continuum and shell elements of interest.

Conventional shell elements can be used to mesh geometries where the thickness of the structure is considered much smaller than the other dimensions [31]. These elements can analyze linear and nonlinear stress, heat transfer, and thermo-mechanical effects and can take on triangular and quadrilateral forms with linear or quadratic shape functions. The *conventional shell* elements of interest in this work, as encountered in Chapters IV and V, can be used to discretize multiple-ply composite bodies rendered as a single layer. Illustrated in Fig. 6, they are the `S3`/`S4` triangular/quadrilateral linear stress elements, which include six nodal DOFs (three displacements and three rotations), and the STRI65 6-node triangular element, which assumes transverse shear deformation to be negligible and includes five nodal DOFs

(three displacements and two in-plane rotations).

2. SMA Constitutive Model

The aforementioned UMAT used in this work consists of an accurate 3-D SMA constitutive model implemented in the FORTRAN language. This particular constitutive model is rigorously developed to ensure that the key constitutive relations and evolution equations are thermodynamically sound. A detailed discussion of the model derivation process can be found in the works of Lagoudas and coworkers [46], and so will not be covered in this work. However, a brief summary of the resulting constitutive relations and transformation conditions is outlined here.

We begin with an additive decomposition of the total strain tensor $\boldsymbol{\varepsilon}$ into elastic strain $\boldsymbol{\varepsilon^{el}}$, thermoelastic strain $\boldsymbol{\varepsilon^{th}}$, and transformation strain $\boldsymbol{\varepsilon^{t}}$:

$$\boldsymbol{\varepsilon} = \boldsymbol{\varepsilon^{el}} + \boldsymbol{\varepsilon^{th}} + \boldsymbol{\varepsilon^{t}}. \tag{2.10}$$

Certain models exist that properly account for the evolution of transformation-induced plastic strain in SMAs [64] or consider the reorientation of variants of martensite [65]. However, for simplicity, the model used in this work assumes that the only inelastic strain component is the transformation strain $\boldsymbol{\varepsilon^{t}}$.

The Hooke's Law equation is stated:

$$\boldsymbol{\varepsilon} = \boldsymbol{S}(\xi)\boldsymbol{\sigma} + \boldsymbol{\alpha}(T - T_0) + \boldsymbol{\varepsilon^{t}}, \tag{2.11}$$

where $\boldsymbol{\alpha}$ is a second-order thermal expansion coefficient tensor and $\boldsymbol{S}$ is a fourth-order compliance tensor. The compliance tensor is a function of the evolving martensite volume fraction ξ and the compliance tensors $\boldsymbol{S^A}$ and $\boldsymbol{S^M}$ for the austenite and martensite phases, respectively, and is formulated as a rule of mixtures given by:

$$\boldsymbol{S}(\xi) = \boldsymbol{S^A} + \xi(\boldsymbol{S^M} - \boldsymbol{S^A}). \tag{2.12}$$

The evolution equation, which is responsible for relating the time rate of change of transformation strain with the time rate of change of the internal state variable ξ, assumes the form of a flow rule:

$$\dot{\boldsymbol{\varepsilon^t}} = \boldsymbol{\Lambda}\dot{\xi}. \tag{2.13}$$

Here, the transformation tensor $\boldsymbol{\Lambda}$ indicates the direction of transformation with the branching function:

$$\boldsymbol{\Lambda} = \begin{cases} H^{cur}(\overline{\sigma})\frac{3}{2}\frac{\boldsymbol{\sigma'}}{\overline{\sigma}} & ; \quad \dot{\xi} > 0 \\ \frac{\boldsymbol{\varepsilon}^{t-r}}{\xi^r} & ; \quad \dot{\xi} < 0 \end{cases} \tag{2.14}$$

where H^{cur} is a scalar value that represents the magnitude of the transformation strain, which generally increases with Mises stress, and $\boldsymbol{\varepsilon}^{t-r}$ and ξ^r are the transformation strain and the martensitic volume fraction at the point of transformation reversal (i.e. the point at which the material stops forward transforming and begins reverse transforming). For reference, the deviatoric stress $\boldsymbol{\sigma'}$ is given by:

$$\boldsymbol{\sigma'} = \boldsymbol{\sigma} - tr(\boldsymbol{\sigma})\mathbf{I}, \tag{2.15}$$

and the associated effective von Mises scalar measure of the stress tensor $\overline{\sigma}$ is defined by:

$$\overline{\sigma} = \sqrt{\frac{3}{2}\boldsymbol{\sigma'} : \boldsymbol{\sigma'}}. \tag{2.16}$$

The phase transformation of the SMA is described by a transformation function, $\boldsymbol{\Phi} = \boldsymbol{\Phi}(\boldsymbol{\sigma}, T, \xi)$, such that:

$$\mathbf{\Phi} = \begin{cases} \pi - Y & ; \quad \dot{\xi} > 0 \\ -\pi - Y & ; \quad \dot{\xi} < 0 \end{cases} \tag{2.17}$$

where Y is the critical thermodynamic driving force necessary to initiate transformation, the current value (π) of which is given by:

$$\pi(\boldsymbol{\sigma}, T, \xi) = \boldsymbol{\sigma} : \mathbf{\Lambda} + \frac{1}{2}\boldsymbol{\sigma} : \Delta\boldsymbol{S} : \boldsymbol{\sigma} + \boldsymbol{\sigma} : \Delta\boldsymbol{\alpha}(T - T_0) + \\ - \rho\Delta c((T - T_0) - T\ln(\frac{T}{T_0})) + \rho\Delta s_0 T - \rho\Delta u_0 - \frac{\partial f}{\partial \xi}, \tag{2.18}$$

where ρ is the material density, c is the specific heat capacity, s_0 and u_0 are the respective reference entropy and internal energies, and $f(\xi)$ is a chosen transformation hardening function. As seen from (2.17), transformation occurs when π value equals Y. Thus, during transformation $\mathbf{\Phi}$ is necessarily zero:

$$\mathbf{\Phi} = 0. \tag{2.19}$$

From the above relations, the evolution of the martensitic volume fraction is said to be governed by the set of constraints called the Kuhn-Tucker conditions. These conditions are concisely stated as:

$$\dot{\xi} \geq 0; \qquad \mathbf{\Phi}(\boldsymbol{\sigma}, T, \xi) = \pi - Y \leq 0; \qquad \mathbf{\Phi}\dot{\xi} = 0; \tag{2.20}$$

$$\dot{\xi} \leq 0; \qquad \mathbf{\Phi}(\boldsymbol{\sigma}, T, \xi) = -\pi - Y \leq 0; \qquad \mathbf{\Phi}\dot{\xi} = 0; \tag{2.21}$$

With the equations described here, the full 3D constitutive model is implemented in the finite element framework, and is subsequently used to predict the thermomechanical response of SMAs as integrated actuators in morphing aerostructures.

In certain cases, however, it important to account for thermomechanical *coupling* effects, such as the generation and absorption of latent heat during transformation. It is worth mentioning that the energy balance equation would then include additional heat source and flux terms. Then, for example, the full heat equation for forward transformation could be stated as:

$$\rho c\dot{T} = -\nabla \cdot \mathbf{q} + \rho r + r^t_{fwd} - T\boldsymbol{\alpha} : \dot{\boldsymbol{\sigma}}, \tag{2.22}$$

where c is the specific heat capacity, $\mathbf{q}$ is the heat flux vector, ρr is the body heat source term, and $\boldsymbol{\alpha}$ is a tensor containing the thermal expansion coefficients. The forward transformation latent heat term of interest, r^t_{fwd}, is defined by:

$$r^t_{fwd} = (\pi_{fwd} - \rho\Delta s_0 T)\dot{\xi}, \tag{2.23}$$

where π_{fwd} is the thermodynamic driving force for forward transformation, and s_0 is the specific entropy at the reference state. It should be noted that the coupling term $T\boldsymbol{\alpha} : \dot{\boldsymbol{\sigma}}$ in (2.22), which represents the effect of elastic deformation on the generation of heat, usually produces values that are very small. Therefore, Abaqus does not account for this term in the heat equation.

Consideration of the additional terms in (2.22) *strongly* couples the mechanical and thermal responses of the material, and numerical computation of global structural response becomes more difficult. Specifically, convergence of the global Newton-Raphson iterative solver becomes strongly dependent on mesh refinement, time step size, and other FEA parameters, and may be prevented altogether.

In order to fully define this SMA constitutive model for use in an Abaqus analysis, the following material properties and model parameters must be calibrated to experimental data and then specified in the custom user-defined material table in

Abaqus:

- E_A, E_M — the elastic moduli for austenite and martensite, respectively,
- C_A, C_M — the stress influence coefficients (the slopes of the transformation surfaces) [46],
- M_s, M_f, A_s, A_f — the zero-stress transformation temperatures,
- ν — Poisson's ratio, assumed to have the same value for austenite and martensite,
- n_1, n_2, n_3, n_4 — four smooth hardening parameters [22], [66],
- H^{max} — the maximum transformation strain.

The notation used here will appear in following chapters to define the SMA used in each example engineering problem.

B. Modeling Fluid-Structure Interaction

In certain cases, it is important to account for the two-way interaction between the structure of interest and the dynamic environmental conditions surrounding it. For example, in Chapter V the goal is to consider the effect of fluid flow on an SMA actuated morphing aerostructure, and vice versa. This involves a complex structural analysis of an SMA actuated morphing aerostructure exhibiting nonlinear actuation characteristics, subjected to variable surface pressures that depend on the surrounding air flow. This section describes the computational tools used to analyze the FSI for this particular engineering problem.

1. Computational Fluid Dynamics

The Abaqus/CFD module is a recent addition to the Abaqus Unified FEA suite that can solve a broad range of incompressible flow problems. Features of this module include laminar and turbulent flow, thermal convective flows, and the ability to actively deform the fluid mesh [31]. The CFD module uses a hybrid discretization scheme to formulate the Navier-Stokes momentum and pressure equations, (2.24) and (2.25) respectively, for arbitrarily deforming domains:

$$\rho(\frac{\partial \dot{\mathbf{u}}}{\partial t} + \dot{\mathbf{u}} \cdot \nabla \dot{\mathbf{u}}) = -\nabla p + \mu \nabla^2 \dot{\mathbf{u}} + \mathbf{f}, \tag{2.24}$$

$$\nabla \cdot (\frac{1}{\rho} \nabla p) = \nabla \cdot (\mathbf{f} - \dot{\mathbf{u}} \cdot \nabla \dot{\mathbf{u}}), \tag{2.25}$$

where ρ is fluid density, $\dot{\mathbf{u}}$ is the velocity vector, p is the pressure, μ is dynamic viscosity, and $\mathbf{f}$ is an applied body force. The $\dot{\mathbf{u}} \cdot \nabla \dot{\mathbf{u}}$ and $\mu \nabla^2 \dot{\mathbf{u}}$ terms from (2.24) are also known as the *advective* and *diffusive* terms, respectively. The finite volume method is applied to the momentum equation (2.24) with a Discontinuous-Galerkin formulation, resulting in the following integral form over the arbitrary domain Ω:

$$\int_\Omega \Phi \left(\rho(\frac{\partial \dot{\mathbf{u}}}{\partial t} + \dot{\mathbf{u}} \cdot \nabla \dot{\mathbf{u}}) + \nabla p - \mu \nabla^2 \dot{\mathbf{u}} - \mathbf{f} \right) \, \mathrm{d}\Omega = 0, \tag{2.26}$$

and the finite element method is applied to the pressure equation (2.25) with the Galerkin FEM formulation, resulting in the following form:

$$\int_\Omega \Psi \left(\nabla \cdot (\frac{1}{\rho} \nabla p) - \nabla \cdot (\mathbf{f} - \dot{\mathbf{u}} \cdot \nabla \dot{\mathbf{u}} \right) \, \mathrm{d}\Omega = 0. \tag{2.27}$$

The final spatially discretized forms are:

$$\mathbf{M}\ddot{\mathbf{u}} + A(\dot{\mathbf{u}})\dot{\mathbf{u}} + K\dot{\mathbf{u}} + Gp = \mathbf{F}, \tag{2.28}$$

$$Lp = D\mathbf{M}^{-1}(\mathbf{F} - K\dot{\mathbf{u}} - A(\dot{\mathbf{u}})\dot{\mathbf{u}}) - \dot{g}, \tag{2.29}$$

where $\mathbf{M}$ is the mass matrix, $A(\dot{\mathbf{u}})$ is the advection operator, K is the viscous diffusion operator, G is the gradient operator, D is the divergence operator, L is the Pressure-Poisson operator, $\mathbf{F}$ is the body force vector, and g is given by:

$$g = D\dot{\mathbf{u}}. \tag{2.30}$$

It should be noted that the advective and diffusive terms from (2.24) are then temporally discretized using different schemes. The advective term is solved using an explicit time scheme, and therefore requires a stability condition called the Courant-Friedrichs-Lewy, or CFL condition. This is a dimensionless constant that is calculated using knowledge of the current mesh characteristics. For a 3-D mesh, the CFL number is determined with the following equation:

$$\Delta t(\frac{\dot{u}_x}{\Delta x} + \frac{\dot{u}_y}{\Delta y} + \frac{\dot{u}_z}{\Delta z}) \leq CFL, \tag{2.31}$$

where $\dot{u}_x$, $\dot{u}_y$, and $\dot{u}_z$ are the three components of freestream velocity, and Δx, Δy, and Δz are the average dimensions of each element, and Δt is the next time interval which, subject to the value of CFL, will guarantee continued solution stability. Abaqus defaults to a fixed value of $CFL = 0.45$, which is sufficient for most CFD analyses. The diffusive term is temporally discretized using implicit methods as exemplified here for velocity:

$$\frac{\dot{\mathbf{u}}_{n+1} - \dot{\mathbf{u}}_n}{\Delta t} = (1-\theta)\ddot{\mathbf{u}}_n + \theta\ddot{\mathbf{u}}_{n+1}, \tag{2.32}$$

where θ may be specified as one of the following to indicate the implicit scheme:

- $\theta = 1$ (Backward Euler)
- $\theta = \frac{2}{3}$ (Galerkin)
- $\theta = \frac{1}{2}$ (Crank-Nicolson)

The implicit scheme requires the specification of a divergence tolerance, and Abaqus automatically adjusts the time intervals according to this tolerance and the specified CFL number.

The pressure and momentum equations are assembled as separate linear systems of equations and solved using separate iterative linear solvers, each of which require specification of the convergence limit. Unfortunately, the overall iterative solution process used by the Abaqus/CFD global solver is not made apparent in the Abaqus documentation [31]. However it is assumed here that Abaqus/CFD uses the Semi-Implicit Method for Pressure-Linked Equations (SIMPLE) algorithm, which is a robust method used by many commercially available CFD codes for calculating pressure, velocity, and other transport variables for an incompressible flow [67].

The general iterative solution process for the SIMPLE algorithm is shown in Fig. 7. At the beginning of any given time increment, the initial solution iterate value is set as $i = 0$ and the initial/boundary conditions are used to determine guess values for the pressure scalar p^*, velocity vector $\{\dot{u}\}^*$, and other transport variables $\{\phi\}^*$ that pertain to turbulence or energy (temperature) models, if enabled. These values are passed to the momentum equation solver, which by default is a Diagonally Scaled Flexible Generalized Minimum Residual (DSFGMRES) linear solver for

Abaqus/CFD [31]. The momentum equation solver is itself an iterative process which terminates and outputs a corrected velocity vector $\{\dot{u}\}_i$ once the norm of the solution residual $\{R_v\}$ and the suggested correction $\{c_v\}$ from the previous iteration are internally evaluated to be lower than specified tolerances. Using the updated velocity vector, the Abaqus/CFD pressure equation solver uses an algebraic multi-grid (AMG) accelerator [31] to calculate updated pressure scalars p_i, terminating when the norm of its solution residual $\{R_p\}$ and the suggested correction $\{c_p\}$ from the previous iteration are evaluated to be lower than specified tolerances. The updated variables $\{\dot{u}\}_i$ and p_i are used to correct the momentum and pressure equations again and, based on these updated variables, the other transport variables $\{\phi\}_i$ are calculated using their own respective solvers. Total solution divergence $\{R_{sol}\}$ for the time increment is then measured and, if it is more than the specified convergence limit, then the next global solution iteration begins for this same time increment using p_i, $\{\dot{u}\}_i$, and $\{\phi\}_i$ as the new guess values. If total solution divergence is less than the tolerance, the process exits, time is incremented, the boundary conditions are ramped (or held constant for a steady-state analysis), and the field output variables are output.

Unlike Abaqus/Standard, however, the global CFD solution process does not automatically terminate if the solution appears to be diverging or aggregating error over successive time increments. Monitoring the convergence of the time-marching solution is left up to the user. To help with this, Abaqus/CFD outputs in real-time the root-mean-square divergence over the entire domain. It is suggested [31] that divergence values of O(1) are indicative of a diverging solution and that perhaps some boundary conditions were incorrectly specified or a bad element was generated somewhere within the mesh. Also output in real-time is the kinetic energy of the entire system, which can indicate when a solution has reached steady state as the values asymptotically approach some limit.

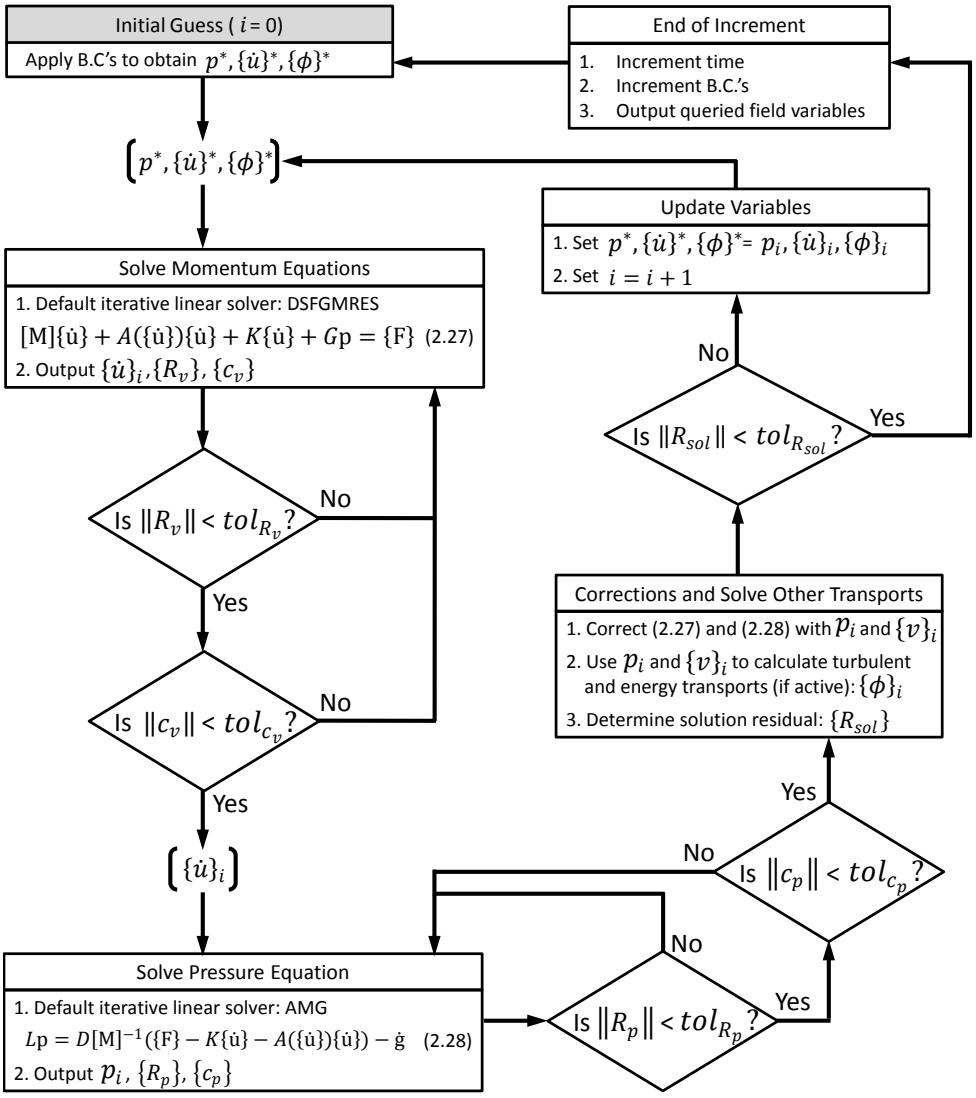

Fig. 7. The iterative solution-finding process for the SIMPLE incompressible fluid solver.

Currently there are three linear elements available for meshing fluid domains in Abaqus/CFD: the `FC3D4` tetrahedron, the `FC3D6` prism, and the `FC3D8` brick. These elements are illustrated in Fig. 8. Note that since the momentum equation is formulated using the finite volume method, the fluid velocity degree of freedom is evaluated at a single point located at the centroid of the element, while fluid pressure is evaluated at each node.

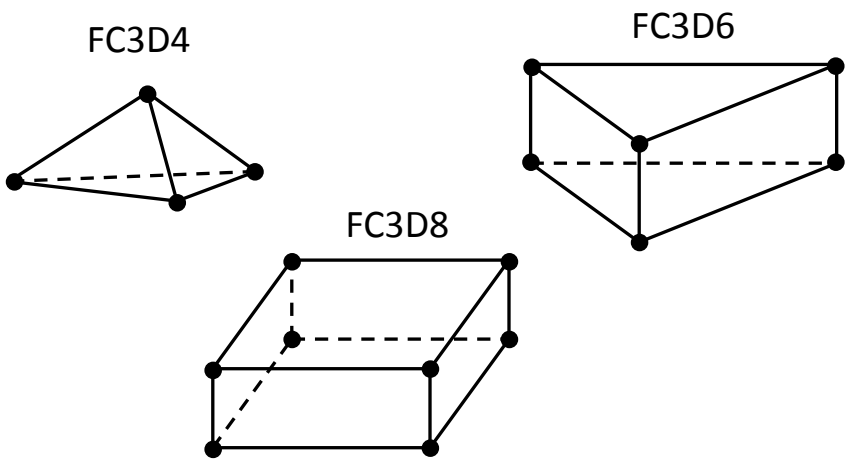

Fig. 8. Linear continuum fluid elements for Abaqus/CFD.

2. The Fluid-Structure Interaction Cosimulation Engine

To analyze FSI, we turn to the cosimulation capabilities of the Abaqus Multiphysics suite [31], which simplifies the complex multiphysical coupling between the solid and fluid domains by managing two distinct solvers: Abaqus/Standard (FEA) and Abaqus/CFD. In this sense, separate solid and fluid models, the governing equations of which remain isolated and uncoupled, are constructed and analyzed in parallel. However, during the cosimulation, each simulation exchanges pertinent model data across a specified surface: the *Fluid-Structure Cosimulation* boundary. This exchange

of data is done through a cosimulation engine (CSE), which is illustrated in Fig. 9 for a dynamic implicit analysis. In Fig. 9(a), the CSE is responsible for receiving pressure and wall shear stress nodal data from the fluid-side FSI surface, and then translating this data into equivalent concentrated nodal forces to be mapped onto the solid-side FSI surface. The FEA global solver calls for an evaluation of the thermomechanical response of the SMA components by invoking the full 3D SMA constitutive model [68], described in Chapter II, Section A.2., that was implemented in the form of a custom user-defined material subroutine (UMAT) coded in Fortran. The UMAT calculates the resultant stresses given strain values at every material point and at every increment in the analysis. The CSE is also responsible for translating solid-side FSI nodal displacements and velocities to update the fluid velocity and location of FSI surface nodes (i.e. morph the mesh) on the fluid-side, as shown in Fig. 9(b).

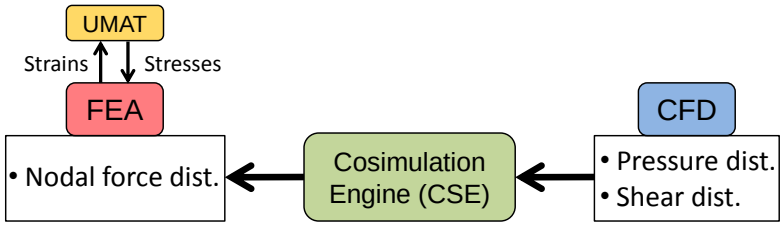

(a) CSE translating fluid model output data.

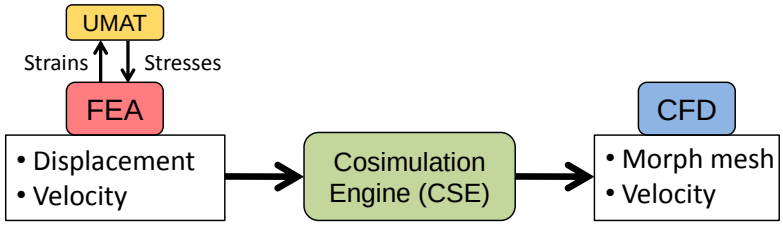

(b) CSE translating solid model output data.

Fig. 9. Illustration of the cosimulation data exchange through the CSE.

Translation of field output data through CSE occurs at a user-specified frequency

regulated by a Gauss-Seidel time-marching algorithm [31] shown in Fig. 10. In this sequential time-marching scheme, both FEA and CFD solve for the first time increment i using initial boundary conditions at the FSI surface. FEA solves for the next increment $i+1$ using traction vectors translated from the CFD pressure solution p_i from the initial increment. The FEA solver then updates the displacement and velocity of the FSI surface nodes u_i and passes these values to CFD to solve the pressure and shear values p_{i+1} for the next increment. It is important to note that CFD requires very small time increments (on the order of 10^{-7} seconds) to maintain a sufficiently low RMS divergence. Thus, the fluid model uses more time increments than FEA in between rendezvous points, a process called *subcycling*.

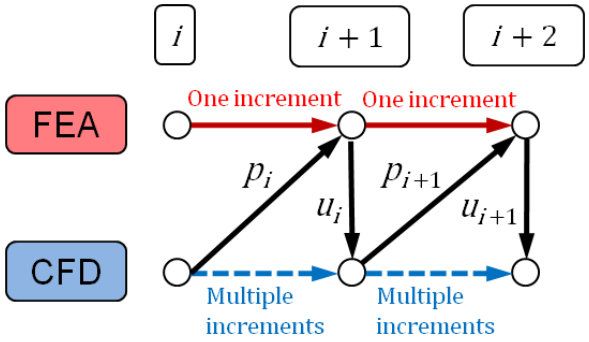

Fig. 10. The Gauss-Seidel time-marching scheme.

The analysis and optimization tools that constitute the expanded modeling and design framework have been fully introduced and described in detail. In the following three chapters (III, IV, and V) we now demonstrate the selective use of these tools on example engineering problems that are motivated by real SMA-actuated morphing aerostructure designs.

C. Design Optimization By Iterative Analysis

One of the most powerful features of the expanded modeling framework presented in this thesis is the capability to iteratively optimize a design using automated analysis tools. The tool of choice here is ModelCenter from Phoenix Integration [69], which is a commercially available software suite. Along with simulation management tools that allow it to integrate with other commercially available analysis tools, such as MATLAB, Abaqus, MS Excel, or any other program that can be executed through a custom batch file, ModelCenter also contains a wide array of design and optimization algorithms. Included are genetic- and gradient-based optimization algorithms, as well as design of experiment and probabilistics tools. Also included is the Design Explorer tool suite that is specially formulated to handle the exploration of erratic design spaces.

The integration of Abaqus into ModelCenter's simulation management process is accomplished through the use of command scripting. Abaqus has the capability to create macros of the model generation and execution process, recording scripts coded in the Python language. This "main script" can then be invoked with different input variables to quickly regenerate a new model with different dimensions, material properties, or boundary conditions. Additional scripts, called "utility scripts", can be created to link with the main script and, upon completion of a successful analysis, open and extract analysis information from the output database (`.odb`) file.

When Abaqus FEA and CFD are linked with ModelCenter, the simulation process manager, as illustrated in Fig. 11, takes control of the execution of the main scripts and input variables and also reads pertinent analysis data generated by the output database and extracted by the utility script. For an optimization study, the user specifies the design objective (maximize utility or minimize cost, as defined by

the user in the utility script), the hard constraints on the input design variables, and the limits of the design space. The process begins by executing the main python scripts in the Abaqus CAE pre-processing environment to generate the models, considering the specified input design variables. Analysis of the generated models follows. Then the output data of interest (maximum stress/strain in the FEA model, nodal displacements, CFD fluid velocities, and performance metrics are just a few examples) that are extracted by the utility script is read by the simulation process manager. This data is processed by the chosen optimization algorithm so that ModelCenter can formulate a new suggested set of design variables, or *design vector*, for the next analysis iteration. This process continues until the optimization algorithm converges upon an optimized design solution that meets the constraint criteria. At this point, several post-processing and visualization tools are available to analyze the output data.

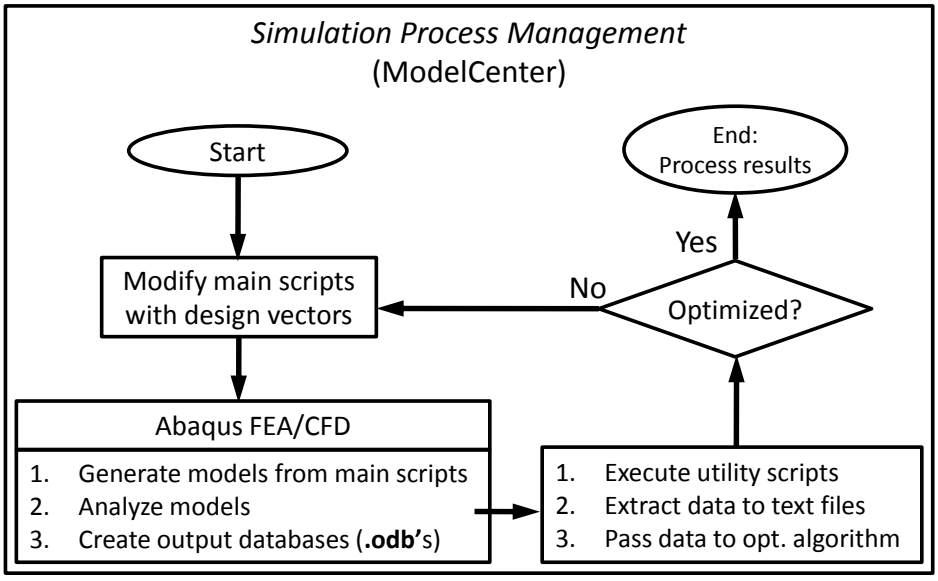

Fig. 11. The automated, iterative optimization process of an FEA model.

Note that, while ModelCenter is used in this work, other simulation management programs exist that contain similar capabilities, such as Simulia's Isight program [70]. The version 6.11 release of the Abaqus FEA suite also includes a topology optimization module internal to the program called ATOM that can remove or add material from a model based on constraints specified by the user [31]. However, it is currently unable to handle a model that references a custom UMAT.

Two of the available optimization algorithms are used extensively in the example engineering problems in Chapters III and IV: gradient and Design Explorer. The gradient algorithm calculates the gradient at a point in the design space and proceeds to take steps proportional to that gradient, in the direction of a minima or maxima, in order to progress towards an optimized design [69]. For most simple applications, where the design space is continuous or contains only a single minimum or maximum, gradient-based optimization algorithms are very useful and can be expected to converge upon the same optimized design solution regardless of the chosen initial design vector. However, for complex applications where the design space is erratic or discontinuous, gradient optimization algorithms are prone to falling into local minima and thus the optimized design solution is no longer independent of initial design vector. Given the nonlinear nature of SMAs, the highly variable environments these active components are subjected to, and the potential for intermittent failure of the FEA model, it is clear that a robust optimization algorithm is necessary. Fortunately, certain optimization algorithms have been developed with these needs in mind. The Design Explorer tool suite, originally developed by the Boeing Company, combines design-of-experiment sampling and advanced surrogate modeling techniques to overcome issues that are particularly problematic for gradient-based methods: discontinuous design spaces, noisy cost functions, long run times, and the potential for intermittent analysis failure.

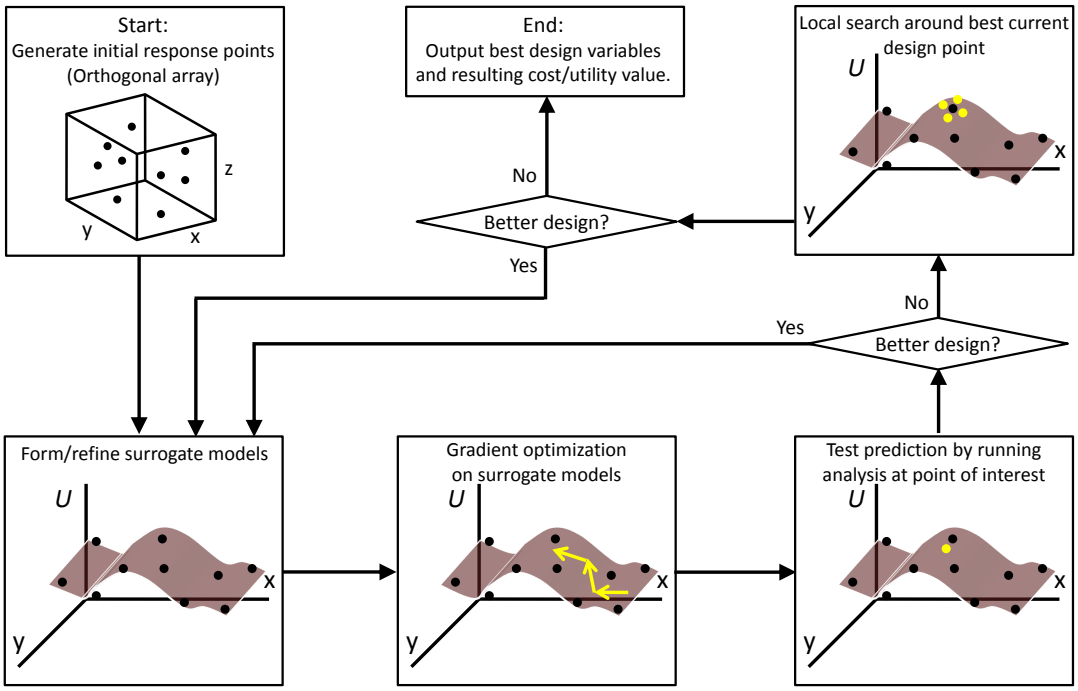

Fig. 12. The Design Explorer optimization process.

The process used by Design Explorer to arrive at an optimized design solution is illustrated in Fig. 12 for an example case where some arbitrary performance metric "utility" (U) must be maximized[3]. At the beginning of the optimization study, Design Explorer samples the design space in an orthogonal array to generate initial response data points [69]. The algorithm then builds surrogate models based on successfully generated response data and predicts optimal design solutions through gradient-based optimization over the surrogate surfaces. Design Explorer then tests its prediction and iteratively refines its surrogate models by running FE analysis at and near potential

[3]It is also common to formulate an objective function as "cost" (C), as is the case in the example problem in Chapter IV. The user must then take care to specify that the objective be *minimized* in Design Explorer in order to arrive at an optimized design solution.

design solutions. This process continues until a local search around a potential design solution does not yield a higher evaluation for U.

CHAPTER III

DESIGN OPTIMIZATION OF A THERMOMECHANICALLY COUPLED SMA FLEXURE FOR A MORPHING AEROSTRUCTURE*

It was noted in Chapter I that, while SMAs are space-saving, solid-state actuators that can provide motion while under very high loads, the rate of thermally-induced SMA transformation is significantly hindered by low thermal conductivity and latent heat effects observed in the material. The relatively long cooling times observed in SMA geometries such as beams and tubes make it difficult for controlled devices to operate with sufficiently high frequency. Therefore, the application of SMA beams as aerospace control actuators has been limited. Morphing structures such as flight control mechanisms require higher cyclic actuation frequencies than are commonly observed in SMAs, and thus have motivated the effort to increase thermal actuation rates attainable in SMA active components.

The following *component*-focused study utilizes the expanded modeling framework that was outlined in Chapter I and detailed in Chapter II. The goal is to design *hybrid* SMA actuators that contain conductive materials to counteract the poor thermal qualities of the SMA, thereby increasing actuation speed. Here, a comparative analysis is conducted to specifically measure increased actuation rates of these hybrid aerostructures. This study addresses the design tradeoffs between component weight, actuation speed, and transformation displacement as they are affected by the type and distribution of secondary conductive materials exposed to non-uniform, transient heat flux. Finite element analysis (FEA) and two optimization algorithms are used

---

*Reprinted with permission from "Analysis and Optimization of Improved Hybrid SMA Flexures for High Rate Actuation" by Stephen D. Oehler, Darren J. Hartl, and Dimitris C. Lagoudas, 2011. Proceedings of SPIE, Vol. 7979, Copyright 2011 by SPIE.

to model the transient thermomechanical behavior of an SMA actuator and to find an optimized design solution in an automated manner. The pertinent aspects of the expanded modeling framework for this study are illustrated in Fig. 13.

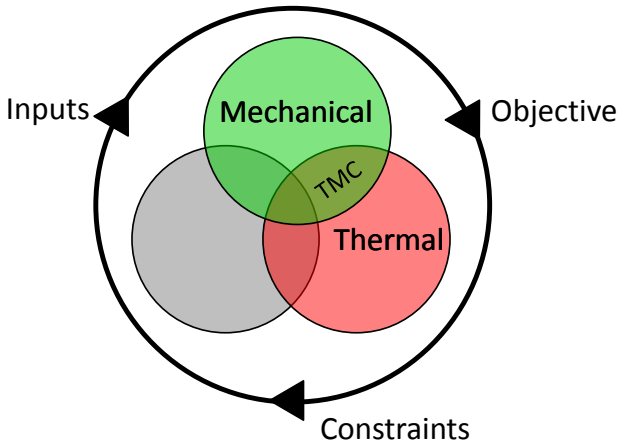

Fig. 13. Pertinent aspects of the expanded modeling framework for designing SMA actuating components (cf. Fig. 4).

The first section of this chapter briefly discusses the role of the original flexure in an aerostructure as the mechanism for assembly actuation. Associated subsections parameterize the proposed modified flexure geometry, present the FEA model, and describe the optimization design space. The second section outlines the procedure for analyzing three hybrid flexures, each with a different secondary material: aluminum, copper, or silver. A baseline analysis is conducted for the three flexures utilizing two models, one in which latent heat is neglected and the other in which it is evaluated, to demonstrate the error in approximating the thermomechanical coupling behavior. The optimized design solutions for each hybrid flexure are provided, along with graphical representation of tip deflection as a function of transformation cycle time.

A. Engineering Model and Analysis Tools

The actuator modeled in this study is derived from the flexures found on the Variable Geometry Chevron (VGC), the morphing aerostructure developed by Boeing [19] that was described earlier in Chapter I, Section A. Each flexure is a tapering beam with a solid rectangular cross section and formed from $Ni_{60}Ti_{40}$ (wt.%), an alloy that exhibits stable shape memory behaviors. Reverse transformation of the flexure toward a curved austenitic configuration is accomplished by activating a heat strip bonded to the top surface. The synchronized reverse transformation of all three mounted flexures results in deflection of the panel toward the axis of the engine. Here we present the model of the proposed hybrid flexure formed by removing material from near the centroid of the original VGC part, creating what will be referred to as a "channel", and then adding back some amount of a non-active thermally conductive material to increase overall heat flux and thus decrease the time required to thermally transform the entire beam.

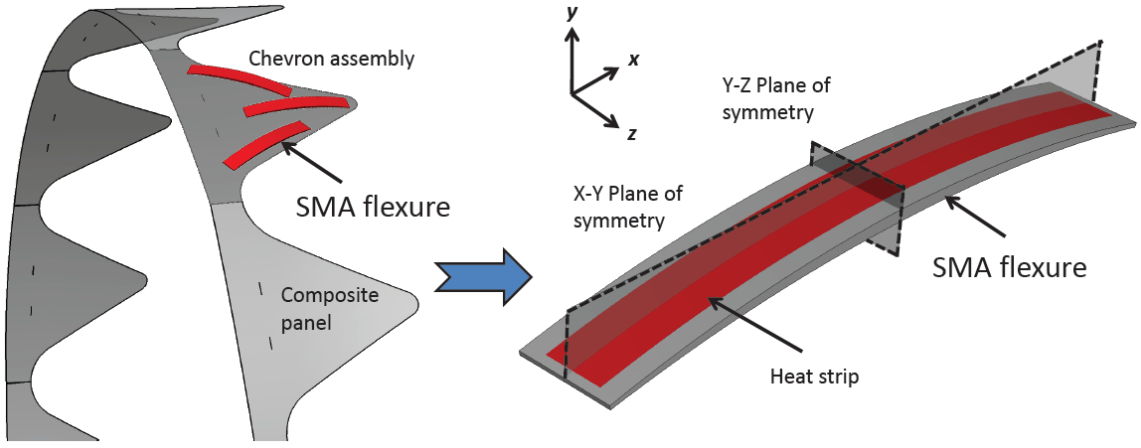

Fig. 14. Circumferential configuration of the 14 installed VGCs and detailed view of a single flexure.

1. Specific Analysis Tools

The goal here is to optimize the design of a thermally actuated smart structure (the flexure) composed of SMA. The set of analysis tools introduced in Chapter II are utilized to reach this goal: the finite element framework for assessing the thermal and mechanical response of each design (Chapter II, Section A.1), the thermomechanically coupled constitutive model for capturing the unique material behavior being exploited (Chapter II, Section A.2), and the design framework for considering multiple design configurations in an efficient manner (Chapter II, Section C). For the FEA model, the flexure geometry described in the next section is discretized using the Abaqus/Standard `C3D20RT` elements. Recall that these are hexahedral continuum elements with quadratic formulation and reduced integration that consider both displacement and temperature degrees of freedom. Also recall that consideration of a thermomechanically coupled material may prevent an analysis from converging depending on the definition of certain FEA parameters. For this reason, we will consider the use of two types of finite element analysis in the following section: one that considers the full and consistent constitutive model (including the latent heat term, heat transfer, and a constant specific heat), and one that neglects the latent heat term while still considering heat transfer and a constant specific heat. The impact of this simplification is quantified in the following section.

2. Model Geometry and Materials

The original curved and tapered VGC flexure has two planes of symmetry as seen in Fig. 14. Due to this symmetry, only a quarter of the hybrid flexure need be modeled; a solid quarter model of the hybrid flexure is shown in Fig. 15. In contrast to the solid SMA flexure from the VGC, the hybrid flexure has an SMA cross-section

similar to that of an I-beam with SMA webs and flanges. This is shown in more detail in Fig. 16. The space between the webs and flanges (the channel) consists of a secondary thermally conductive material layer adjacent to the SMA in addition to a void region. The three secondary materials considered in this particular study were chosen to provide low mechanical resistance during component actuation (i.e. to have a low stiffness) while efficiently channeling heat into and out of the SMA material.

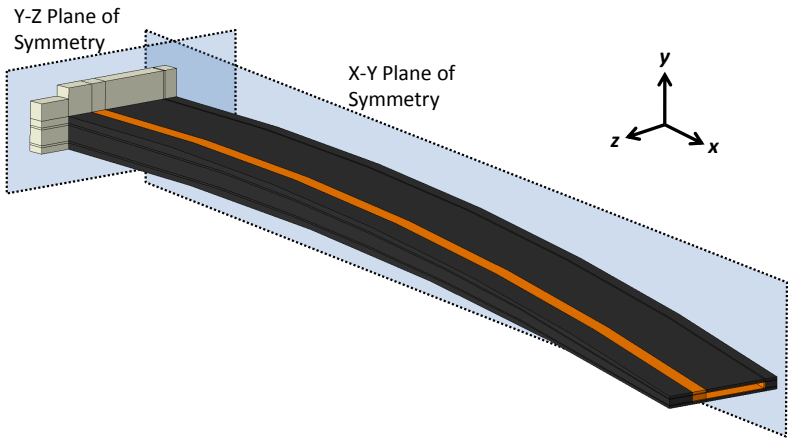

Fig. 15. Modeled hybrid flexure and the two planes of symmetry.

To effectively remove heat from the hybrid flexure in a global sense, we consider an aluminum clamp attached at the Y-Z plane of symmetry, as shown in Fig. 15 and Fig. 16. We imagine the flexure-clamp assembly as installed on the original Boeing VGC, where the upper-most surface of the aluminum clamp could be exposed to the free stream throughout the entirety of flight. As it is also in contact with the conductive material, the collar can act as an efficient route for conducting heat energy out of the hybrid flexure. For heating, we consider the effects of a surface-bonded resistive heater, as was used in the original VGC design (see Fig. 14).

To geometrically define the model, the dimensions of the base geometry are

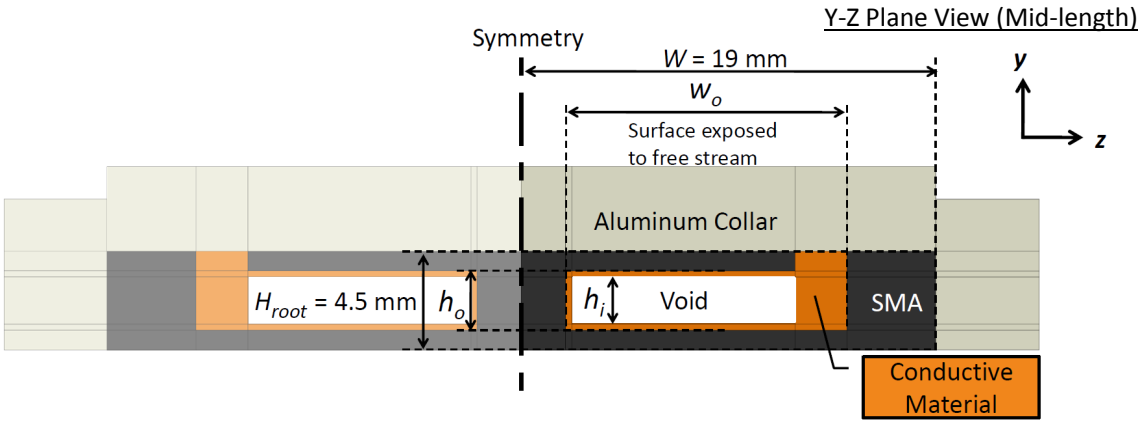

Fig. 16. Y-Z plane view of the hybrid flexure at the mid-length (cf. Fig. 14,15).

parameterized such that SMA and secondary material distribution through the cross-section can be defined by three dimensions at the root: channel height h_o, channel width w_o, and secondary material layer thickness l_{therm}. These dimensions, illustrated in Fig. 16, are related to normalized and bounded geometric ratios h_i/h_o, h_o/H, and w_o/W through the following relations:

$$h_o = H\frac{h_o}{H}, \tag{3.1}$$

$$w_o = W\frac{w_o}{W}, \tag{3.2}$$

$$l_{therm} = \frac{1}{2}(h_o - H\frac{h_i}{h_o}\frac{h_o}{H}), \tag{3.3}$$

where W and H are the width and local height of the flexure cross section, respectively, as seen in Fig. 16. The flexure is geometrically partitioned such that the local ratios h_i/h_o, h_o/H, and w_o/W remain constant along the length of the flexure, and these

will become the three design variables explored during the optimization process.

The material properties for the three thermally conductive secondary materials are provided in Table I [71]-[73]. For each material, the density ρ, Young's modulus E, Poisson's ratio ν, thermal conductivity k, specific heat c_p, and yield stress σ^Y are given. Note that plastic behavior of each material assumes a Mises-type yield criterion with an associated flow rule and isotropic hardening as indicated in the relevant literature sources. The material properties for the $Ni_{60}Ti_{40}$ (wt.%) SMA are provided in Table II [22], [74]. Additional SMA properties are required to account for the martensitic transformation and these are described elsewhere [22]. Note the difference between the poor thermal conductivity of the SMA from Table II as compared to the conductivity of the secondary materials in Table I.

Table I. Material properties for each of the considered thermally conductive secondary materials [71]-[73].

Property	Aluminum	Copper	Silver
ρ [kg/m^3]	2700	9200	10500
E [GPa]	69	117	83
ν	0.33	0.34	0.37
k [W/m-K]	250	400	430
c_p [J/kg-K]	890	390	230
σ_{yield} [MPa]	290	138	50

Finally, we validate that the response of an SMA flexure of the given geometry and material properties from Table II, modeled using the Abaqus FEA software suite

Table II. Material properties for $Ni_{60}Ti_{40}$ (wt.%) shape memory alloy [22], [74].

Property	Value	Property	Value
ρ [kg/m^3]	6450	M_s [°C]	35
E_A [GPa]	90	M_f [°C]	-31
E_M [GPa]	62.85	A_s [°C]	15
k [W/m-K]	22	A_f [°C]	70
c_p [J/kg-K]	329	$C_A\|_{300\text{MPa}}$ [MPa/°C]	16
ν	0.33	$C_M\|_{300\text{MPa}}$ [MPa/°C]	10
n_1, n_2, n_3, n_4	0.6, 0.2, 0.2, 0.3	$H^{cur}(\overline{\sigma})$	$0.0158[1 - e^{-\frac{675\overline{\sigma}}{E_A}}]$

and custom constitutive model, accurately predicts known behavior. We compare the numerical results of the FEA model shown in Fig. 17 with experimental data from another work by Hartl et al. [22] that determined the thermomechanical actuation response of an identical physical flexure under two different loading conditions applied at the center of the flexure: the first a constant distributed load of 90 N, the second a spring load with constant $k \approx 63\,\text{N/mm}$ [22].

The conditions for each analysis step are chosen to mimic the thermomechanical loading path of the flexure as seen in the experiment [22]. For both FEA models, these steps are as follows:

1. Boundary conditions are applied: two corners of the flexure are pinned at one end, and the other two corners are constrained from vertical displacement at the other end. The load P is applied along the center while the flexure temperature is kept above A_f ($T > 70$°C).

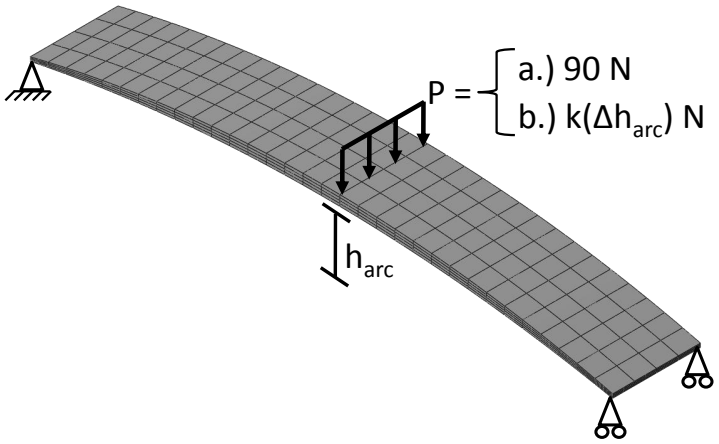

Fig. 17. FEA model for validating the thermomechanical actuation response of the SMA flexure.

2. Flexure temperature is decreased to below M_f ($T < -31°\text{C}$).

3. Flexure temperature is increased to above A_f ($T > 70°\text{C}$).

The numerical results, showing the deflection at the center of the flexure over the actuating temperature range, are plotted in Fig. 18 against the experimental data found from the works of Hartl et al. [22]. As can be seen from both plots, there is excellent agreement between the FEA model and experiment.

3. Initial and Boundary Conditions

The hybrid flexure model described in this study considers the application of thermal and mechanical boundary conditions motivated by the operational conditions of the VGC flexure [19]. The analysis procedure is divided into three steps: *Load*, *Cool*, and *Heat*. Prior to loading, all boundary conditions, local transformation states, and local temperatures are initialized. An initial uniform temperature field of 127 °C is assumed. Thus, the flexure reference configuration corresponds to that of an unstressed

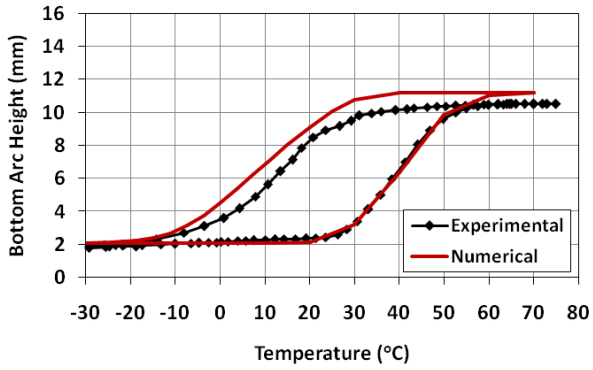

(a) 90 N constant load

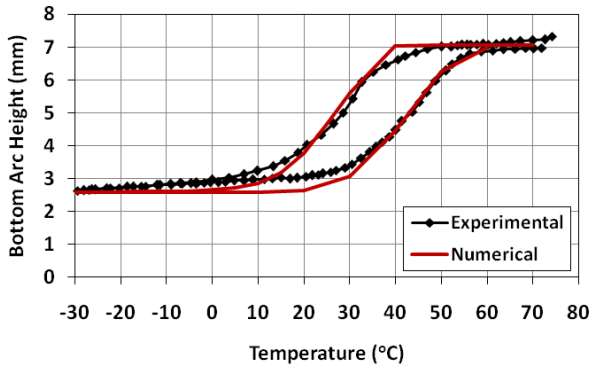

(b) 63 N/mm variable load

Fig. 18. Comparing numerical results with experimental data [22] for identical SMA flexures.

and fully austenitic state.

Several mechanical boundary conditions are applied to exploit the geometric symmetries. Since the component is modeled as a quarter-symmetric flexure, the nodes at the planes of symmetry are restricted from translating out of plane and are restricted from rotation except about the vector normal to the planes. In addition, a small area underneath the root of the flexure is fully constrained to account for adhesion to the chevron panel [75]. Finally, a vertically oriented spring element is

kinematically coupled at one end to all flexure tip nodes to replicate the elastic biasing load caused by the stiffness of the chevron substrate on a quarter of the flexure, approximated as $k \approx 15.75\,\mathrm{N/mm}$ [22]. At the beginning of the load step, the free node of this spring is vertically displaced by 1.42 cm and held for the remainder of the analysis, approximating the fastening of the precurved flexure to the flat VGC substrate. This is schematically illustrated in Fig. 19.

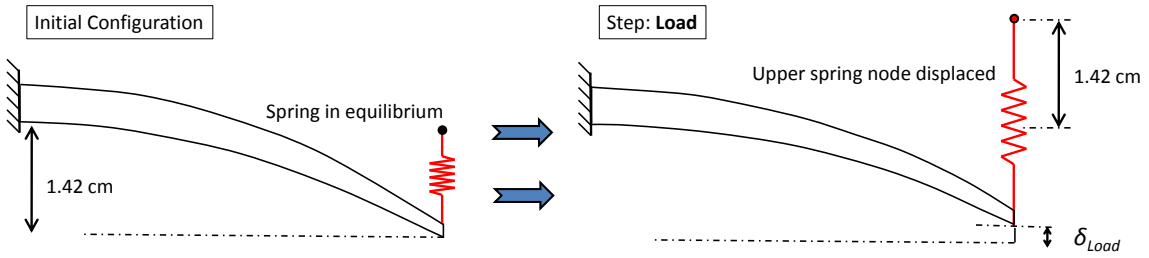

Fig. 19. Mechanical boundary conditions applied during the loading step.

The forward transformation of the hybrid flexure occurs during the cooling step, which spans a maximum of 1000 seconds. Thermal boundary conditions for flexure cooling are derived assuming component operation at aircraft cruise conditions associated with an air velocity of Mach 0.8 and an altitude of 10,668 m (35,000 ft). The surface film coefficient for the top surface of the aluminum collar is approximated by using the Nusselt Number, N_u, for turbulent flow over a flat plate of similar dimensions for this step:

$$h = \frac{N_u k}{L}, \tag{3.4}$$

where h is the surface film coefficient, and k and L are the thermal conductivity and length of the plate, respectively. An empirically-derived equation [76] is chosen to determine the Nusselt Number:

$$N_{u,turb} = 0.0296 Pr^{1/3} Re^{4/5}, \tag{3.5}$$

where Pr and Re are the Prandtl and Reynold's numbers, respectively. The environmental conditions associated with the cruise stage of aircraft flight pattern determine the magnitude of these numbers through the following relations:

$$Pr = \frac{\mu c_p}{k}, \tag{3.6}$$

$$Re = \frac{u \rho L}{\mu}, \tag{3.7}$$

where u, ρ, μ, and c_p are the velocity, density, dynamic viscosity, and specific heat of the surrounding air at aircraft cruise conditions. Given the properties of air at these conditions [77], the surface film coefficient of the top surface of the aluminum collar is determined to be $h \approx 960$ W/m^{2}K. A sink temperature of -55°C is assumed per standard atmospheric conditions [77]. This surface convection boundary condition is active during both the cooling and heating steps of the analysis, while all other surfaces are assumed to be thermally insulated.

Reverse transformation occurs during the heating step, which spans at most 2000 seconds. To emulate the heat strip mentioned previously, 5 W of total power is applied over the rectangular area spanned by the fixed length of the flexure (root to tip) L and channel width w_o, which is a design variable and thus changes over the course of optimization. The applied heat flux density ϕ_q (with units: W/m^2) is then related to these two dimensions per the following:

$$\phi_q = \frac{Q}{L w_o}, \tag{3.8}$$

where Q is the total heater power (5 W). The thermal boundary conditions ap-

plied during steps *Cool* and *Heat* are illustrated in Fig. 20.

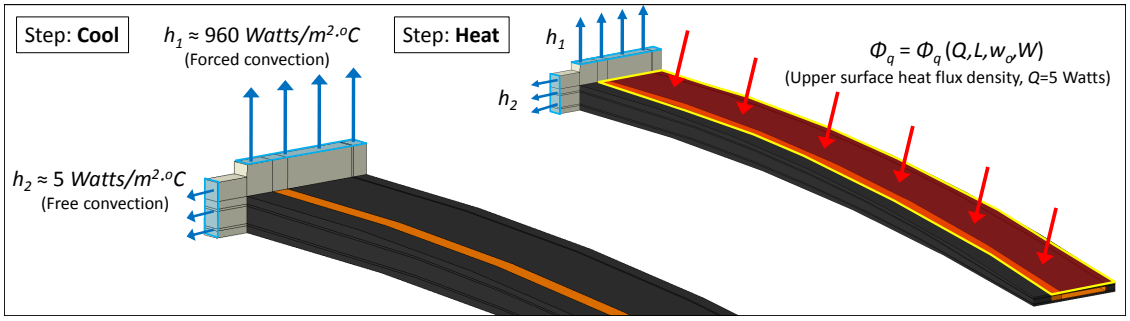

Fig. 20. Thermal boundary conditions active during cool and heat steps.

4. Optimization Statement

As stated earlier, for the current design and optimization study, three normalized parameters are used to define the geometry of the model: h_i/h_o, h_o/H, and w_o/W. These design variables constitute the design space over which the component actuation performance is optimized for each of the three materials.

The objective considered here is to maximize overall flexure performance during actuation. Note that, even though the design of the hybrid flexure is motivated by the poor actuation rate of the original all-SMA flexure, the objective is not the simple minimization of actuation time. We instead consider the capability of the flexure to provide work against the spring, albeit in a timely manner. We also consider the effects of reducing the amount of internally distributed, thermally conductive material on component mass, as the weight of operating components has direct effect on aircraft fuel consumption. The objective function is therefore measured according to a power-to-mass ratio, or the cyclic power of actuation P_{cyc} divided by total component mass m_{tot}. This objective function can be restated in terms of output work done against

the spring W_{rev}, total transformation time t_{tot}, and component mass m_{tot}:

$$\frac{P_{cyc}}{m_{tot}} = \frac{W_{rev}}{t_{tot} m_{tot}}, \tag{3.9}$$

where each argument is assessed using the following:

- W_{rev}: the output work done against the spring during reverse transformation; calculated using beam tip deflections and the spring constant,
- t_{tot}: the total transformation time; the sum of forward and reverse transformation times,
- m_{tot}: the total mass of the entire actuator (includes the SMA, conductive material, and aluminum collar).

It is important to note that the forward and reverse transformation times are calculated by measuring the amount of time needed to complete 95% of the actuation motion during cooling and heating, respectively. The total cycle time t_{tot} is the sum of these two. Thus, the optimal design solution is considered to be that which maximizes the objective power-to-mass ratio P_{cyc}/m_{tot}.

In addition to the objective function arguments, the maximum Mises stress found anywhere in the SMA at any time $\overline{\sigma}_{SMA}^{max}$ is also reported for each analysis of each geometric configuration for each of the three secondary materials. A design constraint of 300 MPa is imposed as an upper limit on $\overline{\sigma}_{SMA}^{max}$ [21]. No stress constraints are considered for the secondary materials, which are allowed to plastically yield during component actuation. The final design optimization problem statement is then summarized in Table III.

Table III. The design optimization summary for this morphing flexure study.

Objective:	
Maximize	P_{cyc}/m_{tot}
Input:	
	$0.1 \leq (h_o/H) \leq 0.9$
by varying	$0.1 \leq (h_i/h_o) \leq 0.9$
	$0.1 \leq (w_o/W) \leq 0.9$
Constraints:	
subject to	$\overline{\sigma}_{SMA}^{max} \leq$300 MPa

B. Analysis Procedures and Results

In this section we discuss preliminary analyses of a nominal baseline hybrid flexure design considering three secondary materials (aluminum, copper, and silver), followed by a design optimization study for each of the three material systems. The preliminary analyses assess the transformation times of the three hybrid flexures with consistent distributions of secondary material using both FEA types previously discussed: the full and consistent model and another that neglects the SMA transformation latent heat term in the energy balance equation. The cyclic transformation times predicted using these two methods are compared to demonstrate errors resulting from omission of the latent heat effects in transient analyses. Following this, an iterative scheme is used to explore the hybrid flexure design space to find the material distribution for each of the three hybrid flexures that maximizes the actuator power-to-mass ratio.

Prior to running FEA on the flexure model, however, it may be useful to quantitatively analyze these material properties for an example heat transfer scenario in

order to gain a better intuition of which secondary material will act as the best thermal channel. For this, we explore the ability of each material to diffuse thermal energy. Consider an initial-boundary value problem in which a material is undergoing a decaying temperature gradient. The 1-D heat transfer partial differential equation is:

$$\rho c_p \frac{\partial}{\partial t} T(x,t) = k \frac{\partial^2}{\partial x^2} T(x,t), \tag{3.10}$$

with the associated initial-boundary conditions:

$$T(x,0) = 100 \qquad T(L,t) = 0 \qquad T(0,t) = 0, \tag{3.11}$$

which corresponds to a material of dimension L that is initially and uniformly 100°C, with both sides exposed to an ambient temperature of 0°C. Using the separation of variables technique, the general solution to this equation is found to be:

$$T(x,t) = \sum_{i=1}^{n} \left(-\frac{200(-1+(-1)^i) sin\left(\frac{\pi i x}{L}\right) exp\left(\frac{-k\pi^2 i^2 t}{L^2 \rho c_p}\right)}{\pi i} \right). \tag{3.12}$$

The symbolic solver Maple 14 [78] is chosen to numerically sum the equation and solve for the time t at which the core temperature is near zero, or $T(\frac{L}{2}, t) \leq 1$°C. For a size of $L = 0.1$, we arrive at the values shown in Table IV for each of the three secondary materials. Also shown are the calculated values for the thermal diffusivity α of each material, given by:

$$\alpha = \frac{k}{c_p \rho}. \tag{3.13}$$

Note from Table IV that the materials have been ranked in order from slowest to fastest thermal diffusion, and that this ranking agrees with the α values for each

Table IV. Decaying temperature gradient solutions for each thermally conductive material.

Material	Time to 1°C [secs]	Diffusivity [10^{-4}]
Aluminum	47	1.04
Copper	44	1.11
Silver	28	1.78

* For an upper sum limit $n = 2000$

material. It is now apparent that silver is the most capable of diffusing thermal energy under the given conditions. It is also expected that the use of aluminum as a thermally conductive material in the hybrid flexure might not be the best design solution, with respect to copper or silver, if one is to maximize actuation frequency. However, these analytical results will be compared against FEA results in the following subsection to see if the 1-D heat transfer scenario is sufficient to intuit the performance of the three hybrid flexures.

1. Baseline Analysis

The preliminary numerical analyses consider hybrid flexures with a known and consistent geometric configuration and associated secondary material distribution, where all three design variables are equal:

$$\frac{h_i}{h_o} = \frac{h_o}{H} = \frac{w_o}{W} = 0.8. \tag{3.14}$$

Structural responses are predicted using models that alternatively neglect or account for the latent heat of transformation. The cyclic transformation times predicted using

each model and the relative error between them are shown in Table V for each of the secondary materials considered. The results of an additional analysis case for which the secondary material is taken to be SMA (and the void remains) is provided for comparison. These transformation times are subdivided into forward and reverse transformation contributions and are compared in Fig. 21. Additionally, the tip deflections of the baseline flexures over time are plotted in Fig. 22.

First, we note the substantial decrease in actuation time obtained when SMA material[1] is replaced with more thermally conductive material. Further, we note that the general trends are captured with the less computationally expensive (and more robust) model that neglects latent heat, the cycle time of the SMA actuator is extended by approximately 17% when this important term is considered. These latter findings are used in the design optimization study, where the "latent heat neglected" model is used to explore the overall design space and the consistent and more accurate "full model" is used to find a final optimized solution.

Table V. Observing the impact of neglecting latent heat effects on transformation cycle times for the baseline flexure configurations.

	Aluminum	Copper	Silver	SMA
Latent Heat Neglected	690 s	830 s	710 s	1440 s
Full Model	830 s	990 s	870 s	-
Error	17%	16%	18%	-

Another point of interest is that, according to Fig. 21, an aluminum-SMA hybrid

[1]Several convergence issues related to the global solver were encountered in using the full model to analyze the all-SMA flexures. As a result, only output from the "latent heat neglected" models exist for these cases.

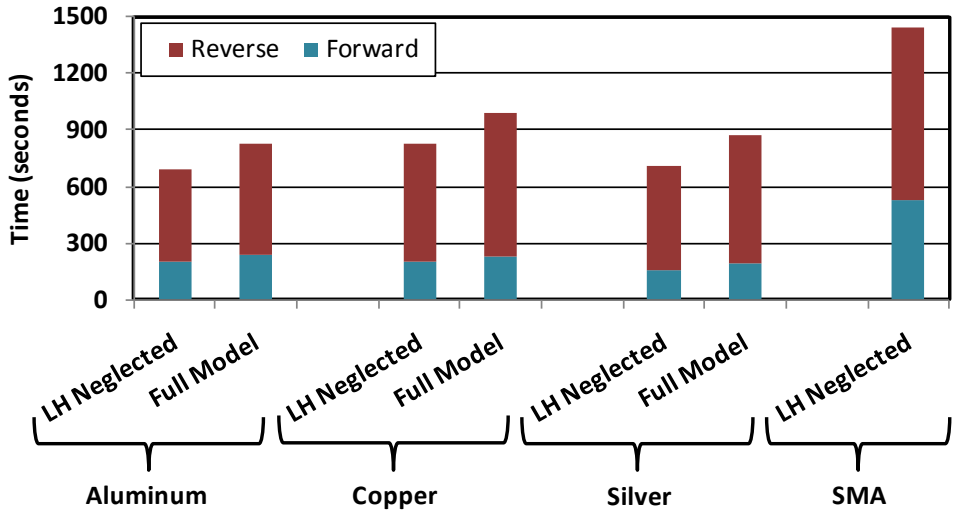

Fig. 21. Full transformation times for the baseline configuration.

flexure with an identical material distribution as the other two flexures has the smallest transformation time, and therefore has the highest actuation frequency. This is counter to our intuition, given the results from the 1-D heat transfer scenario hypothesized at the beginning of this section. In fact, it was predicted from Table IV that an aluminum-SMA hybrid flexure would have the poorest overall thermal qualities. A closer look at Fig. 22, however, shows that the combined mechanical properties of the aluminum and SMA cause the hybrid flexure to have a much lower overall tip displacement during actuation. The lower tip displacement of the aluminum-SMA flexure could be attributed to the relatively high yield stress of the aluminum. At stress levels lower than the aluminum yield stress, copper and silver are able to plastically deform and are therefore less of an impedance on SMA motion during transformation, and as a result the tip deflection is less affected. Since the rate of transformation for the aluminum-SMA flexure is much the same as the other two

flexures, this material combination is able to complete actuation more quickly.

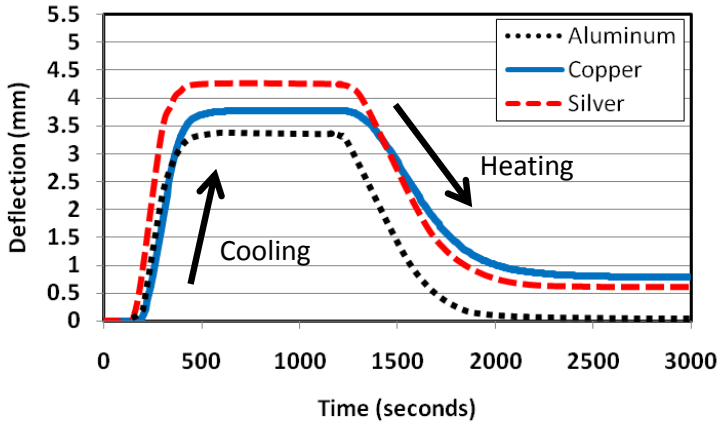

Fig. 22. Tip deflection of the baseline flexures over time (full model).

2. Optimization of Material Distribution

We then perform an automated study to determine the optimized design solutions for hybrid flexures including each of the three secondary materials. Because the evaluation of the latent heat significantly increases the analysis run time and may preclude convergence for some geometric configurations, the overall optimization procedure is divided into two steps. The first step neglects latent heat and finds approximately optimal design solutions for each flexure using an iterative algorithm that evaluates designs throughout the design space. The second step then refines the search by fully evaluating the contribution of latent heat, employing a gradient-based optimizer and using the result of the first step as its initial guess.

During the first step (latent heat neglected), the Design Explorer optimization option of the ModelCenter tool [69] is utilized. Recall from Chapter II, Section C, that Design Explorer is a fast and robust scheme for navigating the design space

towards some goal (i.e., maximizing P_{cyc}/m_{tot}). The algorithm proceeds to sample the design space via FEA, choosing design variable values based on previous design attempts and seeking the design with the maximum power-to-mass ratio that does not violate the specified design constraints. The three approximate optimized design solutions found using this "latent heat neglected" model are summarized in Table VI. The value of $\overline{\sigma}_{SMA}^{max}$ is reported to prove that constraints were satisfied.

Table VI. Optimization step one results: design variables, root dimensions, and response outputs for the approximate design solutions of each hybrid flexure (latent heat neglected).

Design Solution	Aluminum	Copper	Silver
h_o/H	0.82	0.57	0.63
h_i/h_o	0.90	0.90	0.90
w_o/W	0.90	0.87	0.90
l_{therm} [mm]	0.18	0.13	0.14
h_o [mm]	3.69	2.57	2.84
w_o [mm]	17.1	16.5	17.1
$P_{cyc}/m_{tot}[W/kg]$	17.5E-3	8.72E-3	9.97E-3
$\overline{\sigma}_{SMA}^{max}$ [MPa]	283	300	289

The second step employs the full phase transformation model (latent heat evaluated) in performing gradient-based design optimization [69]. The approximations provided by the first step (see Table VI) are used as the initial guesses for the second step. The gradient algorithm then samples the design space in a small region

surrounding the initial guess, estimating the local gradient of the objective P_{cyc}/m_{tot}. This information is used to choose a new design that maximizes the objective while satisfying design constraints. The process terminates when a higher power-to-mass ratio cannot be found. The three final optimized design solutions found using this full model are summarized in Table VII. The time vs. deflection response of each of these optimized designs are illustrated in more detail in Fig. 23. Flexure tip deflection over time is seen in Fig. 23(a). The total times to complete transformation, subdivided into forward and reverse contributions, are compared in the bar graph of Fig. 23(b).

It is seen from this data that the hybrid flexure with aluminum as the secondary material provides an optimized design solution with the highest power-to-mass ratio for the given search bounds. Considering the lower actuation deflection of the aluminum hybrid flexure, it is clear that this high measure of performance is due to the low density of aluminum. It is also worth noting that the two design variables h_i/h_o and w_o/W for aluminum and silver converged to values of 0.9. Since these values correspond to the upper search bounds of the design vector, we cannot determine if a better design solution with a potentially higher power-to-mass ratio exists where values of h_i/h_o and w_o/W are greater than 0.9. However, this still implies that a minimum of thermally conductive material is needed to increase the ability of the flexure to effectively diffuse heat energy. Finally, in comparing Table VI with Table VII, it is clear that only the optimal flexure design for copper changed substantially during the second optimization step. This highlights the utility of the faster approximate model for efficiently determining optimal designs. However, the consideration of latent heat decreased all three power-to-mass ratio predictions noticeably (see Table VII).

Table VII. Optimization step two results: design variables, root dimensions, and response outputs for the final optimized designs.

Design Solution	Aluminum	Copper	Silver
h_o/H	0.82	0.63	0.69
h_i/h_o	0.90	0.86	0.90
w_o/W	0.90	0.75	0.90
l_{therm} [mm]	0.18	0.20	0.16
h_o [mm]	3.69	2.84	3.11
w_o [mm]	17.1	14.3	17.1
P_{cyc}/m_{tot} [W/kg]	14.9E-3	5.30E-3	7.83E-3
$\overline{\sigma}_{SMA}^{max}$ [MPa]	282	296	299

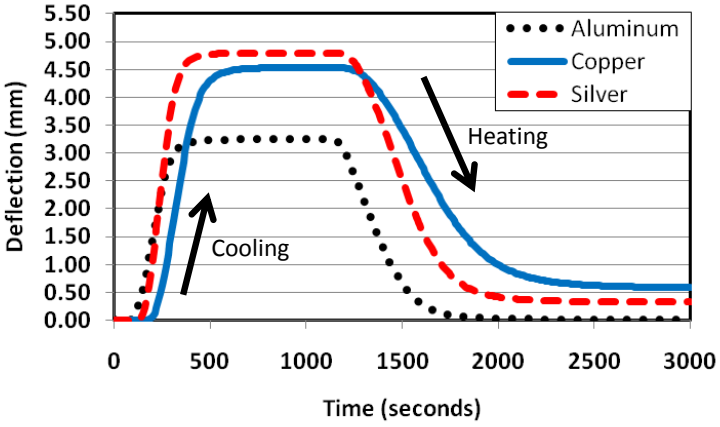

(a) Deflection of the flexure tip over time

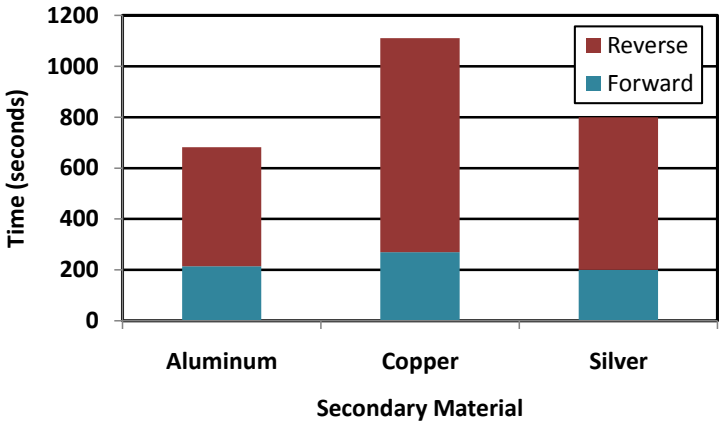

(b) Full transformation cycle time

Fig. 23. Transformation deflections and times for optimized full model designs.

CHAPTER IV

DESIGN OPTIMIZATION OF A MORPHING AEROSTRUCTURE WITH INTEGRATED SMA FLEXURES

Having demonstrated a method for optimizing SMA actuator components in Chapter III, we now demonstrate the capability of the expanded modeling framework for handling more complicated *assembly*-level design and analysis. This study is motivated by an interest in developing more cost- and time-efficient methods for designing entire morphing aerostructure assemblies alternative to the legacy design-build-test method. Historically, this legacy method of smart structures design has involved several iterations of altering, fabricating, and testing expensive physical prototypes, largely relying on trial and error experimentation to arrive at an "optimized" design solution. While experimental tests are still important to validate baseline computational models and to certify final designs, it will be shown here that it is no longer necessary to use experimental tests alone to explore an entire design space.

This work demonstrates the use of the tools introduced in Chapter II to solve an example engineering design problem in an efficient manner. However, the thermomechanical coupling effects that were considered in the previous study are neglected since we are no longer interested in transient solutions. Therefore, we now focus on designing to the static behavior of a morphing aerostructure with SMA flexures. This study involves determining the optimized configuration of the assembly by altering design inputs representing the placement of active components and geometry of support material to minimize a specified cost function related to structural deflec-

tion. The relevant components of the expanded modeling framework are illustrated in Fig. 24.

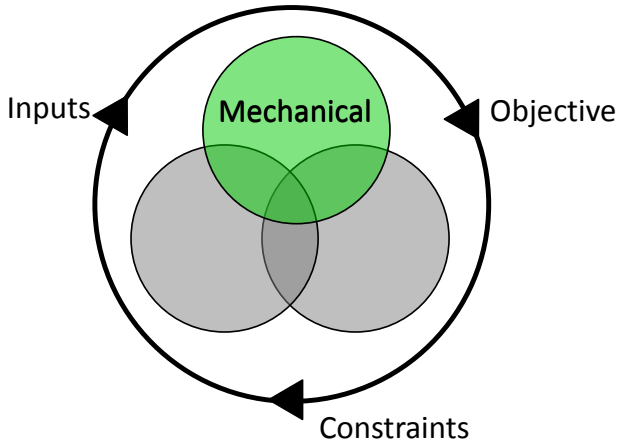

Fig. 24. Pertinent aspects of the expanded modeling framework for assembly-level morphing structure design.

The first section of this chapter reviews the example aerostructure, and its associated FEA model, and outlines the tools used in this study. Two cost functions, formulated as different mathematical evaluations of the optimization statement, are described and the optimization algorithm is summarized. This includes a specially tailored version of the design optimization algorithm outlined in Chapter II, Section C. The second section presents tabular and illustrative results for the optimized design variables and the resultant cost evaluations for each cost function.

A. Engineering Model and Analysis Tools

As in Chapter III, the Boeing VGC illustrated in Fig. 25 is the motivating morphing structure design here. Recall from Chapter I that the VGC consists of three SMA flexures installed in a prestrained martensitic configuration onto a carbon fiber

composite panel. This panel contains two thickened regions of stiffening tape used to provide additional structural support and to prevent panel buckling during flexure actuation. Here, the interaction between the actuators and carbon fiber panel is considered, and therefore the VGC assembly is modeled in its entirety.

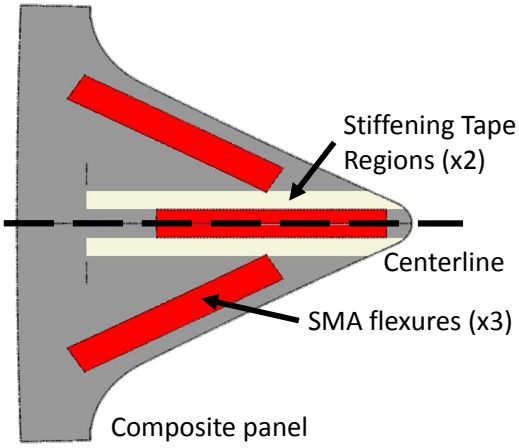

Fig. 25. Illustration of the stiffening tape regions and SMA flexure configuration on the flight-tested VGC.

The VGC is an example of an application developed using the legacy design-build-test method. A more efficient design methodology for any such structure is the primary motivation for this focused study. During the initial development phase of the VGC, several prototypes were designed, built, and tested with various flexure geometries and configurations [21]. The process iterated for three-and-a-half years until the centerline deflection profile of the chevron nearly matched an "ideal" profile chosen by aerodynamicists and acoustics engineers (see Fig. 26) to provide the required reduction in noise levels. This trial and error method of design is inherently expensive, time-consuming, and has the potential to bypass better performing design configurations.

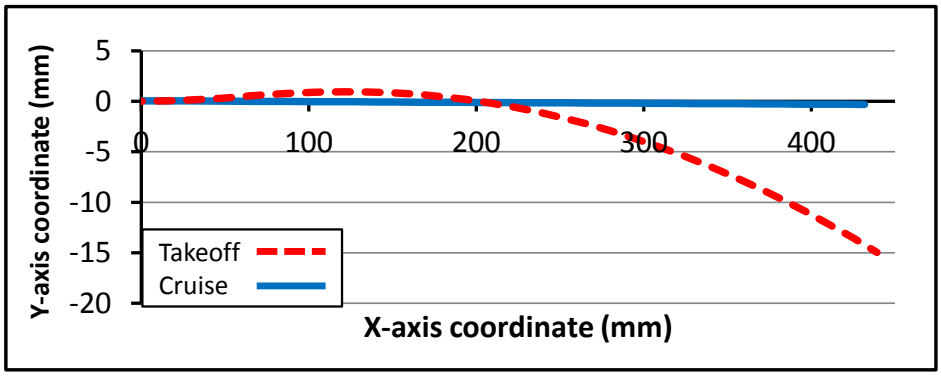

Fig. 26. Plot of the ideal VGC centerline deflection profile for takeoff and cruise conditions.

The purpose of this study is to show that a better design solution for the VGC can be found in a more efficient manner, given available constitutive modeling tools and optimization algorithms. To accomplish this, various design configurations of the VGC are analyzed in which the position of SMA flexures and the thickness of the stiffening tape are optimized such that the surface deflection of the composite panel matches with the aeroacoustically "ideal" profiles seen in Fig. 26, subject to best-practice constraints regarding SMA and composite loads. This is posed in the form of the following problem statement:

Determine an optimized design of the Boeing VGC that best achieves desired deflection profiles at takeoff and cruise conditions by altering only flexure placement/orientation and stiffening tape thickness without overstraining the composite panel or overstressing the SMA components.

1. Specific Analysis Tools

The same combination of numerical analysis and simulation process management tools used in the previous study from Chapter III are used here:

1. the Abaqus FEA suite (see Chapter II, Section A.1),

2. the SMA constitutive model implemented as an Abaqus/Standard UMAT (see Chapter II, Section A.2),

3. the Design Explorer design optimization tool available in Model Center (see Chapter II, Section C).

Note that, since the static behavior of the structure is considered here, we neglect the latent heat terms in the SMA constitutive model and specify the use of `STATIC` analysis steps in Abaqus.

2. Model Geometry and Materials

The 3-D FEA model of the VGC is similar to that found in the works of Hartl et al. [21], [22]. A composite panel FEA mesh, consisting of 3-D second-order triangular shell elements (`STRI65`), is imported into the model assembly. This mesh is graphically rendered as a single layer and is shown in Fig. 27. The computational model specifies 15 composite layers of alternating 90° carbon fiber weaves, each 0.21 mm thick. Two thickened stiffening tape regions are also included, as shown in Fig. 27. Symmetry is assumed along the centerline of the composite panel, and subsequently only half of the assembly is modeled and symmetric boundary conditions are imposed. Each SMA flexure is modeled using the nominal physical dimensions representative of flexures manufactured by Boeing (124 mm x 38 mm with a thickness of 4.4 mm at the center and tapering to 1.7 mm at the tip). The resulting shape, seen in Fig. 27, is an arcing beam that is meshed using second-order reduced integration 3-D stress elements (`C3D20R`), with one element through the thickness[1]. These flexures consist

[1]No discernible change in the structural response was detected during transformation when the number of thickness elements was increased.

of $Ni_{60}Ti_{40}$ SMA, whose material properties are given in Chapter III, Table II.

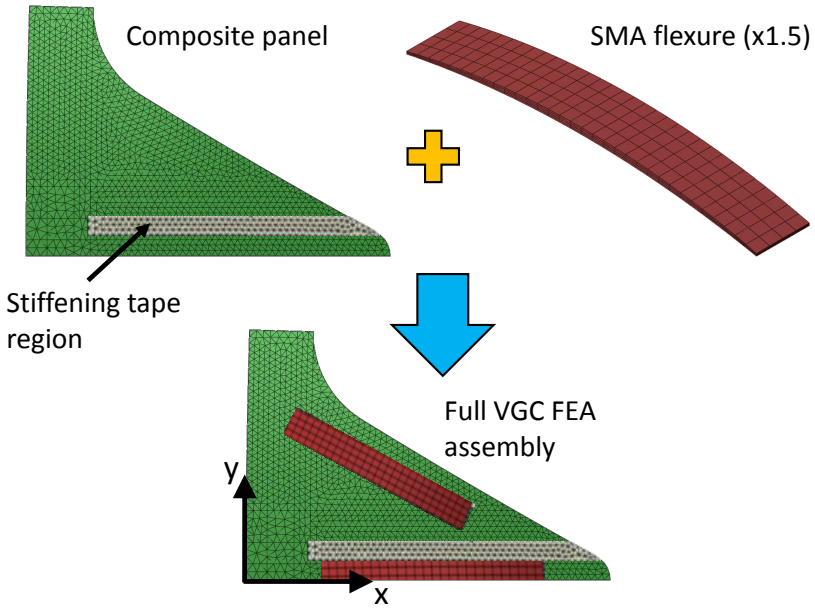

Fig. 27. 3-D FEA models of the VGC composite panel (left), SMA flexure (right), and assembled structure.

3. Initial and Boundary Conditions

To establish the correct assembled stress conditions in the flexures and panel, the full finite element analysis must consider the process of installing the flexures onto the panel as separate steps before initiating SMA actuation. The process is generalized for use with any design configuration of the VGC, and is capable of autonomously assembling the model for any feasible placement of the flexures. Installation of the flexures is reflected in the first three of six total analysis steps. Initially, the composite panel is kinematically constrained near its base with zero-displacement boundary conditions applied over an engine attachment region (shown in Fig. 28). Both *full* and *half* (symmetric) flexures are placed well above the panel surface at 107 °C ($A_f +$

37 °C). The center nodes of the underside of each flexure are kinematically tied to vertically-oriented `AXIAL` connector elements, which terminate at reference points located well beneath the panel, as seen in Fig. 28. The analysis proceeds with the first three steps, which are outlined as follows:

1. Controlled downward displacement of both flexures, specified at four "mounting" points, moves the flexure tip nodes close to the substrate. Contact controls disallowing surface penetration are specified between flexure tip nodes and the substrate and allow for sliding. The flexures and substrate come into contact. The flexures and substrate come into contact.

2. The axial connector elements contract along their vertical axis, drawing the reference points closer to the center flexure nodes. The flexure is thus "clamped" to the panel surface, introducing additional stress into both the flexures and the panel.

3. To simulate bonding of the center of the flexure with the substrate [79], contact controls disallowing post-contact separation are activated between the underside of the flexure, at its center, and the top surface of the panel. Simultaneously, the displacement boundary conditions on the connector elements are released.

Following the analysis steps related to multicomponent assembly, those pertaining to the transformation (and therefore *operation*) of the SMA flexures begin. These transformation steps are:

4. Cool flexures to full martensite.

5. Heat flexures to 58 °C ($A_f - 12\,°C$).

6. Cool flexures to 20 °C ($M_f + 51\,°C$).

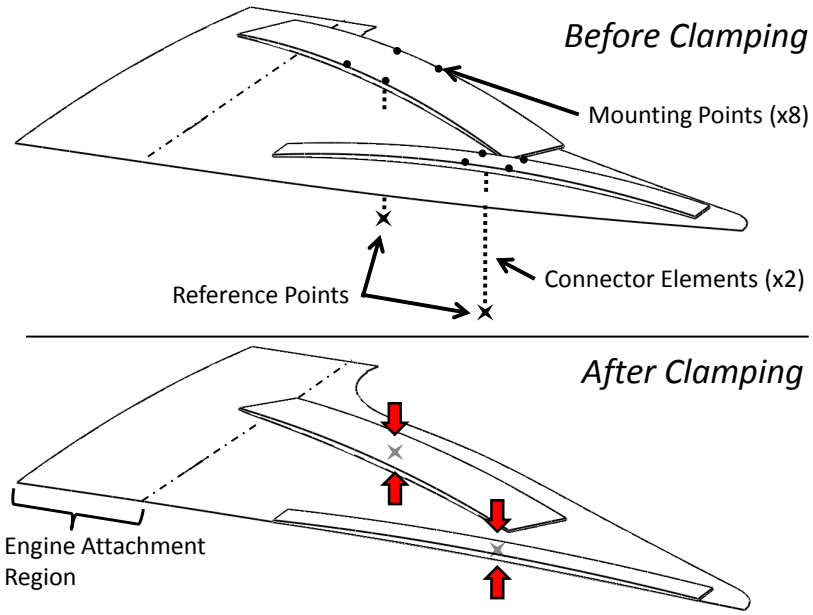

Fig. 28. Graphical representation of the SMA flexure installation.

Due to the thermal conditions specified in steps (v) and (vi), the material points composing the flexures traverse a minor loop within the full SMA transformation hysteresis. This additional design choice provides a small additional regime of motion control outside the normal dynamic range of the VGC.

4. Optimization Statement

To frame the problem statement in a design optimization setting, the cost function, design variables, and constraints on chosen output parameters must be carefully considered. This study focuses on obtaining optimized design solutions for only the takeoff flight condition, when the SMA is thermally activated and the chevron is deflected into the flow. A non-dimensional cost function C quantifies the absolute deviation, or *error* $|\varepsilon(x)|$, of the FEA-predicted local panel deflections from the ideal deflection profile for the takeoff condition. The ideal panel deflection along the axis

of symmetry (the centerline) can be seen in the graph in Fig. 26.

Two design optimization cases are considered in this study. Both formulations integrate the absolute error $|\varepsilon(x)|$ along the centerline while applying a weighting function $f(x)$ to more heavily penalize error near the tip of the panel, a region that is assumed to be particularly important in generating the desired aeroacoustic effect. Here, the weighting function is taken to be

$$f(x) = 9\frac{x}{L}, \tag{4.1}$$

where x is the distance from the origin to a point on the centerline (see Fig 27) and L is the distance from the origin to the tip of the panel. The manner in which this weighting function is implemented then varies between the two cost functions. In the first case, the cost formulation C_1 preserves the linear nature of $f(x)$ and is mathematically represented as:

$$C_1 = \frac{1}{h}\int_0^L |\varepsilon(x)|\,[1 + f(x)]\,\mathrm{d}x, \tag{4.2}$$

where h is the average distance between FEA nodes along the centerline. This particular formulation of the cost function results in a linear cost weight that increases 10 times from the origin towards the tip node.

In the second case, the cost formulation C_2 greatly increases the penalty for errors near the tip by considering an *exponential* implementation of $f(x)$:

$$C_2 = \frac{1}{h}\int_0^L |\varepsilon(x)|\,[1 + Ae^{kf(x)}]\,\mathrm{d}x, \tag{4.3}$$

where $A = 10^{-23}$ and $k = 6.27$ in this case study. The resulting cost function C_2 is more heavily influenced by tip node error than C_1.

Cost functions C_1 and C_2 are discretized for application in the FEA model. The

panel described in Section 2 is meshed with 115 nodes along the centerline. Assuming equal nodal spacing along the centerline ($\Delta x_i = h$), the discretized forms of (4.2) and (4.3) become summations over the error of each individual centerline node, given as:

$$C_1 \cong \sum_{i=1}^{115} |\varepsilon_i| \left(1 + 9\frac{x_i}{L}\right), \tag{4.4}$$

$$C_2 \cong \sum_{i=1}^{115} |\varepsilon_i| \left(1 + Ae^{(k\frac{9x_i}{L})}\right). \tag{4.5}$$

Minimization of the cost function C is accomplished by varying the location and orientation of the SMA flexures and thickness of the stiffening tape regions[2] as input design variables, which are illustrated in Fig. 29. Assuming symmetry along the centerline of the VGC, we consider a coordinate system whose origin is located on the centerline and at the base of the chevron, as shown in Fig. 29. We then consider the following design variables with respect this coordinate system:

- x_{half}: the x-coordinate, in millimeters, of the centroid of the half flexure,
- x_{full}: the x-coordinate, in millimeters, of the centroid of the full flexure,
- y_{full}: the y-coordinate, in millimeters, of the centroid of the full flexure,
- θ_{full}: the orientation of the full flexure, in degrees, about the centroid and with respect to the x-axis,
- t_{tape}: a multiplying factor of the thickness of the stiffening tape region from the flight-tested VGC configuration.

[2]Only the thickness of the stiffening tape is considered variable as opposed to the entire substrate, since the nominal substrate layup is taken to be identical to the fan cowl to which it is attached.

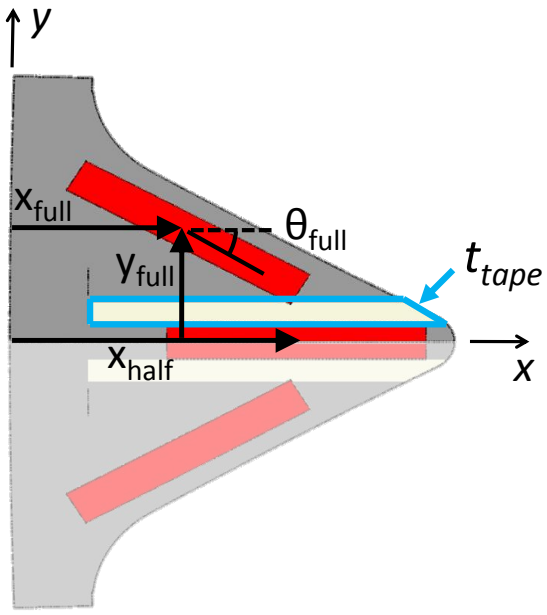

Fig. 29. Graphic representation of the design variables considered in this design study.

In addition, constraints are established to limit damage to the SMA flexures and composite panel. These constraints bound the maximum measured SMA component Mises stress ($\overline{\sigma}^{max}_{SMA}$) and maximum measured in-plane principle strain of the composite panel ($\varepsilon^{max}_{panel}$) from above by the critical values $\overline{\sigma}^{crit}_{SMA}$ and $\varepsilon^{crit}_{panel}$, respectively. Throughout the remainder of this work, these critical limits are taken to be:

- $\overline{\sigma}^{crit}_{SMA} = 276$ MPa (40 ksi),
- $\varepsilon^{crit}_{panel} = 0.5\%$.

The engineering problem statement is then summarized as a constrained optimization problem in Table VIII. Note that limits have been placed on the input design variables to confine our search to a reasonable area of the design space. However it is shown in the following subsection that these limits are not sufficient to prevent the generation of infeasible designs and that further measures are required to properly

search the design space.

Table VIII. The design optimization summary for this morphing aerostructure study.

Objective:	
Minimize	C_1, C_2
Input:	
	$95 \leq (x_{half}) \leq 275$
	$95 \leq (x_{full}) \leq 275$
by varying	$95 \leq (y_{full}) \leq 275$
	$-30 \leq (\theta_{full}) \leq 30$
	$0.01 \leq (t_{tape}) \leq 3.0$
Constraints:	
subject to	$\overline{\sigma}_{SMA}^{max} \leq \overline{\sigma}_{SMA}^{crit}$
	$\varepsilon_{panel}^{max} \leq \varepsilon_{panel}^{crit}$

5. Optimization Algorithm

We begin describing the optimization process by considering the limits that have been placed on the inputs. The chosen ModelCenter optimization tool explores a given design space that is defined only by upper and lower limits on input design variables. In this specific case, the design space shown in Fig. 30 is then bounded by a simple two-dimensional box around the composite panel that limits the design variables governing the location of each SMA component (x_{full}, y_{full}, x_{half}). Considering that a great deal of empty space is enclosed within this bounded area, and further considering that many angles of θ_{full} are investigated, more stringent and more complicated constraints must be considered. Since the average run time for each FE

analysis is 20 minutes, and since many runs are necessary in order to converge to an optimal solution, a significant amount of time could be wasted if non-physical configurations resulting from infeasible design vectors were submitted for analysis. However, a mathematical formulation of constraints is not possible for an arbitrarily shaped structure such as the one considered in this study. Therefore, we allow the optimization algorithm to choose design vectors from a simply bounded set, but then prevent non-physical designs from being submitted for analysis. To accomplish this, a geometry checking subroutine is implemented to predict if a given design vector will result in an infeasible model. An infeasible design vector is one in which:

1. any part of a flexure is placed outside of the bounding area (the black box in Fig. 30),
2. any part of a flexure is placed in the empty space within the bounding area,
3. flexures interfere with each other,
4. any of the four mounting points of each flexure are placed within the engine attachment region.

This algorithm is executed prior to each analysis and prevents an analysis from running if the suggested design configuration cannot satisfy the three requirements listed above. The feasbility check executes within seconds, saves hours of analysis time over the course of a full optimization, and can be useful for appropriately handling design vectors over any irregular domain that cannot be easily bounded with simple geometric equations. The feasibility checking algorithm is implemented as a subroutine within the main Python script and represents the chevron panel and flexures as shapes in a 2-D Cartesian coordinate system. The chevron component is

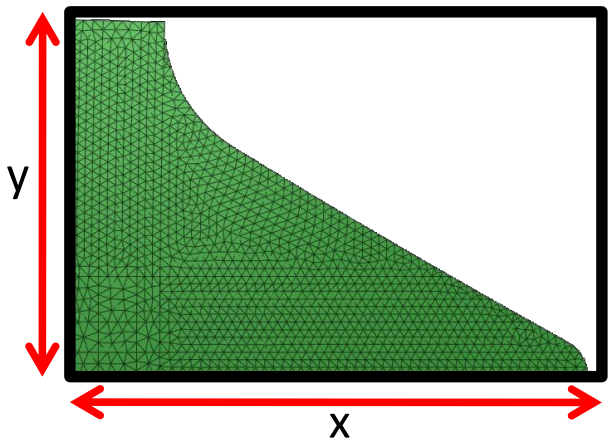

Fig. 30. Design space for the flexure location design variables.

approximated using ten connected points, and the flexures are expressed as rectangles with four mounting points. A graphic of the chevron and flexures in this 2-D approximate representation can be seen in Fig. 31. Note that the mounting points are located as black circles on the full-flexure.

The subroutine starts by checking the first of the four feasibility requirements and so determines if any of the flexure corners lie outside of the bounding area shown Fig. 30. If this is true, then the algorithm exits and prevents the analysis from running the suggested design configuration. If this is false, then a combination of a sorting algorithm and a linear regression analysis is employed to check each of the subsequent three feasibility conditions: (ii), (iii), and (iv). Examples of proposed flexure placements checked by the algorithm are shown in Fig. 32.

In the event that the feasibility subroutine prevents a configuration from being analyzed, the ModelCenter-based optimizer tags the attempted design vector as a "failed" run and will attempt to continue searching the design space. However, simple gradient optimization algorithms are particularly sensitive to missing data resulting

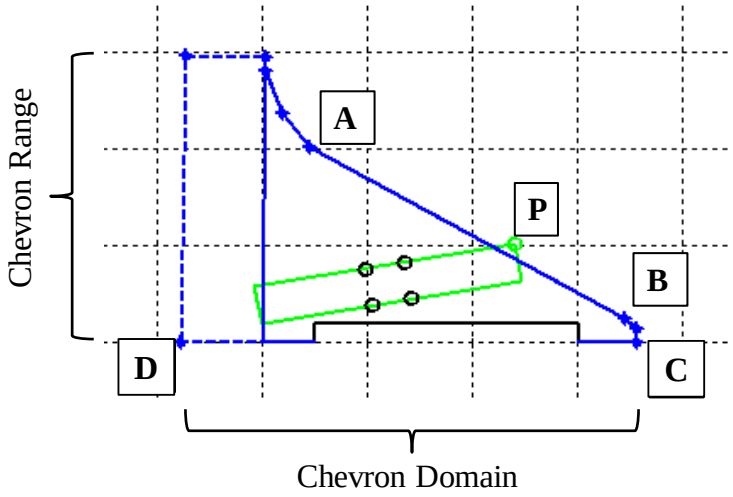

Fig. 31. Example of a proposed design configuration. Outlined are approximations of the chevron (blue), half-flexure (black), and full-flexure (green).

from failed engineering analysis and are less likely to converge upon optimized design solutions when this occurs. Given the nature of the feasibility check, it is clear that a robust optimization algorithm capable of handling a number of unsuccessful design attempts is necessary. For this reason, we choose to use the Design Explorer tool suite, which was developed with these needs in mind[3].

The flow of data for a general iterative optimization scheme was described in Chapter II, Section C. However, since a feasibility analysis is required in this study, a specially tailored procedure considering the eventuality of passed/failed design vectors is necessary. This new scheme is illustrated in Fig. 33. Design Explorer first chooses a design vector and passes it to the geometry checking algorithm. This algorithm checks for model feasibility and, based on the requirements stated earlier, either

[3]The model analyzed in this study is also suited for optimization using genetic algorithms. However, this algorithm was overlooked due to the high number of runs needed to complete an evolutionary optimization.

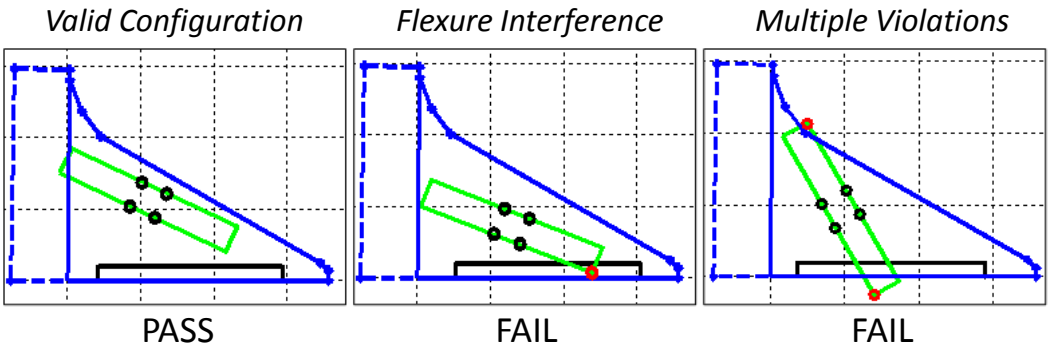

Fig. 32. Examples of possible design configurations checked by the feasibility algorithm.

prevents the preprocessing of the model or allows the analysis to continue. Each successful FE analysis outputs the scalar value calculated from the cost function, the maximum in-plane principal strain anywhere in the panel, and the maximum Mises stress anywhere in the SMA flexures encountered during transformation through the minor loop (the final two steps of the analysis). These values are then passed back into the Design Explorer simulation process manager and the algorithm chooses the next design vector. If an optimized design solution is found, the scheme terminates and Design Explorer reports the optimized design variables and associated output values.

B. Analysis Procedures and Results

Applying the procedures outlined in Section 5 to the two cost functions C_1 and C_2, two optimized designs are found. The optimized design solution *Design 1* will be used to denote the configuration associated with the design vector that was originally found to minimize cost function C_1, and likewise for *Design 2* with C_2. ModelCenter converged upon these design solutions after 189 successful function evaluations for

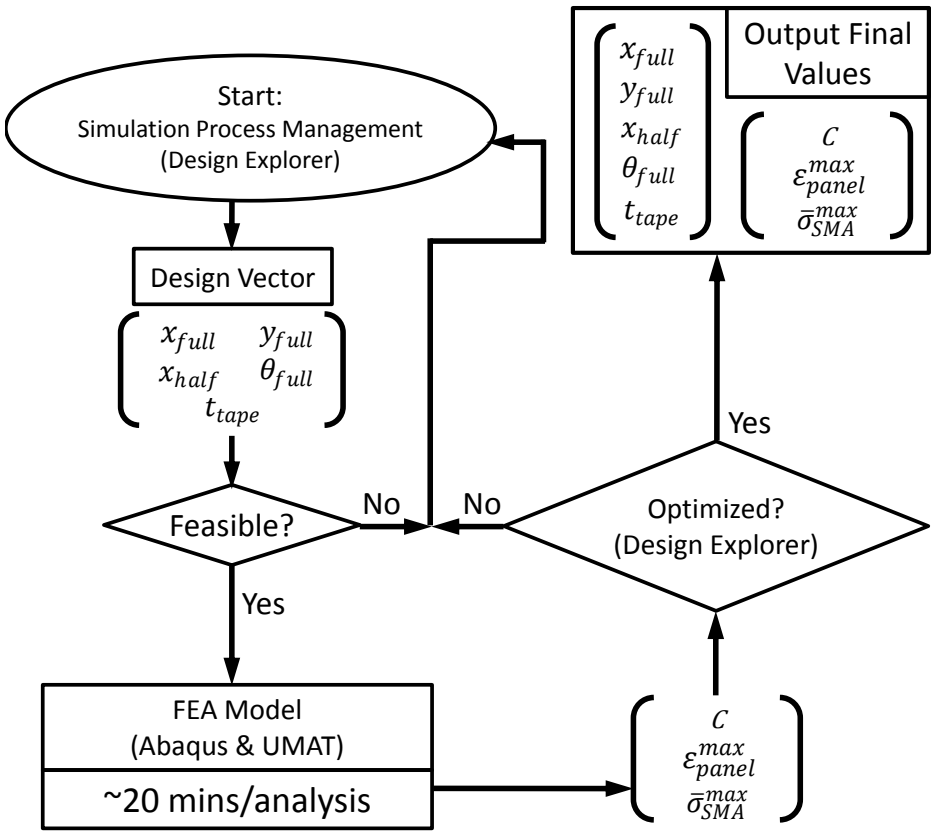

Fig. 33. Flow chart describing the iterative analysis process for VGC design optimization.

C_1 and 236 evaluations for C_2, requiring approximately 60-80 total hours of CPU time for each cost function. To compare the performance of *Design 1* and *Design 2* with the Boeing prototype [80], the flexure configuration and tape thickness of the nominal flight test design are used to generate and analyze a representative FEA model. The configurations for all three designs are shown in Fig. 34 and the input design variable values, resultant maximum SMA stresses, and maximum composite strains are numerically summarized in Table IX.

From Table IX, it can be seen that the optimized configurations do not seem to be restricted by the constraints on $\overline{\sigma}_{SMA}^{crit}$ or $\varepsilon_{panel}^{crit}$ specified in Section 4 (recall

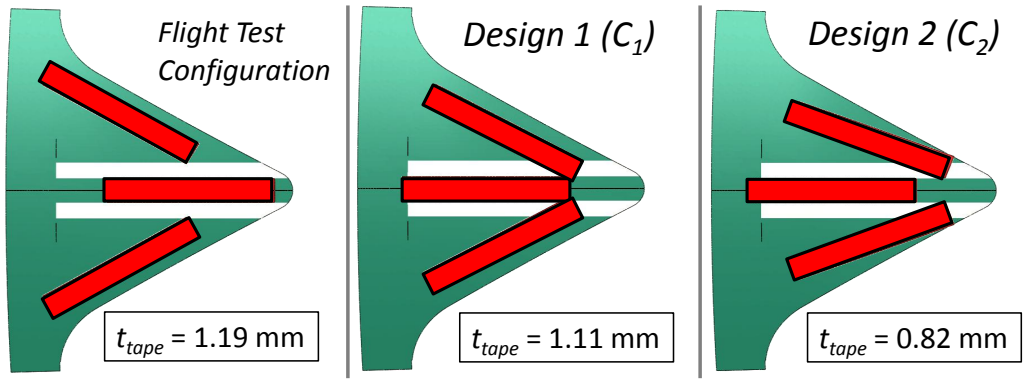

Fig. 34. Illustrations of the nominal optimized VGC configurations.

that $\overline{\sigma}_{SMA}^{crit} = 276$ MPa and $\varepsilon_{panel}^{crit} = 0.5\%$). It is also interesting to note that the orientation of the *full* flexures ($\sim 30°$) between the original flight test configuration and *Design 1* are fairly consistent and generally conform to the triangular shape of the substrate, as seen in Fig. 34. In addition, the center flexures (i.e. those that lie on the centerline) in both optimized configurations are placed further from the tip of the panel than was the case for the original flight test configuration.

Figure 35 provides contour plots of the analytical surface deflection error (deviation from the ideal surface) for each of the designs. Configurations *Design 1* and *Design 2* show a considerable improvement in the centerline region over the FEA representation of the Boeing flight tested prototype, albeit at the expense of an increase in error in regions away from the centerline. The predicted centerline deflection profiles for each of the configurations are plotted against the ideal profiles in Fig. 36. It can be seen that the predicted takeoff profile in *Design 2* more closely matches the ideal takeoff profile than that of *Design 1*. This result indicates that the Design Explorer algorithm, in minimizing C_1, did not effectively explore the design space in

Table IX. Optimal design values and resultant stresses and strains for three VGC configurations.

Analysis Output	Flight Tested	Design 1	Design 2
x_{half} [mm]	280	195	187
x_{full} [mm]	174	220	245
y_{full} [mm]	123	90	82
θ_{full} [deg]	-30.0	-28.9	-20.7
t_{tape} [mm]	1.19	1.11	0.82
$\overline{\sigma}^{max}_{SMA}$ [MPa]	159.4	147.4	145.7
$\varepsilon^{max}_{panel}$ [%]	0.26	0.30	0.32

the vicinity of *Design 2*, and instead settled on a solution with a higher cost[4].

[4]This is likely due to the selection of default search options prior to starting the algorithm. This resulted in an initial sampling of the design space that was unrefined and a local minima was accepted as the optimized design.

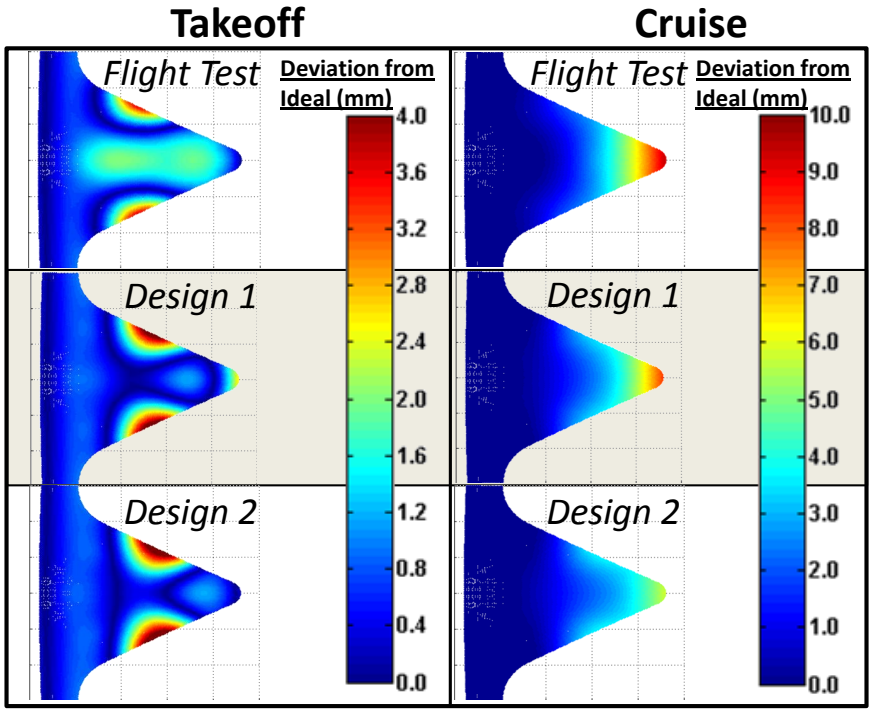

Fig. 35. Contour plots of analytical surface deviations from the ideal surface.

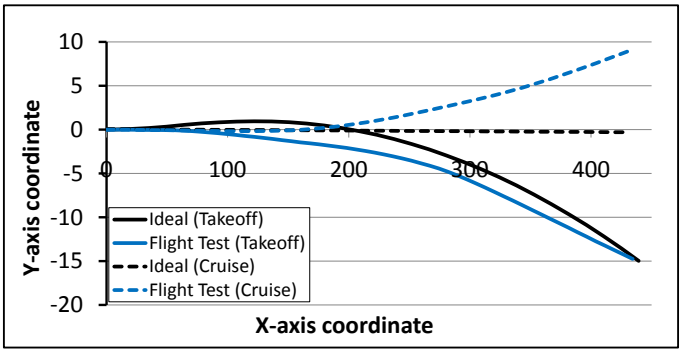

(a) Boeing flight tested configuration.

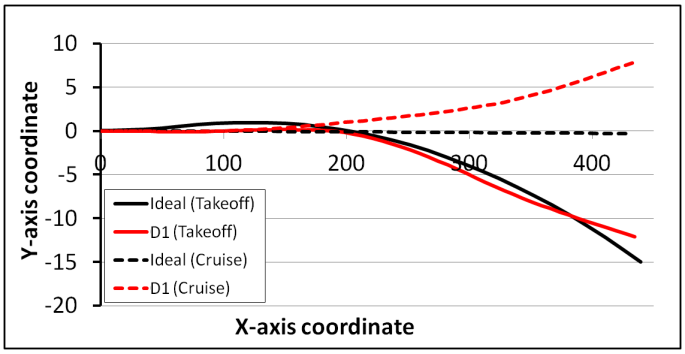

(b) *Design 1* optimized configuration.

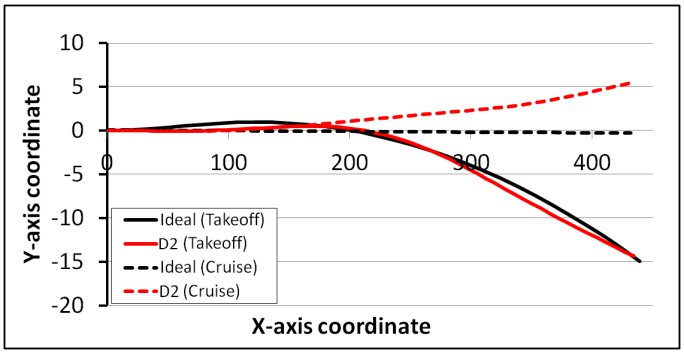

(c) *Design 2* optimized configuration.

Fig. 36. Centerline deflection profiles for various VGC configurations.

CHAPTER V

FLUID-STRUCTURE INTERACTION OF AN SMA ACTUATED MORPHING AEROSTRUCTURE*

As explained in Chapter I, SMAs have a high actuation energy density that makes them an ideal replacement for conventional actuation mechanisms in morphing aerostructures. However, SMA components are often exposed to the same highly variable environments experienced by the aeroelastic assemblies into which they are incorporated. This is motivating design engineers to consider modeling fluid-structure interaction (FSI) for prescribing dynamic, solution-dependent boundary conditions. The following *system*-focused study demonstrates the FSI capabilities of the expanded modeling framework by analyzing a particular morphing aerostructure in a representative flow field. The effect of the considered morphing structure on the pressure and velocity field of a high-speed fluid flow, and conversely the effect of the pressure distribution of the fluid on the deflection profile, is of particular interest. These areas of interest are best represented as highlighted, or "active", fields of the expanded modeling framework illustrated in Fig. 37.

The first section reviews the morphing structure design, outlines which of the tools introduced in Chapter II are invoked to analyze this engineering problem, and describes the specific details of the models. This includes discussion regarding fluid and solid domain geometries, material properties, and initial/boundary conditions. The second section presents numerical analysis results that are validated against experimental data from benchtop and representative flow tests.

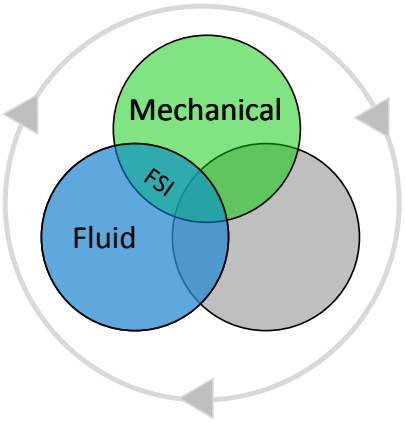

Fig. 37. Pertinent aspects of the expanded modeling framework for fluid-structure interaction.

A. Engineering Model and Analysis Tools

The morphing aerostructure modeled in this study is the SMA hybrid composite (SMAHC) chevron [12], a prototype developed at the NASA Langley Research Center (LaRC) in the early 2000s[1]. Recall from Chapter I that the SMAHC chevron is a composite panel with embedded SMA ribbons installed in a pre-strained martensitic configuration below the neutral axis, and that heating of the ribbons induces contraction of the SMA resulting in panel deflection. A 1:9 scaled physical prototype of this assembly, shown in Fig. 38, has been built and tested in representative flow conditions at the NASA LaRC Small Anechoic Jet Facility (SAJF) [12]. The focus of the tests was to determine the thermal distribution and actuated deflection profile of the chevron as a response to closed- and open-loop controllers, while exposed to subsonic flows. These tests are the motivation for this current work, where we attempt to

[1]Although this method is demonstrated on a specific application here, it is intended for use with any morphing aerostructure analysis.

replicate these test conditions in a computational model. This study will only focus on the resulting deflection profile of the chevron due to the mechanical effects of the flow field, given a specified thermal distribution and without regard for the controls system. The following subsections describe in greater detail the scheme used to generate the FSI models, as well as the procedure for importing, creating, or specifying the solid and fluid geometries, material properties, and boundary conditions.

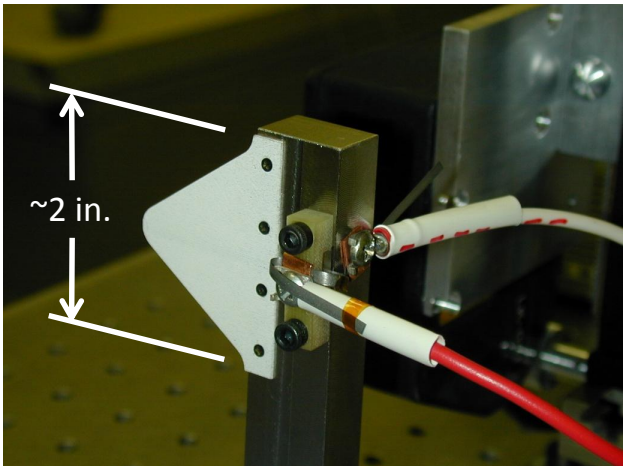

Fig. 38. Scaled prototype of the SMAHC chevron.

1. Specific Analysis Tools

Note from the Venn diagram in Fig. 37 that the areas of interest in this study involve predicting the response of the SMA components and surrounding composite structure, while accounting for a dynamic fluid environment. This FSI problem requires the use of cosimulation methods, which have been outlined in Chapter II, Section B.2. Through the Abaqus cosimulation engine (CSE), we link the following tools:

1. the standard, thermomechanically *uncoupled*, formulation of the constitutive model (UMAT) implemented in the Abaqus FEA framework (see Chapter II,

Sections A.1 and A.2),

2. the CFD incompressible flow module native to Abaqus (see Chapter II, Section B.1).

For this study, data exchange through CSE is chosen to occur every 10^{-4} seconds, over a total time step spanning 0.15 seconds, and follows the Gauss-Seidel time-marching algorithm [31] shown in Fig. 11.

2. Model Geometries and Materials

The solid and fluid models analyzed in this study contain geometric representations of the SMAHC chevron and the environment surrounding the nozzle test setup, respectively. The 3-D FEA solid model geometry is identical to that found in the works of Turner et al. [12]. A composite panel FEA mesh consisting of quadrilateral and triangular shell elements (`S4` and `S3` respectively) is imported into the solid model assembly, seen in Fig. 39. The mesh is graphically rendered as a single layer, however the model specifies section definitions for five plies of 0.127 mm-thick glass-epoxy oriented with respect to 0.152 mm-thick SMA ribbons in the following order: -45°, +45°, 90°, SMA, +45°, SMA, -45°. [12]. In order to reduce computational expense, symmetry along the centerline is assumed and thus only half of the structure is modeled. Note that this assumption is only valid because the bend-twist coupling effect in this asymmetric ply lay-up is considered weak and can therefore be neglected.

The composite material properties used in this study are borrowed from the works of Turner et al. [12], where the special orthotropic properties of the glass-epoxy plies have been defined. However, the established FEA framework [21], [22] in this study calls for a full, 3D SMA constitutive model [68] rather than the purely thermoelastic model proposed in those works. Therefore, a full set of SMA material properties

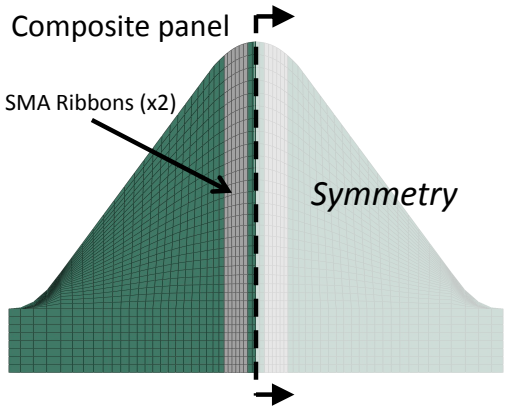

Fig. 39. 3-D FEA model of the SMAHC chevron.

specific to this model must be calibrated. These material properties are characterized using a combination of thermal actuation[2] and blocked force data [81]. In this case, an untrained specimen of $Ni_{55}Ti_{45}$ (wt.%) ribbon from NASA LaRC that is identical in dimensions and composition to the specimen used in the SMAHC chevron is characterized using a differential scanning calorimeter (DSC) and a material testing system (MTS).

The results from DSC analysis, plotted in Fig. 40, are used to provide approximate values for the zero-stress transformation temperatures (A_s, A_f, M_s, and M_f), which are used to program full-cycle isobaric thermal actuation tests[3]. Following DSC analysis, the full-cycle thermal actuation tests are performed on the specimen at three applied stress levels: 50 MPa, 100 MPa, and 200 MPa. The stress-temperature phase diagram shown in Fig. 41 is plotted from the resulting thermal actuation data, giving

[2]Thermal actuation data obtained in a laboratory setting using methods outlined in the works of Lagoudas et al. [46].

[3]Tests were conducted using an MTS® Insight 30 kN electromechanical, screw-driven test frame and a Thermcraft® thermal chamber. Chamber temperature was controlled via convective heating and liquid nitrogen cooling.

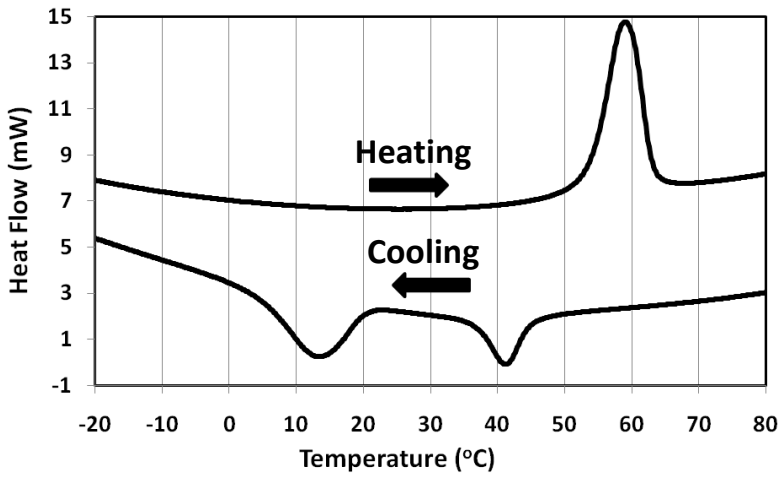

Fig. 40. Heat flow as a function of DSC chamber temperature.

a more accurate reassessment of the zero-stress transformation temperatures. Isothermal pseudoelastic tests are then conducted at chamber temperatures well above A_f and well below M_f to determine the elastic moduli for both the austenitic and martensitic states (E_A and E_M) respectively.

It is important to note that the coefficients in the current maximum transformation strain function $H^{cur}(\overline{\sigma})$ and the stress influence coefficient of austenite C_A (i.e. the slope of the reverse transformation surface) are not calibrated from the thermal actuation tests, as is conventional [21]. The reason for this can be seen in Fig. 42, where the specimen ceases providing recovery stress at higher temperatures under blocked load. This is interpreted as plastic yielding of the specimen during transformation, a phenomena not captured here by thermal actuation testing. This behavior indicates that the FEA model should account for plasticity in order to provide an accurate prediction of the behavior of the SMA ribbon when it is embedded in the glass-epoxy plies of the SMAHC chevron. A particular version of the constitutive

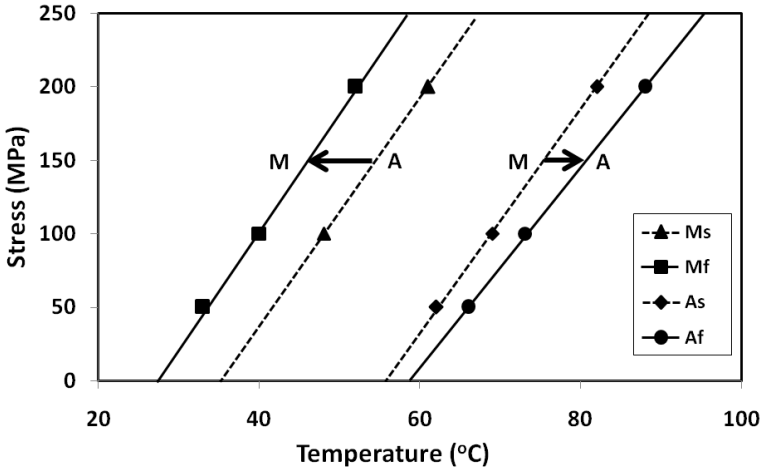

Fig. 41. Phase diagram obtained from thermal actuation testing.

model has been tailored for the purpose of accounting for the generation and evolution of irrecoverable plastic strains [64], however its use would require significant characterization efforts beyond the scope of this work. For the present, this yielding phenomena has instead been approximated by directly calibrating $H^{cur}(\overline{\sigma})$ and C_A to closely match the aforementioned blocked force test data [81], seen in Fig. 42. From Fig. 42, it is determined that the model prediction and experimental data are in good agreement at lower temperatures in the range $30 - 90°$C. However, error between the two curves begins to develop at higher temperatures around $\sim 90°$C, peaking at $\sim 110°$C.

The finalized set of calibrated SMA material properties that are used for the remainder of the study are presented in Table X.

The fluid model consists of a 3-D rectangular geometry that approximates the volume of affected air around the nozzle test setup, which is described in the works of Turner et al. [12]. The volume, shown in Fig. 43(a), is modeled in symmetry and

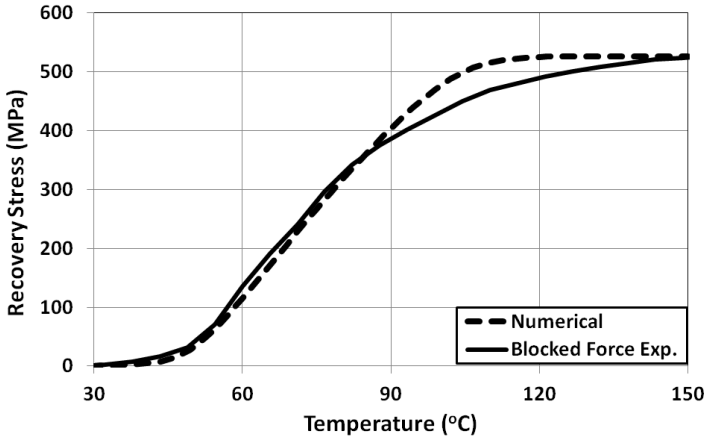

Fig. 42. Comparing the fully calibrated constitutive model with blocked force data [81].

is partitioned at one inlet wall to represent the nozzle flow. This partitioned area, shown in Fig. 43(b), is used later as the fluid inlet boundary condition (see Section 3). The upper and lower surfaces of the chevron, illustrated in Fig. 43(c), are specified as a collection of nodes colocated on a single plane directly above and perpendicular to the inlet area. This represents the SMAHC chevron fixed onto the nozzle exit. The resulting domain is meshed using tetragonal linear fluid elements (`FC3D4`) and without consideration of the boundary layer. It is assumed that the boundary layer can be neglected here since the inertial effects of the air flow are expected to greatly exceed viscous effects encountered in the analysis.

The relevant properties of air, density ρ and dynamic viscosity μ, corresponding to standard temperature and pressure (STP) are assumed for the fluid model material definitions [77]. These are summarized in Table XI. Note that density is considered constant throughout the analysis, as the current fluid model is not yet capable of analyzing compressible flows.

Table X. Material properties for the $Ni_{55}Ti_{45}$ (wt.%) shape memory alloy.

Property	Value	Property	Value
ρ [kg/m^3]*	5720	M_s [°C]	47
E_A [GPa]	81	M_f [°C]	22
E_M [GPa]	51	A_s [°C]	27
C_A [MPa/°C]	12.0	A_f [°C]	82
C_M [MPa/°C]	12.0	$H^{cur}(\overline{\sigma})$	$= 0.0065\left[1 - \exp\left(-\frac{794\overline{\sigma}}{E_A}\right)\right]$
ν	0.33	$n_{1,2,3,4}$	0.2, 0.05, 0.1, 0.1

* Density ρ obtained from the works of Turner et al. [12]

3. Initial and Boundary Conditions

The CFD and FEA models in this study consider the proper application of mechanical and thermal boundary conditions to mimic the conditions under which the representative flow tests were conducted [12]. In the flow test, the chevron prototype was mounted on a nozzle and actuated such that the deflected panel was immersed in the flow. The Abaqus CFD/FEA cosimulation therefore consists of a single analysis

Table XI. Material properties for the representative air flow.

Property	Value
ρ [kg/m^3]	1.225
μ [kg/m-s]	1.983x10^{-5}

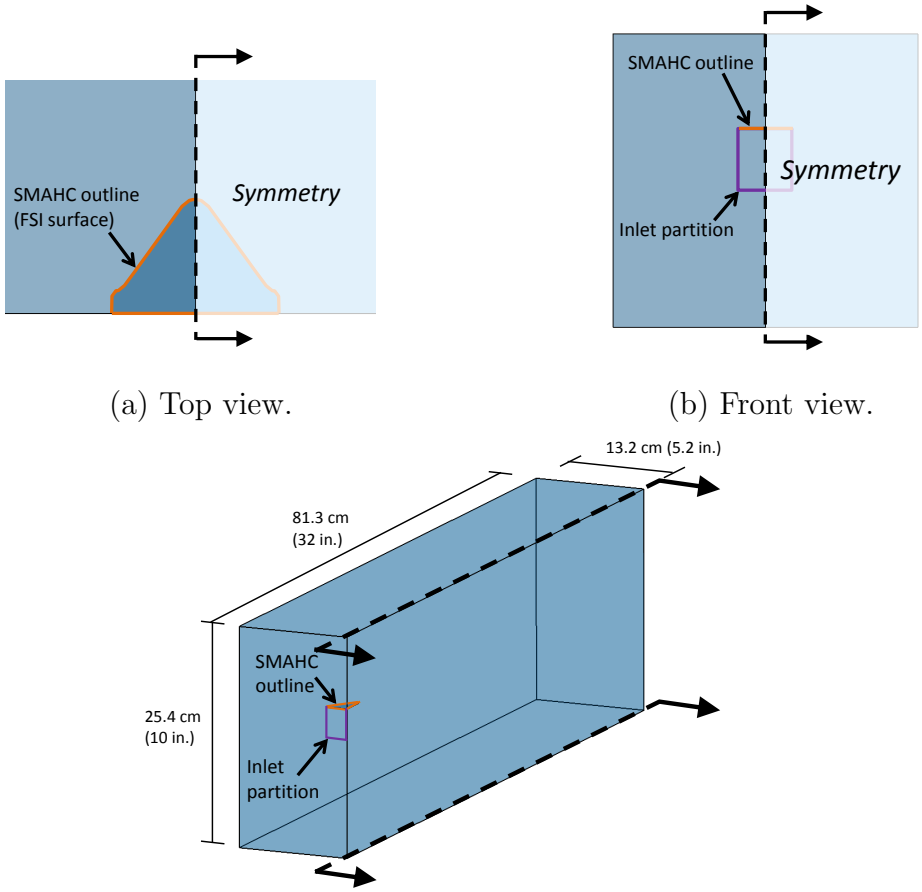

(a) Top view.

(b) Front view.

(c) Offset view.

Fig. 43. Views of the fluid model geometry.

step that spans 0.15 seconds, during which the air velocity at the inlet is steadily ramped up from zero to a specified magnitude while the chevron is simultaneously actuated from the martensitic "powered-off retracted" configuration to the austenitic "powered-on immersed" configuration[4].

The initial/boundary conditions applied to the solid FEA model are illustrated

[4]A more realistic actuation time history was attempted, however instabilities in the solution and a significant increase in the residual over successive time increments detracted from the reliability of the results. Future work will focus on resolving these issues.

in Fig. 44. For clarity, these are presented as three different sets of conditions. In Fig. 44(a), it is shown that nodes along the line of symmetry are constrained to only move along the plane of symmetry. The displacements and rotations of a select group of nodes at one end of the embedded SMA ribbon are fixed to represent the actuator clamp. Fig. 44(b) highlights a selected area of the laminate that is constrained from moving out-of-plane (the nozzle mounting region). Two nodes within this area are fixed to represent panel screws. In Fig. 44(c), an FSI boundary condition is applied to the upper and lower surfaces of the panel. A contour image of the thermal field of the SMAHC chevron, recorded by the IR camera from the test setup, is imported and mapped onto the mesh to specify a realistic temperature distribution in the model. At the beginning of the analysis step, the temperature of the panel is smoothly ramped from room temperature (293 K, uniformly distributed) to the equivalent temperature values of the mapped thermal field over the course of 0.08 seconds.

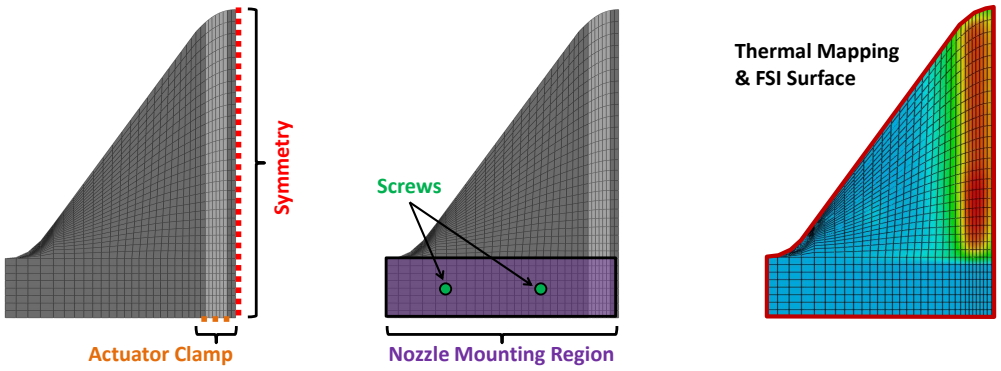

(a) Symmetry and actuator clamp. (b) Mounting region and screws. (c) Imported thermal map and FSI surface.

Fig. 44. Initial and boundary conditions for the solid FEA model.

The boundary conditions applied to the CFD model are illustrated in Fig. 45. As with any solid FEA model, the mechanical boundary conditions must also be specified

here in CFD to properly define the mesh morphing characteristics. The boundary conditions on the external surfaces of the domain are shown in Fig. 45(a). A uniform inlet velocity condition is specified in the partitioned region enforcing a smoothly increasing flow velocity over 0.1 seconds to a maximum specified limit, at which point the flow stabilizes for the remainder of the analysis step (an additional 0.05 seconds). A fluid wall condition is specified on the area surrounding the inlet, where flow velocity is zero. Freestream conditions, where relative gage pressure is zero, are specified at the top, bottom, side, and outlet of the domain. Lastly, a fluid symmetry condition is specified on the other side wall such that flow velocity is zero in the direction normal to the plane of symmetry. The displacements and rotations of all nodes on the freestream, fluid inlet, and wall regions are fixed, and so the mesh is constrained from morphing on these boundaries. However, the nodes in the region of symmetry are allowed to move in-plane in accordance with FSI mesh morphing. The region where the chevron is located within the fluid domain is highlighted in Fig. 45(b). The FSI surface condition is applied on the node group that represents both the upper and lower surfaces of the SMAHC chevron described in Section 2. Thus, the FSI surface is completely unconstrained and may morph in all three dimensions.

B. Analysis Procedures and Results

The following section discusses results from two numerical analyses conducted using the models described in Section. 2. The first study employs only the FEA model to validate the predicted centerline deflection profiles of the SMAHC chevron against the profiles from benchtop testing conducted in still-air conditions [12]. The second study utilizes both CFD and FEA models in a cosimulation to predict the effect of increasing airflow on the deflection profile of a fully actuated SMAHC chevron.

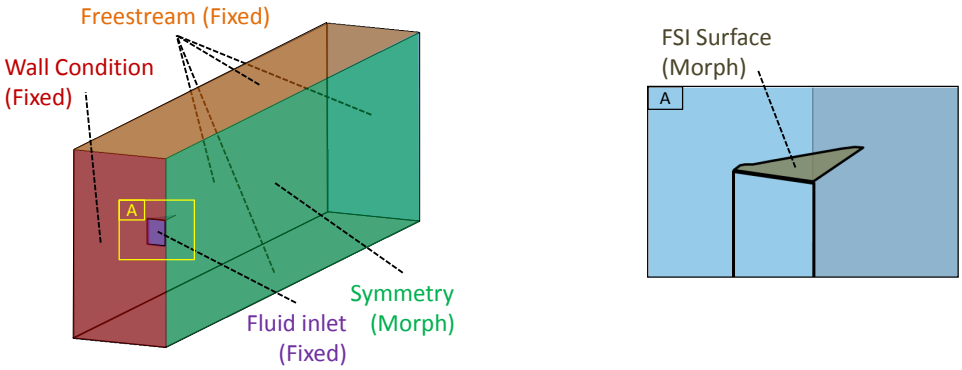

(a) Inlet, wall, and freestream.

(b) Freestream, symmetry, and FSI surface.

Fig. 45. Initial and boundary conditions for the fluid CFD model.

1. Zero-Flow Benchtop Analysis

In this analysis, the IR thermal fields are imported into the model for three temperature set points: 54°C, 88°C, and 121°C. The predicted centerline deflection profiles for the SMAHC chevron actuated under no flow conditions are shown in Fig. 46. These profiles are plotted against corresponding experimental data from the benchtop tests. The computed and experimental profiles match very closely at the lowest temperature setpoint, 54°C. However, significant error between the profiles develops as the temperature setpoint is increased towards 121°C. This is perhaps due to the details of the calibration, or the slight difference between the SMA material properties characterized and those used in this study. Recall that the coefficient of austenite C_A and the constants in the current transformation strain equation $H^{cur}(\overline{\sigma})$ are calibrated to match blocked force test data, and that the FEA-predicted blocked force response of the SMA began to deviate from experiment at higher temperatures around ~ 110°C.

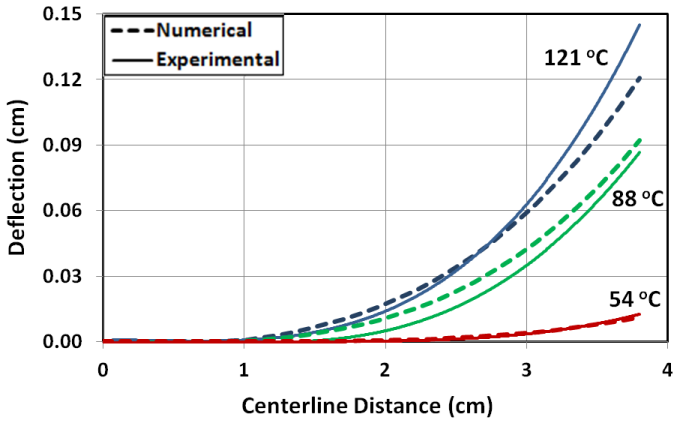

Fig. 46. Comparing FEA-predicted and benchtop test-reported [12] centerline deflection profiles.

2. Representative Flow Conditions

In this next study, the tip deflections for the fully actuated SMAHC chevron are predicted for four flow conditions. These conditions are considered in terms of nozzle pressure ratio (NPR): 0 NPR, 1.46 NPR, 1.62 NPR, and 1.75 NPR. These pressure ratios are converted into equivalent nozzle air velocities (V), dimensionless Reynolds numbers (Re), and dimensionless Mach numbers (M) for flow at sea-level in Table XII.

Table XII. Nozzle air flow characteristics.

Property	0 NPR	1.46 NPR	1.62 NPR	1.75 NPR
V [m/s]	0	250	280	300
Re [-]	0	5.1E5	5.7E5	6.1E5
M [-]	0	0.73	0.82	0.87

Note that the equivalent Mach numbers for each pressure ratio are significantly higher than Mach 0.3, which is widely accepted as the speed at which air can no longer be considered incompressible for typical aerodynamic bodies [77]. This could pose a problem for this study, since the Abaqus/CFD analysis tool cannot account for compressibility effects. However, the body in this study (the SMAHC chevron) is flat and remains relatively parallel to the flow, even during actuation. It might be reasonable to assume that compressibility effects in this study are negligible, even at the given air speeds.

To test this hypothesis, the Star-CCM+ CFD suite by CD-Adapco [82] is used to recreate the fluid domain and boundary conditions described in the previous section as a 2-D domain and, considering the SMAHC to be a rigid flat plate, compare the results of a simple steady-state *incompressible* fluid model with a steady-state *compressible* model that assumes the ideal gas equation of state. A custom output field variable called "Percent Density Variation" is queried to plot the difference (or error) between the density of the incompressible model with that of the compressible model. The resulting percent density variation contour plot is shown in Fig. 47 for the worst case scenario, where the inlet velocity is set to 300 m/s. In these side-views of the fluid domain, the flat plate is circled in red and it can be seen from Fig. 47 that, while there is significant error between the two models downstream of the flat plate, the region local to the flat plate shows almost no variation in density from the incompressibility assumption.

In addition, Fig.48 illustrates the velocity contours for the incompressible and compressible models. It can be seen that there is little apparent variation between the two solutions for the normal-to-inlet velocity. Considering this, along with the observation that density variation is nearly zero in the region close to the flat plate, it can be assumed that the Abaqus/CFD incompressible flow solver will not contribute

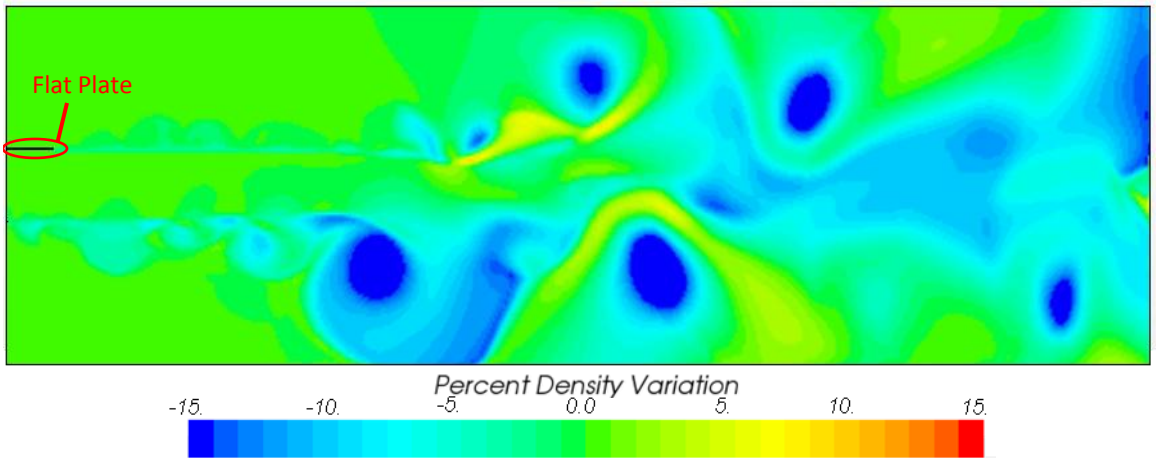

Fig. 47. Side-view contour plot of the percent error between an assumed constant density model and an ideal gas model at 1.75 NPR (300 m/s).

a significant amount of error to the actuated tip deflection predictions made during the FSI analysis.

Using Abaqus/CFD with the FSI cosimulation engine, the full 3-D domain is now considered. The inlet velocity is ramped from zero to one of the three non-zero NPR cases, as was specified in the previous section. While the inlet velocity is ramped, the chevron thermal map for the respective NPR case is simultaneously ramped from zero to the interpolated end-state nodal temperatures. After the chevron is deflected into the flow and the flow is fully stabilized, a condition that is monitored through the real-time output kinetic energy of the fluid domain, the tip deflections associated with each NPR are plotted in Fig. 49(a) against the average of the independently obtained experimental values from the representative flow tests [12].

It is interesting to note that, due to the stiffness of the panel, the effect of the flow on the actuation capabilities of the chevron is quite low. The maximum flow velocity alters the tip deflection by less than one-tenth of a centimeter, which equates

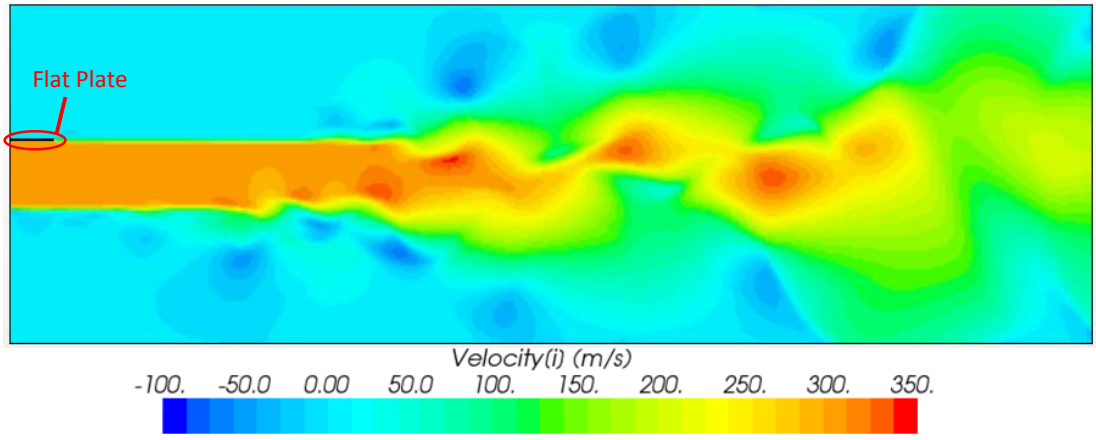

(a) Incompressible model.

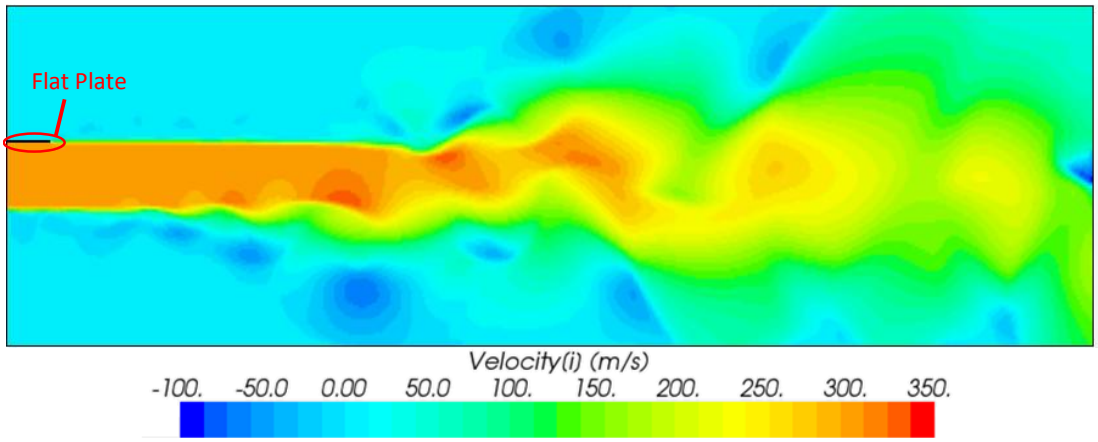

(b) Ideal gas model.

Fig. 48. Side-view contour plot of the normal-to-inlet fluid velocity for the incompressible and compressible models at 1.75 NPR (300 m/s).

to a total change in tip deflection of around $\sim 5\%$. Focusing on the relevant area of the plot, as in Fig. 49(b), we see that the general trend of decreasing tip deflection with increasing flow velocity does reflect the same trend found from experiment [12]. However, it is difficult to determine the accuracy of the model given that, after each experiment conducted by Turner and coworkers, the tip deflection of the chevron prototype never reached zero again after being deactivated in preparation for the next test.

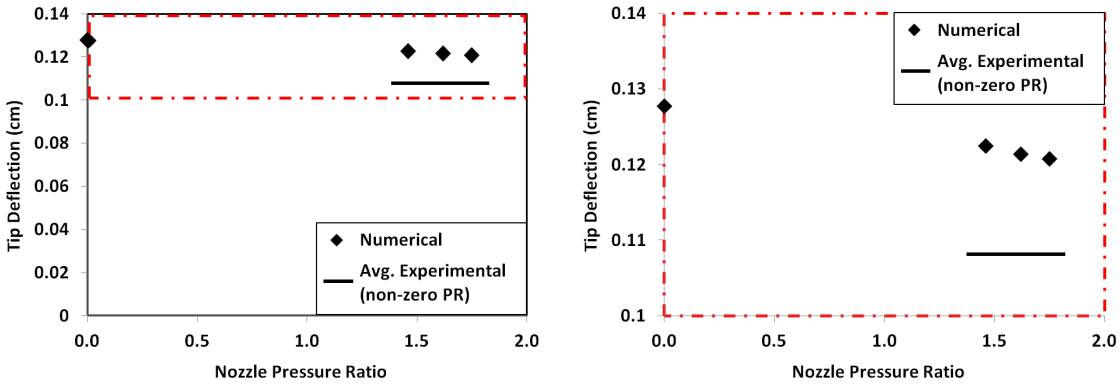

(a) (b)

Fig. 49. Comparing cosimulation-predicted and representative flow test-reported [12] tip deflections.

Contours of the fluid velocity on the symmetric face of the fluid domain are plotted in Fig. 50 for the fully actuated chevron, after the flow has completely stabilized to NPR 1.75. Streamlines are superimposed onto these contours to illustrate the path of travel for fluid particles. It is immediately apparent that the normal-to-inlet fluid velocity contours, outside of the main plume of air and away from the chevron, are significantly lower than those from Fig. 48. Recall that the domain from Fig. 48 is only 2-D, and so fluid is constrained to move in-plane. The lower fluid velocities observed in Fig. 50 are a result of the addition of a third dimension, depth, to the

domain. Thus, fluid momentum is free to expand into the depth of the domain, effectively decreasing the magnitude of V_1.

Also note that the streamlines indicate that the flow at the outlet (on the right the domain) is angled downward with respect to the velocity inlet. This behavior is not seen in Fig. 48, where the 2-D domain is analyzed with the SMAHC approximated as a rigid flat plate. Therefore, it is likely that this downward path of travel seen in Fig. 50 is a result of the actuated chevron altering the path of the flow.

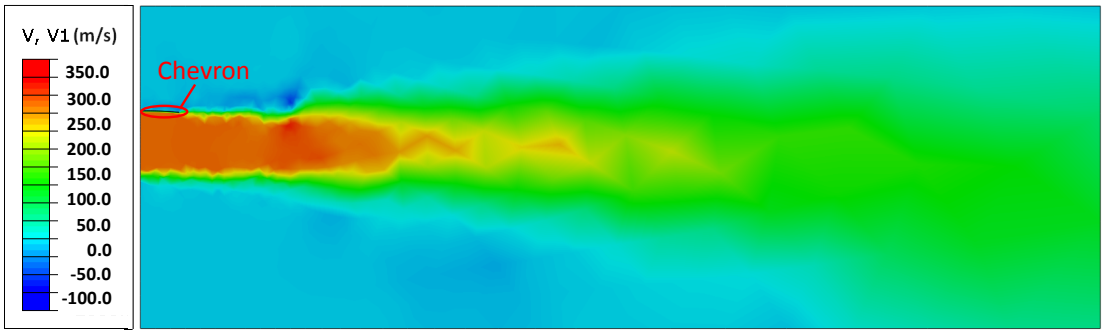

Fig. 50. Side-view of the normal-to-inlet fluid velocity for the 3-D domain at 1.75 NPR (300 m/s).

CHAPTER VI

CONCLUSIONS AND FUTURE WORK

This thesis has proposed a comprehensive framework that can be used to analyze and design shape memory alloy morphing aerostructures. The following chapter summarizes this framework, describes the important observations from the example engineering problems used to demonstrate its capabilities, and suggests certain areas to be further explored.

A. The Design Framework

The first two chapters detailed the background and motivation for proposing an expanded design framework with the capability of considering the mechanical response, transient thermal behavior, and effects of dynamic fluid loading on SMA components, aeroelastic assemblies, and morphing aerostructure systems. It was shown that integration of current commercially available and custom coded tools could be used to cover all of these aspects; namely, a non-linear FEA solver, a thermomechanically coupled (TMC) SMA constitutive model coded into a UMAT that includes a modified heat equation, a CFD solver, a cosimulation engine, simulation process management tools, and optimization algorithms. It was also noted that, although this scheme consists of all of these tools, the engineer or researcher should carefully select which tools be used based on elements of the framework that are active in each model.

Of course, this is not an all-inclusive framework that considers all possible coupling effects. Additional work is suggested to include consideration of actuator *dynamics*. This is especially important as the intelligent design of SMA actuators eventually reduces transformation cycle times down to real-time levels, where inertial effects of the component begin to affect the overall behavior of the morphing aerostructure.

Also, the actuators modeled in this work were assumed to be fully trained to a certain loading level. As a result, the evolution of transformation strain and other transformation properties over subsequent cycles was not captured. For proper integration of these aerostructures as control surfaces, it will be important to consider the effects of continuous actuation at various loading levels on the transformation hysteresis of the SMA component.

Of the three overlapping aspects of the framework illustrated in the Venn diagram from Fig. 4, only two of these were demonstrated in this thesis: fluid-structure interaction (FSI) and TMC. Although the cosimulation algorithm for translating field output data between fluid and solid FSI models works in much the same way for conjugate heat transfer (CHT), a CHT study must still be demonstrated and validated. This can be accomplished using the same tools and procedures utilized in the example FSI engineering problem in Chapter V. However, in this case the thermal energy model would need to be enabled in Abaqus/CFD, and fluid-side heat flux data would be exchanged with solid-side nodal temperatures rather than the structural dynamic field variables exemplified in Chapter II, Section B.2.

The scenario in which a model requires the use of all three interactions (CHT, FSI, TMC) at the same time must also be addressed and demonstrated. Abaqus/Standard does currently does not support the concurrent transfer of thermal and mechanical data with its native CFD module, and so the tools chosen to demonstrate the design framework cannot analyze all three interactions. A third-party CFD software must therefore be used to accomplish this end. One possibility is the Star-CCM+ CFD suite by CD-Adapco, which contains the same cosimulation engine libraries as Abaqus/CFD and can thus communicate with Abaqus/Standard through the same socket-based transfer protocol as the FSI framework shown in Chapter II, Section B.2. Another possibility is the Fluent CFD suite by ANSYS, which can also communicate

with Abaqus/Standard, albeit through the use of another third-party message-passing interface called the Multi-Physics Coupling Code Interface (MPCCI). It should be noted that, at the time when this work was initially being conducted, an unsuccessful attempt was made to use Star-CCM+ for demonstration of full multiphysical coupling of all three interaction types (CHT, FSI, TMC). The then-current version of Star-CCM+ prohibited Abaqus/Standard from making external references to custom UMATs, a bug in the programming that has ostensibly been corrected in recent releases of the suite.

B. Demonstration of the Framework on Example Engineering Problems

The next three chapters demonstrated the expanded framework on real morphing aerostructure designs, namely the Boeing Variable Geometry Chevron (VGC) and the NASA Shape Memory Alloy Hybrid Composite (SMAHC) chevron, with a focus on three analysis levels: component, assembly, and system. Each study necessitated accounting for certain coupling effects between mechanical, fluid, and transient thermal fields, and therefore required different combinations of analysis and simulation process management tools.

1. Component-Level Analysis

In Chapter III, the component-focused comparative analysis was performed on hybrid SMA flexure actuators formed by adding secondary thermally conductive material regions to existing SMA flexure components. The goal was to assess how different secondary materials configured in various geometric distributions might enhance actuation performance. It was shown that the optimized hybrid flexures drastically reduced the component actuation time with respect to all-SMA flexures. In addition,

it was discovered that neglecting latent heat effects of transformation resulted in, on average, 17% error in reported actuation rate.

Unfortunately the difficulty of solving the thermomechanically coupled equations, termed the "full" model, often resulted in failed analysis runs. As a result, no actuation frequency data exists for a flexure consisting entirely of SMA. For a more comprehensive comparative analysis of these flexures, more time should be committed to determining the proper conditions necessary for a thermomechanically coupled analysis to converge consistently, or if perhaps this is an internal issue that is central to the Newton-Rhapson solver. Also, although latent heat effects of transformation were considered for the hybrid flexures, only approximate thermal material properties for the SMA were used that were not validated against experiment. It is therefore suggested that these values be calibrated through careful experimentation for future consideration of thermomechanical coupling in SMA components. Finally, it is suggested that other thermally conductive materials be considered for integration into the hybrid flexure design. It is also clear that the interplay between the thermal diffusivity and yield stress of the conductive material significantly affects the ability of the hybrid flexure to perform work on an elastic structure. More hybrid material combinations should be explored with this in mind.

2. Assembly-Level Analysis

In Chapter IV, the optimization of an assembly-level model considered interaction between SMA actuator components and an elastic composite panel. Positioning of three SMA flexures and stiffening tape thickness were optimized such that the computed composite panel deflection profile error with respect to an ideal deflection profile was minimized. It was shown that the expensive and time-consuming design-build-test methodology used to arrive at the VGC flight-tested configuration could be circum-

vented by utilizing the design framework to produce configurations whose centerline deflections closely matched provided aeroacoustically ideal profiles. A significant difference in optimized design solutions also demonstrated the importance of choosing appropriate quantified measures of device performance.

In this study, optimizing the aeroacoustic effectiveness of the VGC components was considered to be related to how close the actuated aerostructure was to the ideal deflection profile provided by Boeing aeroacoustics engineers. However, it was assumed that emphasis must be placed on the proximity of related points on both profiles, rather than the overall fit of the curves. Recall from Chapter IV that the optimized design solution for cost function C_2 resulted in a centerline deflection profile that was extremely close to the ideal, but was fairly flat from the base towards the mid-length of the panel, then linearly deflected towards the tip. This design, though considered optimized by the chosen cost function, obviously does not capture the intended smooth curvature of the ideal aerostructure. If the nature of the curvature was indeed an important factor, the cost function should be reformulated to consider matching to the spatial derivative of the ideal deflection profile at the tip of the panel. It is therefore suggested, for future aerostructure optimization studies, that careful thought go into the proper definition of the objective to achieve the intended design solution.

3. System-Level Analysis

Finally, in Chapter V, a system-level FSI analysis of a morphing aerostructure was conducted. In this study, the actuation response was predicted of the structure as exposed to high-speed fluid flows of varying velocity. It was shown that the FSI between pressure distribution in the flow field and the deflection profile of the structure could be captured by using cosimulation. The data from the cosimulation reflected a

trend of decreasing tip deflection as fluid velocity increased, however this effect was found to be minimal.

It was also noted that the Abaqus/CFD solver chosen to demonstrate FSI in this work is currently only capable of analyzing incompressible flows. The FSI study violated this assumption by modeling flow at a velocity well above the incompressibility limit for aerospace lifting bodies. It was shown that, for the particular morphing structure and fluid domain studied, the effect of neglecting compressibility effects was quite low. However, future analysis of morphing aerostructures that are blunt or that cause inhomogeneous flow fields in high-speed flows would need to account for changes in fluid density. This should motivate efforts to increase the accuracy of FSI modeling by considering less simplifying assumptions. It is suggested that third-party CFD programs capable of analyzing fluid compressibility, such as Star-CCM+ and Fluent, be employed to communicate with Abaqus/Standard in order to analyze FSI problems where the fluid density is expected to change significantly.

REFERENCES

[1] B. Sanders, R. Crowe, and E. Garcia, "Defense advanced research projects agency – Smart materials and structures demonstration program overview," *Journal of Intelligent Material Systems and Structures*, vol. 15, pp. 227–233, 2004.

[2] J. Kudva, "Overview of the darpa smart wing project," *Journal of Intelligent Material Systems and Structures*, vol. 15, pp. 261–267, 2004.

[3] J. K. Strelec, D. C. Lagoudas, M. A. Khan, and J. Yen, "Design and implementation of a shape memory alloy actuated reconfigurable wing," *Journal of Intelligent Material Systems and Structures*, vol. 14, pp. 257–273, 2003.

[4] M. Tawfik, J. Ro, and C. Mei, "Thermal post-buckling and aeroelastic behaviour of shape memory alloy reinforced plates," *Smart Materials and Structures*, vol. 11, pp. 297–307, 2002.

[5] C. Nam, A. Chattopadhyay, and Y. Kim, "Application of shape memory alloy (SMA) spars for aircraft maneuver enhancement," in *Proceedings of SPIE, Smart Structures and Materials*, San Diego, CA, 17–21 March 2002, vol. 4701, pp. 226–236.

[6] H. Prahlad and I. Chopra, "Design of a variable twist tiltrotor blade using shape memmory alloy (SMA) actuators," in *Proceedings of SPIE, Smart Structures and Materials*, Newport Beach, CA, 4–8 March 2001, vol. 4327, pp. 46–59.

[7] A. Jacot, R. Ruggeri, and D. Clingman, "Shape memory alloy device and control method," U.S. Patent 7,037,076, 2 May 2006.

[8] K. Singh and I. Chopra, "Design of an imporoved shape memory alloy actuator for rotor blade tracking," in *Proceedings of SPIE, Smart Structures and Materials*, San Diego, CA, 17–21 March 2002, vol. 4701, pp. 244–266.

[9] D. Kennedy, F. Straub, L. Schetky, Z. Chaudhry, and R. Roznoy, "Development of an SMA actuator for in-flight rotor blade tracking," *Journal of Intelligent Material Systems and Structures*, vol. 15, pp. 235–248, April 2004.

[10] D.M. Pitt, J. Dunne, E. White, and E. Garcia, "SAMPSON smart inlet SMA powered adaptive lip design and static test," *Proceedings of the 42nd AIAA Structures, Structrual Dynamics, and Materials Conference, Seattle, WA, 16–20 April 2001*, pp. 1–11, 2001.

[11] F.T. Calkins, J.H. Mabe, and R.T. Ruggeri, "Overview of Boeing's shape memory alloy based morphing aerostructures," *Proceedings of SMASIS08: ASME Conference on Smart Materials, Adaptive Structures and Intelligent Systems, October 28–30, 2008, Ellicott City, MD*, pp. 1–11, 2008.

[12] T. Turner, R. Cabell, R. Cano, and R. Silcox, "Development of a preliminary model-scale adaptive jet engine chevron," *American Institute of Aeronautics and Astronautics*, vol. 46, no. 10, pp. 2545–2557, 2008.

[13] R. Mani, D. Lagoudas, and O. Rediniotis, "MEMS based active skin for turbulent drag reduction," in *Proceedings of SPIE, Smart Structures and Materials*, San Diego, CA, 2–6 March 2003, vol. 5056, pp. 9–20.

[14] T. Quackenbush, R. McKillip, and G. Whitehouse, "Development and testing of deployable vortex generators using sma actuation," in *Proceedings of the 28th AIAA Applied Aeroacoustics Conference*, Chicago, IL, June 2010, pp. 1–16.

[15] P.K. Kumar and D.C. Lagoudas, "Thermomechanical constitutive modeling of SMAs," in *Shape Memory Alloys: Modeling and Engineering Applications*, D.C. Lagoudas, Ed., chapter 1, pp. 29–35. Springer-Verlag, New York, 2008.

[16] J. Schick, D.J. Hartl, and D.C. Lagoudas, "Incorporation of shape memory alloy actuators into morphing aerostructures," in *Morphing Aerospace Vehicles and Structures*, J. Valasek, Ed. Wiley, 2012.

[17] Gangbing Song and Ning Ma, "Robust control of a shape memory alloy wire actuated flap," *Smart Materials and Structures*, vol. 16, no. 6, 2007.

[18] J. Kudva, K. Appa, C. Martin, and A. Jardine, "Design, fabrication, and testing of the DARPA/Wright lab 'smart wing' wind tunnel model," in *Proceedings of the 38th AIAA/ASME/ASCE/AHS/ASC Structures, Structural Dynamics, and Materials Conference and Exhibit*, Kissimmee, FL, April 7–10 1997, pp. 1–6.

[19] J. H. Mabe, F.T. Calkins, and G.W Butler, "Boeing's variable geometry chevron, morphing aerostructure for jet noise reduction," in *47th AIAA/ ASME / ASCE / AHS / ASC Structures, Structural Dynamics and Materials Conference*, Newport, Rhode Island, 1–4 May 2006, pp. 1–19.

[20] J. Bridges, M. Wernet, and C. Brown, "Control of jet noise through mixing enhancement," Tech. Rep. NASA TM-2003-212335, NASA, 2003.

[21] D. Hartl, D. Lagoudas, J. Mabe, and F. Calkins, "Use of Ni60Ti shape memory alloy for active jet engine chevron application, Part I: Thermomechanical characterization," *Smart Materials and Structures*, vol. 19, no. 1, 2009.

[22] D. Hartl, D. Lagoudas, J. Mabe, F. Calkins, and J. Mooney, "Use of Ni60Ti shape memory alloy for active jet engine chevron application, Part II: Experi-

mentally validated numerical analysis," *Smart Materials and Structures*, vol. 19, no. 1, 2009.

[23] K.K. Choi and N.-H. Kim, *Structural Sensitivity Analysis and Optimization 1: Linear Systems*, Mechanical Engineering Series. Springer-Verlag, Berlin, 2005.

[24] L. C. Brinson, "One-dimensional constitutive behavior of shape memory alloys: Thermomechanical derivation with non-constant material functions and redefined martensite internal variable," *Journal of Intelligent Material Systems and Structures*, vol. 4, pp. 229–242, 1993.

[25] D. C. Lagoudas, Z. Bo, and M. A. Qidwai, "A unified thermodynamic constitutive model for SMA and finite element analysis of active metal matrix composites," *Mechanics of Composite Materials and Structures*, vol. 3, pp. 153–179, 1996.

[26] F. Daghia, D. Inman, F. Ubertini, and E. Viola, "Shape memory alloy hybrid composite plates for shape and stiffness control," *Journal of Intelligent Material Systems and Structures*, vol. 19, pp. 609–619, 2008.

[27] J. Roh, J. Han, and I. Lee, "Finite element analysis of adaptive inflatable structures with SMA strip actuator," in *Proceedings of SPIE, Smart Structures and Materials*, San Diego, CA, 7–10 March 2005, vol. 5764, pp. 460–471.

[28] A. Vitiello, A. Squillace, and U. Prisco, "Characterization of NiTinol under torsional loads through a numerical implementation of the Boyd-Lagoudas constitutive model and comparison of the results with experimental data," *Smart Materials and Structures*, vol. 16, pp. 76–82, 2007.

[29] H. Jun, O. Rediniotis, and D. Lagoudas, "Development of a fuel–powered shape

memory alloy actuator system: II. Numerical analysis," *Smart Materials and Structures*, vol. 16, pp. S81–S94, 2007.

[30] L.G. Machado and D.C. Lagoudas, "Thermomechanical constitutive modeling of SMAs," in *Shape Memory Alloys: Modeling and Engineering Applications*, D.C. Lagoudas, Ed., chapter 3, pp. 175–179. Springer-Verlag, New York, 2008.

[31] Abaqus, *Analysis User's Manual*, Dassault Systèmes of America Corp., Woodlands Hills, CA, 2010.

[32] F. Auricchio and R. L. Taylor, "Shape-memory alloys: Modelling and numerical simulation of the finite-strain superelastic behavior.," *Computer Methods in Applied Mechanics and Engineering*, vol. 143, no. 1–2, pp. 175–194, 1997.

[33] F. Auricchio, R. L. Taylor, and J. Lubliner, "Shape-memory alloys: Macromodelling and numerical simulations of the superelastic behavior," *Computer Methods in Applied Mechanics and Engineering*, vol. 146, pp. 281–312, 1997.

[34] MSC Software Corporation, *MSC MARC User's Manual*, 2006.

[35] "Technical report," Tech. Rep., Department of Applied Mechanics and Engineering Sciences, University of California at San Diego, 1995.

[36] M. A. Qidwai and D. C. Lagoudas, "Numerical implementation of a shape memory alloy thermomechanical constitutive model using return mapping algorithms," *International Journal for Numerical Methods in Engineering*, vol. 47, pp. 1123–1168, 2000.

[37] C. M. Jackson, H. J. Wagner, and R. J. Wasilewski, "55-Nitinol—The alloy with a memory: Its physical metallurgy, properties and applications," Tech.

Rep. NASA SP-5110, NASA Technology Utilization Office, Washington, D.C., 1972.

[38] Frank Richter, Oliver Kastner, and Gunther Eggeler, "Implementation of the mller-achenbach-seelecke model for shape memory alloys in ABAQUS," *Journal of Materials Engineering and Performance*, vol. 18, pp. 626–630, 2009, 10.1007/s11665-009-9483-x.

[39] J. G. Boyd and D. C. Lagoudas, "A thermodynamical constitutive model for shape memory materials. Part II. The SMA composite material," *International Journal of Plasticity*, vol. 12, no. 7, pp. 843–873, 1996.

[40] D. Christ and S. Reese, "A finite element model for shape memory alloys considering thermomechanical couplings at large strains," *International Journal of Solids and Structures*, vol. 46, no. 20, pp. 3694–3709, 2009.

[41] S. Seelecke and I. Müller, "Shape memory alloy actuators in smart structures: Modeling and simulation," *Applied Mechanics Reviews*, vol. 57, no. 1, pp. 23–46, 2004.

[42] L.G. Machado and D.C. Lagoudas, "Thermomechanical constitutive modeling of SMAs," in *Shape Memory Alloys: Modeling and Engineering Applications*, D.C. Lagoudas, Ed., chapter 3, pp. 122–187. Springer-Verlag, New York, 2008.

[43] T. Turner, R. Buehrle, R. Cano, and G. Fleming, "Modeling, fabrication, and testing of a SMA hybrid composite jet engine chevron concept," *Journal of Intelligent Material Systems and Structures*, vol. 17, pp. 483–497, June 2006.

[44] P. A. Popov, "Constitutive modelling of shape memory alloys and upscaling of

deformable porous media," Ph.D. dissertation, Texas A&M University, Department of Aerospace Engineering, May 2005.

[45] M. I. Frecker, "Recent advances in optimization of smart structures and actuators," *Journal of Intelligent Material Systems and Structures*, vol. 14, pp. 207–216, 2003.

[46] D.C. Lagoudas, Ed., *Shape Memory Alloys: Modeling and Engineering Applications*, Springer-Verlag, New York, 2008.

[47] D. Hartl and D. Lagoudas, "Advanced methods for the analysis, design, and optimization of sma-based aerostructures yield in shape memory alloys," *Smart Materials and Structures*, vol. 20, pp. 1–21, 2011.

[48] G. Dumont and C. Kühl, "Finite element simulation for design optimisation of shape memory alloy spring actuators," *Engineering Computations*, vol. 22, no. 7, pp. 835 – 848, 2005.

[49] C.C. Lan, J.H. Wang, and C.H. Fan, "Optimal design of rotary manipulators using shape memory alloy wire actuated flexures," *Sensors and Actuators A: Physical*, vol. 153, no. 2, pp. 258 – 266, 2009.

[50] S. Wang and J. C. Brigham, "A computational inverse problem approach for the design of morphing processes in thermally activated smart structural materials," *Proceedings of SPIE, Active and Passive Smart Structures and Integrated Systems, San Diego, CA, 27 April 2011*, vol. Vol. 7977, 2011.

[51] Justin Manzo and Ephrahim Garcia, "Analysis and optimization of the active rigidity joint," *Smart Materials and Structures*, vol. 18, no. 12, pp. 125020, 2009.

[52] O E Ozbulut, P N Roschke, P Y Lin, and C H Loh, "Ga-based optimum design of a shape memory alloy device for seismic response mitigation," *Smart Materials and Structures*, vol. 19, no. 6, pp. 065004, 2010.

[53] M. Langelaar and F. van Keulen, "Design optimization of shape memory alloy active structures using the R-phase transformation," in *Proceedings of SPIE, Smart Structures and Materials*, 18–22 March 2007, vol. 6525.

[54] M. Langelaar and F. van Keulen, "Sensitivity analysis of shape memory alloy shells," *Computers & Structures*, vol. 86, no. 9, pp. 964 – 976, 2008.

[55] M. Langelaar and F. van Keulen, "Modeling of shape memory alloy shells for design optimization," *Computers & Structures*, vol. 86, no. 9, pp. 955 – 963, 2008.

[56] K.K. Choi and N.-H. Kim, *Structural Sensitivity Analysis and Optimization 2: Nonlinear Systems and Applications*, Mechanical Engineering Series. Springer-Verlag, Berlin, 2005.

[57] S.P. Gurav, M. Langelaar, and F. Van Keulen, "Uncertainty-based design optimization of shape memory alloy microgripper using combined cycle-based alternating anti-optimization and nested parallel computing," in *6th World Congresses of Structural and Multidisciplinary Optimization*, 2008.

[58] Y. Ben-Haim and I. Elishakoff, "Convex models of uncertainty in applied mechanics," *Elsevier*, 1990.

[59] Y. Ben-Haim, "Robust reliability in the mechanical sciences," *Springer*, 1996.

[60] R. D. Widdle, Jr., M. T. Grimshaw, and M. Shome, "Optimal design of a shape memory alloy actuated composite structure with iterative finite element

analysis," in *Proceedings of SPIE, Smart Structures and Materials*, 9 March 2009, vol. 7288.

[61] L. Gravatt, J. Mabe, F. Calkins, and D. Hartl, "Characterization of varied geometry shape memory alloy beams," in *Proceedings of SPIE, Smart Structures and Materials*, San Diego, CA, 8–11 March 2010, vol. 7645, pp. 1–12.

[62] J. N. Reddy, *Introduction to the Finite Element Method*, McGraw-Hill, Boston, 3rd edition, 2006.

[63] M.A.S. Qidwai, D.J. Hartl, and D.C. Lagoudas, "Thermomechanical constitutive modeling of SMAs," in *Shape Memory Alloys: Modeling and Engineering Applications*, D.C. Lagoudas, Ed., chapter 4, pp. 191–192. Springer-Verlag, New York, 2008.

[64] Darren J. Hartl, George Chatzigeorgiou, and Dimitris C. Lagoudas, "Three-dimensional modeling and numerical analysis of rate-dependent irrecoverable deformation in shape memory alloys," *International Journal of Plasticity*, vol. 26, no. 10, pp. 1485–1507, 2010.

[65] Y. Chemisky, A. Duval, E. Patoor, and T. Ben Zineb, "Constitutive model for shape memory alloys including phase transformation, martensitic reorientation and twins accommodation," *Mechanics of Materials*, vol. 43, no. 7, pp. 361–376, 2011.

[66] Dimitris C. Lagoudas, Darren Hartl, Yves Chemisky, Luciano Machado, and Peter Popov, "Constitutive model for the numerical analysis of phase transformation in polycrystalline shape memory alloys," *International Journal of Plasticity*, pp. 1–29, available online, in press.

[67] J. Tu, G. Heng Yeoh, and C. Liu, *Computational Fluid Dynamics: A Practical Approach*, Elsevier, Amsterdam, 1st edition, 2008.

[68] D. Hartl, J. Mooney, D. Lagoudas, F. Calkins, and J. Mabe, "Experimentally validated numerical analysis of aerostructures incorporating shape memory alloys," *Proceedings of SPIE, Smart Structures and Materials: Active Materials: Behavior and Mechanics, San Diego, CA, 9–13 March 2008*, vol. 6929, pp. 1–12, 2008.

[69] ModelCenter, *Model Center 9.0 User's Manual*, Phoenix Integration, Philadelphia, PA, 2009.

[70] Abaqus, *ISight User's Manual*, Dassault Systèmes of America Corp., Woodlands Hills, CA, 2007.

[71] D. L. Logan, *Mechanics of Materials*, HarperCollins Publishers, New York, 1991.

[72] Inc. Copper Development Association, Ed., *CDA Copper in Architecture Design Handbook*, Copper Development Association, Inc., New York, 2010.

[73] D. R. Smith and F. R. Fickett, "Low-temperature properties of silver," *Journal of Research of the National Institute of Standards and Technology*, vol. 100, no. 2, 1995.

[74] K. Otsuka and C. M. Wayman, Eds., *Shape Memory Materials*, Cambridge University Press, Cambridge, 1999.

[75] T.J. Zimmerman, K.Y. Blohowiak, M.A. Dilligan, F.T. Calkins, and Mabe J.H., "Adhesive bonding of hybrid actuated shape memory alloy-composite structures," in *47nd ISTC, Society for the Advancement of Material and Process Engineering*, Salt Lake City, Utah, 11–14 October 2010, pp. 1–14.

[76] F. P. Incropera and D. P. DeWitt, *Fundamentals of Heat and Mass Transfer*, John Wiley & Sons, New York, 3rd edition, 1990.

[77] J. D. Anderson Jr., *Introduction to Flight*, McGraw-Hill, New York, 5th edition, 2005.

[78] Maplesoft, *The Maple Help System*, Waterloo Maple Inc., Waterloo, ON, 2010.

[79] D. Hartl, T. Zimmerman, M. Dilligan, J. Mabe, and F. Calkins, "Analysis of shape memory alloy components using beam, shell, and continuum finite elements," *Proceedings of SMASIS10: ASME Conference on Smart Materials, Adaptive Structures and Intelligent Systems, September 28–October 1, 2010, Philadelphia, PA*, pp. 1–11, 2010.

[80] F. T. Calkins, J. H. Mabe, and G. W. Butler, "Boeing's variable geometry chevron: Morphing aerospace structures for jet noise reduction," in *Proceedings of SPIE, Smart Structures and Materials 2006: Industrial and Commerical Applications of Smart Structures Technologies*, San Diego, CA, 27 February 2006.

[81] T. Turner, C. Lach, and R. Cano, "Fabrication and characterization of SMA hybrid composites," in *Proceedings of SPIE, Smart Structures and Materials*, 4–8 March 2001, vol. 4333.

[82] Star-CCM+, *Star-CCM+ User Guide*, CD-Adapco, 2011.

VITA

Stephen Daniel Oehler graduated from Texas A&M with a Bachelor of Science degree in Aerospace Engineering in May of 2010. His interest in material science and structures began after working as a lab intern at NASA JSC for several months in 2008, fabricating and preparing dog bone specimens for fatigue testing. Under the mentorship of Dr. Darren J. Hartl and Dr. Dimitris C. Lagoudas starting in 2009, he then gained an appreciation for active materials and the modeling of such materials behavior with finite element analysis. Two years after enrolling in the graduate program at Texas A&M in 2010, Stephen graduated with a Master of Science in Aerospace Engineering in August of 2012. He is now a structural analysis engineer at The Boeing Company.